



3D Electron Microscopy of Nanostructures in Energy Devices

Colding-Jørgensen, Sofie

Publication date:
2020

Document Version
Publisher's PDF, also known as Version of record

[Link back to DTU Orbit](#)

Citation (APA):
Colding-Jørgensen, S. (2020). *3D Electron Microscopy of Nanostructures in Energy Devices*. Technical University of Denmark.

General rights

Copyright and moral rights for the publications made accessible in the public portal are retained by the authors and/or other copyright owners and it is a condition of accessing publications that users recognise and abide by the legal requirements associated with these rights.

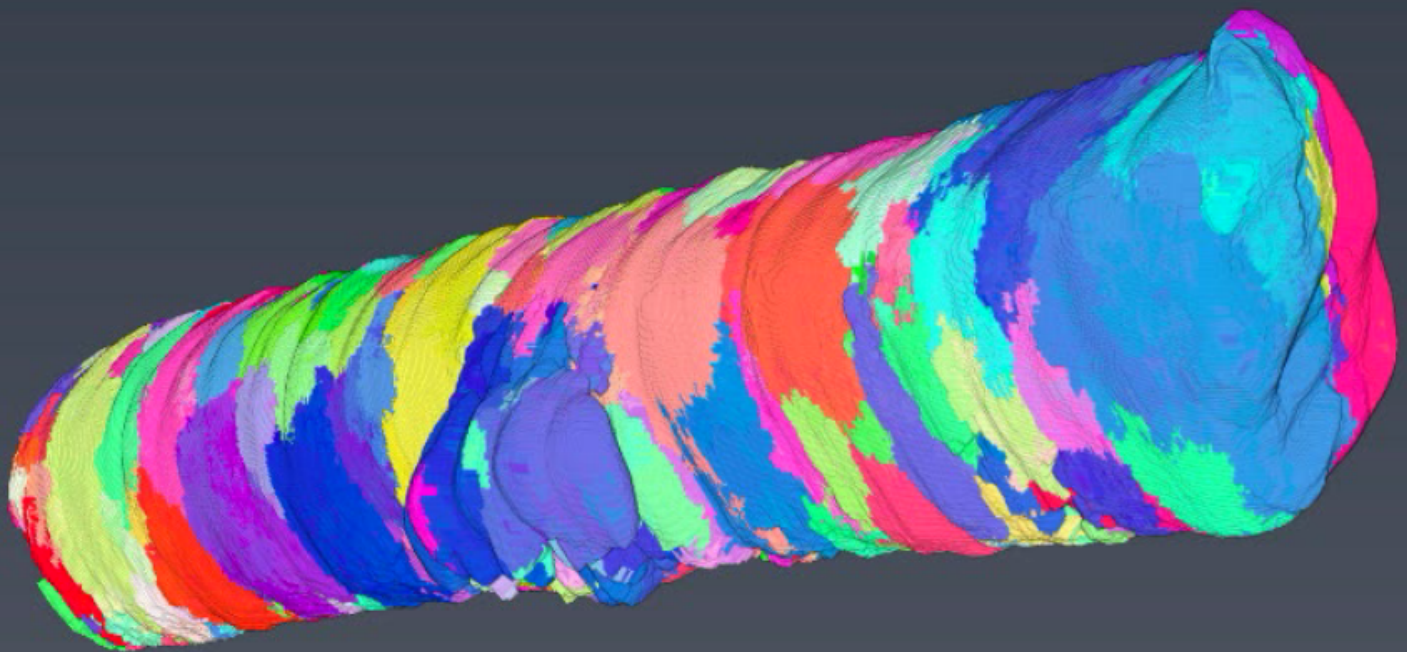
- Users may download and print one copy of any publication from the public portal for the purpose of private study or research.
- You may not further distribute the material or use it for any profit-making activity or commercial gain
- You may freely distribute the URL identifying the publication in the public portal

If you believe that this document breaches copyright please contact us providing details, and we will remove access to the work immediately and investigate your claim.

3D Electron Microscopy of Nanostructures in Energy Devices

by Sofie Colding-Jørgensen

Ph.D. Dissertation



200 nm

3D Electron Microscopy of Nanostructures in Energy Devices

by Sofie Colding-Jørgensen

Ph.D. Dissertation

August, 2020

By

Sofie Colding-Jørgensen

Copyright: Reproduction of this publication in whole or in part must include the customary bibliographic citation, including author attribution, report title, etc.

Published by: DTU, Department of Energy Conversion and Storage, Fysikvej, Building 310, 2800 Kgs. Lyngby Denmark
www.energy.dtu.dk

Abstract

The increasing demand for renewable energy has led to an interest in the field of energy conversion devices to exploit fluctuating energy production from solar cells and wind turbines. One of the solutions is the Solid Oxide Cell (SOC). Some of the new promising materials for SOCs are electrospun nanofibres of e.g. gadolinium doped ceria. However, characterizing these types of structures is challenging as they are polycrystalline complex nanostructured materials composed of hundreds-thousands of nano-grains with down to 1 nm wide grain boundaries.

3D Orientation Mapping in the Transmission Electron Microscope (3D-OMiTEM) is a promising technique that can non-destructively determine crystal orientations and morphology in 3D with a resolution of down to 1 nm. In this exploratory work the emphasis has been on applying 3D-OMiTEM on different materials to find potentials and challenges when applying the method. The three materials, maghemite nanoflowers, silver nanowire and electrospun gadolinium doped ceria nanofibres each showed different potentials of the 3D-OMiTEM technique.

The main identified potentials are; the ability to do statistical morphological analysis on an ensemble of particles and crystallites, accurately determination of orientation and structures such as twin-structures and ultimately determination of transport properties through solids. To elaborate on the latter: This work shows how it is possible to determine a relationship between crystal orientation and doping concentration in the grain boundary of polycrystalline solids using a combination of 3D-OMiTEM and Energy Filtered Transmission Electron Microscopy (EFTEM). With this knowledge it is possible to calculate the ion conductivity path through the solid with the least resistance. This provides a new insights to these kind of materials.

Following this, preliminary results are presented showing possible methods for measuring conductivity of nanofibres. This could give a comparison value for the calculated path with least resistance from 3D-OMiTEM/EFTEM. Ultimately, conductivity measurements

together with 3D-OMiTEM/EFTEM results can prove to be a strong tool in understanding and describing conductivities in ion conductive solids.

Resumé

Den stigende efterspørgsel efter bæredygtig energi har ført til en interesse i energikonvertering til bedre udnyttelse af den svingede energiproduktion fra solceller og vindmøller. En af energikonverteringsløsningerne er faststofoxidceller. Nogle af de nye lovende materialer til faststofoxidceller er elektrospundne nanofibre af f.eks. gadolinium doteret ceriumoxid. Det er imidlertid udfordrende at karakterisere sådanne materialer, da det er polykrystallinske komplekse nanostrukturerede materialer, som er sammensat af hundrede-tusinder af nanokorn med ned til 1 nm brede korngrensener.

3D-orienteringskortlægning i transmissionselektronmikroskopet (3D-OMiTEM) er en ikke-destruktiv teknik, der kan bestemme krystalorienteringer og morfologi i 3D med en opløsning på ned til 1 nm. I dette arbejde har der været fokus på at anvende 3D-OMiTEM på forskellige materialer for at finde metodens potentialer og udfordringer. De tre materialer, maghemit nano-blomster, sølv nanotråd og elektrospundet gadolinium doteret ceriumoxid nanofibre, viste hver især forskellige potentialer og udfordringer ved anvendelsen af 3D-OMiTEM teknikken.

De væsentlige potentialer er; evnen til at udføre statistisk morfologisk analyse på et ensemble af partikler og/eller krystallitter, nøjagtig bestemmelse af orientering og strukturer såsom twinstrukturer og i sidste ende bestemmelse af transportegenskaber gennem faststoffer. En uddybelse af det sidstnævnte er som følger: Dette arbejde præsenterer, hvordan det er muligt at bestemme et forhold mellem krystalorientering og dopingkoncentration i korngrensen for polykrystallinske faststoffer ved hjælp af en kombination af 3D-OMiTEM og energifiltreret transmissionselektronmikroskopi (EFTEM). Med denne viden, er det muligt at beregne ionledningsvejen gennem materialet med mindst mulig modstand. Dette giver en helt ny indsigt i denne type materialer.

Efter dette præsenteres foreløbige resultater, der viser mulige metoder til måling af ledningsevne af sådanne nanofibre. Dette kan give et sammenligningsgrundlag for den beregnede sti med mindst modstand fra 3D-OMiTEM/EFTEM. Ultimativt, kan

ledningsevne målinger sammen med 3D-OMiTEM/EFTEM-resultaterne være et stærkt værktøj til forståelse og beskrivelse af ledningsevne i ionledende faststoffer.

Preface

This thesis is submitted in candidacy for the Ph.D. degree from the Technical University of Denmark (DTU). The work was carried out at the Department of Energy Conversion and Storage in the period from August 2017 to August 2020. The project was supervised by head of section Luise Theil Kuhn and co-supervised by senior researcher Søren Bredmose Simonsen and senior scientist Søren Schmidt. The plan was to conduct a three months external stay at Arizona State University in Peter A. Crozier's group at the School for Engineering of Matter, Transport and Energy. Due to the COVID-19 the stay way shortened. This research stay was partly funded by a travel grant from the Idella foundation.

August 2020

A handwritten signature in black ink that reads "Sofie Colding-Jørgensen". The signature is written in a cursive, flowing style.

Sofie Colding-Jørgensen

Acknowledgements

Luise Theil Kuhn, Head of section, DTU Energy

Firstly, I would like to thank my main supervisor, Luise, for the scientific support and guidance during the three years and for letting me know that my work was appreciated.

Søren Bredmose Simonsen, Senior Researcher, DTU Energy

Søren was my co-supervisor and I would like to thank him for the daily supervision at the microscope and for the general guidance and support.

Søren Schmidt, Senior Scientist, DTU Physics

My co-supervisor, I would like to thank for his guidance in the reconstruction process and for helping me get in contact with researchers at Chongqing University.

Peter Crozier, Professor, Arizona State University

I would like to sincerely gratitude Peter, as well as his entire group at Arizona State University, for hosting my external stay even though it was shortened. Furthermore, I would like to thank for the scientific discussions after my return to DTU.

Xiaoxu Huang, Senior Researcher, DTU Mechanics

I would like to thank him for the scientific discussions and guidance in regards to 3D-OMiTEM as well as for hosting me and introducing me to his group while being at Chongqing University.

Qiongyao He, PhD, Chongqing University

I would like to thank for the introduction to 3D-OMiTEM acquisition and for the collaboration both at Chongqing University and at Technical University of Denmark.

Peter Stanley Jørgensen, Senior Researcher, DTU Energy

I would like to thank for his support in 3D image analysis and calculation of 3D percolation paths.

Karl Tor Sune Thydén, Development Engineer, DTU Energy

Karl helped me during sample preparation and conductivity measurements at the Scanning

Electron Microscopes. For this I would like to thank him and his patience in the long hours of microscopy time.

Ebtisam Abdellahi, Laboratory technician, DTU Energy

I would like to thank for our discussions on sample preparation and for assisting me in the lab.

Rune E. Johnsen, Former DTU Energy

Thanks for the help in the x-ray diffraction measurements.

Wenjing (Angela) Zhang, Associate Professor, DTU Environment

I would like to thank for providing me with electrospun nano fibres for the projects and for sharing her knowledge on electrospun fibres.

Cathrine Frandsen, Professor, DTU Physics

Thanks, for the guidance and collaboration on magnetic nanoparticles and for the discussions of the results

Miriam Varón, Research Engineer, DTU Physics

Thanks, for providing me with magnetic nanoparticle samples for the project and prior TEM analysis.

Kristian Mølhave, Associate Professor, DTU Nanolab

I would like to thank for the collaboration of silver nanowires and for our scientific discussions.

Murat Nulati Yesibolati, Postdoc, DTU Nanolab

Thank, for providing me with silver nanowire samples and for assisting me at the 3D-OMiTEM acquisition during late hours.

Joachim Dahl Thomsen, Postdoc, DTU Physics

I would like to thank for his support and guidance in chips designs for conductivity measurements.

Patrick Rebsdorf Whelan, Postdoc, DTU Physics

Thanks, for the training and guidance in measuring conductivities of nanofibres.

Jacob R. Bowen, Assistant Professor, DTU Energy

I would like to thank for our time sharing office at Risø and for the scientific discussions on 3D segmentation.

List of Publications

Publications Included in This Thesis

Colding-Jørgensen, S.; Simonsen, S. B.; Jørgensen, P. S.; Zhan, W.; Huang, X.; Schmidt, S.; Theil Kuhn, L. (submitted): 3D Ion Percolation Path in Gadolinium Doped Ceria Nanofibres for Solid Oxide Electrochemical Cells

Manuscript is placed in appendix C.

Publications not Included in This Thesis

Kabir, A., Colding-Jørgensen, S., Molin, S., & Esposito, V. (Accepted/In press): Electrical conductivity of nanostructured acceptor-doped ceria fabricated by Spark Plasma Sintering (SPS). *Materials Letters*, [128513].

Kabir, A., Zhang, H., Colding-Jørgensen, S., Santucci, S., Molin, S., & Esposito, V. (2020). Electro-chemo-mechanical properties in nanostructured Ca-doped ceria (CDC) by field assisted sintering. *Scripta Materialia*, 187, 183-187.

Contents

Abstract	iii
Resumé	v
Preface	vii
Acknowledgements	ix
List of Publications	xi
1 Introduction	1
1.1 Aim	3
1.2 Objectives	3
1.3 Outline of Thesis	4
2 Mathematical Formalism and Definitions	7
2.1 Crystallographic Orientation	7
2.2 Characterization of Grain Boundaries	8
3 Experimental methods	13
3.1 3D-OMiTEM	13
3.2 Energy Filtered Transmission Electron Microscopy (EFTEM)	26
4 OMiTEM Parameter Testing	29
5 Crystallographic Texture of Silver Nanowire for Galvanic Replacement	37
5.1 Introduction	37
5.2 Experimental Methods	39
5.3 Results and Discussion	40
5.4 Conclusion	49
6 Statistical Morphological Analysis of Maghemite Nanoflower Ensemble using 3D-OMiTEM	51

6.1	Introduction	51
6.2	Experimental	53
6.3	Results and Discussion	54
6.4	Conclusion	60
7	Determination of 3D Ion Percolation Path in CGO Nanofibers for Solid Oxide Fuel Cells	63
7.1	Abstract	63
7.2	Introduction	64
7.3	Experimental Methods	67
7.4	3D-OMiTEM	68
7.5	Results and Analysis	69
7.6	Conclusion	81
8	Preliminary Method Development for Measuring Conductivity of Single Nanofibre	83
8.1	Experimental	84
8.2	Set-up	84
8.3	Chip Design	85
8.4	Electrode deposition	89
8.5	Measuring IV curves	91
8.6	Conclusion	92
9	Conclusion	95
9.1	Future Work	97
A	OMiTEM Reconstruction Manual	107
B	OMiTEM Acquisition Manual	139
C	Manuscript 1	145

Chapter 1

Introduction

There is a widely agreement amongst contemporary researchers that greenhouse gases stemming from combustion of fossil fuels have a great impact on the climate i.e. rising global temperatures and extreme weather conditions. The EU commission recommend switching to sustainable energy sources for energy production to reach the goal of reducing greenhouse gas emission¹.

The goal set by the Danish government is to have a climate neutral society by 2050². Currently, the European energy production amount to 70% of the greenhousegas emission³. In 2018 18.9% of the energy production was produced from renewable energy⁴. In 2019 in Denmark, with the new offshore wind farms, 47% of the total electricity consumption was produced by wind energy while 3% was produced from solar energy⁵. However, both wind- and solar energy produce fluctuating energy and as a result there is an increasing interest in energy conversion and storage devices.

A promising candidate for an energy conversion device is the Solid Oxide Electrochemical Cell (SOC). The SOC can be operated in either fuel cell mode (SOFC) to produce power from a hydrogen- or carbon based fuel or in electrolyser mode (SOEC) to store energy as a chemical fuel. By using SOECs it would thereby be possible to convert excess energy produced by wind- or solar energy to a fuel which could hereafter be used to generate power with SOFCs⁶⁻⁸.

SOCs are composed of layers of different materials. A cathode, an electrolyte and an anode. In fuel cell mode with hydrogen as fuel, hydrogen is oxidized at the anode and while O_2 is reduced at the cathode. The oxygen ions diffuse through the cathode, through the electrolyte and meets the H_2 to produce water. During the H_2 oxidation electrons are created and transported out to an external circuit thereby producing power.^{7,8}

This means that it is essential that the ions can be conducted through the cathode and electrolyte and that the materials thereby have a high ionic conductivity to ensure high efficiency.

The materials normally being used are functional materials with high ionic conductivity. These functional materials are polycrystalline solids and to understand the parameters affecting the overall performance it would be relevant to study the materials with nm-resolution to resolve grain boundaries, which are $\sim 1\text{-}2\text{ nm}$ ^{9,10}, and are the source of many discussions amongst researchers⁹⁻¹⁶.

One of the discussions is how the crystalline orientation affects the doping concentration in the grain boundary and how this impacts the overall conductivity of the material^{9,10}.

The crystal orientation of grains in polycrystalline solids have previously been studied by 3D Electron Backscatter Diffraction (3D-EBSD)¹⁷⁻¹⁹ and precession electron microscopy (PED)⁹. EBSD can map out thousands of grains giving good statistical results. Furthermore, it can be conducted in 3D by slicing the sample with a focussed ion beam. However, this technique is highly destructive. Besides, the resolution is 1-2 orders of magnitude larger than the grain boundary and it is therefore not possible to resolve the grain boundaries or do a simultaneous spectroscopic analysis to correlate chemical composition with the orientation of the individual grain boundaries. PED, on the other hand, is a Scanning Transmission Electron Microscopy (STEM) based technique and has a sub nm-resolution which enables subsequent spectroscopic analysis in the TEM. However, overlapping grains can disturb the orientation determination and as a consequence, PED is normally only conducted on one slice of material. PED is therefore useful for crystal orientation determination where a subsequent compositional analysis is wanted but the good statistics from the EBSD is lost. It would be highly beneficial to be able to combine the two techniques to conduct the orientation mapping in a non-destructive way with nm resolution in 3D. This would contribute to the fundamental understanding of the relationship between crystal orientation and overall performance.

This calls for a new way of measuring crystal orientation in the TEM. This work has focussed on applying 3D Orientation Mapping in the Transmission Electron Microscopy (3D-OMiTEM) a promising technique for nondestructive visualization of crystal orientation in 3D. Liu et al. firstly described the method in 2011 on a simulated data set and on an aluminium thin foil²⁰. More recently Wu et al. (2020) has described the method applied on a gold nano-island film²¹.

The work in this thesis is focussed on applying 3D-OMiTEM successfully on different

materials to reveal the potentials and challenges when applying the technique. After this, it is shown how Energy Filtered Transmission Electron Microscopy (EFTEM) can be used prior or subsequent to 3D-OMiTEM on the same nanofibre to study the effect of orientation on the composition of the fibre.

Finally, first steps are taken to develop a method for measuring conductivity of a fibre to add this contribution to the compositional and orientation information to fully determine the effect of the parameters on the overall performance of the fibre.

1.1 Aim

The aim of the project is to successfully apply 3D-Orientation Mapping in the TEM on polycrystalline functional materials for energy conversion devices such as SOEC and SOFC to gain information on transport properties to understand the parameters affecting overall performance.

1.2 Objectives

The objectives of this work was to conduct 3D-orientation mapping on different types of material to explore the possibilities of 3D-OMiTEM. This include applying the technique on three different materials:

1. a silver nanowire with known crystal orientations.
2. magnetic nanoflowers to study an ensemble of particles which enables thorough statistical analysis on morphology of the particles.
3. Gadolinium Doped Cerium Oxide (CGO) nanofibres used in SOCs to analyse both crystallographic orientation (as the silver nanowire) and statistics on morphology (as nano the nanoflowers) to use together with EFTEM to gain information on possible ion conduction paths in the material to understand how orientation affect the performance of the material.

Another objective was to commence the process of measuring conductivity of single nanofibres for further studies where the actual conductivity can be compared to the conductivity calculated from the 3D-OMiTEM/EFTEM results.

This can be summarized into the following four objectives

1. Develop and optimize the 3D-OMiTEM acquisition process for three different materials to find potential possibilities and challenges when applying the method

2. Apply and develop pipelines for appropriate image analysis, 3D reconstruction and segmentation analysis to extract useful information from the 3D-OMiTEM data set
3. Apply atomic-ratio EFTEM supplementary to 3D-OMiTEM for correlating orientation with doping concentration
4. Commence the process of developing a method for measuring conductivity of single nanofibres enabling comparison of actual conductivity with the conductivity calculated from the 3D-OMiTEM/EFTEM results.

1.3 Outline of Thesis

This dissertation is composed of nine chapters. This section will briefly describe the content of these, apart from this introductory chapter.

Chapter 2 presents the mathematical formalism and definitions used to describe crystallographic orientations and the tools for describing the characteristics of grain boundaries in polycrystalline solids.

Chapter 3 describes the experimental methods used in this project. The two main microscopy methods used were; 3D-Oriented Mapping in the Transmission Electron Microscope (3D-OMiTEM) and Energy Filtered Transmission Electron Microscopy.

The project has focused on applying 3D-OMiTEM. Therefore, and since it is a novel technique, the theory behind the technique will be described in detail along with the acquisition procedure and parameter calibration. Hereafter, a part of this chapter will be dedicated to describing how to work with the acquired data. This will include a description of the 3D-reconstruction procedure and data analysis.

The second part of this chapter will describe EFTEM and how to quantify the data to gain compositional maps.

Chapter 4 describes some of the considerations needed to be addressed prior to 3D-OMiTEM acquisition. This will include a discussion on suitable sample supports for different purposes and an analysis of the beam damage of the support. Furthermore, this chapter will evaluate beam damage on two of the samples used in this project namely the gadolinium doped ceria nanofiber and the silver nanorod. Finally, this chapter will cover how reducing sample tilts to reduce beam damage affect the final reconstruction.

Chapter 5 presents 3D-OMiTEM results of a silver nanowire and determines the crys-

tallographic texture of the sample. Deviations from the theoretical pentagonal twin structure helps to understand why galvanic replacement reaction sometimes stops, or happens along other directions in the rod than expected. This chapter thereby shows an example of how 3D-OMiTEM can be used to determine crystallographic texture in 3D.

Chapter 6 presents 3D-OMiTEM results of a maghemite nanoflower ensemble to analyse and discuss morphology statistics of crystallites and particles. The chapter reveals that with 3D-OMiTEM it is possible to obtain both crystallite size and particle size on a whole ensemble of particles. This enables statistical analysis of single particles and of the ensemble simultaneously.

Chapter 7 presents the results of 3D-OMiTEM and EFTEM applied on CGO nanofibers used for SOCs. The chapter will show how combining these two measurements proves to be a strong tool that can ultimately predict ion percolation paths in 3D.

Thus, **Chapter 5**, **Chapter 6** and **Chapter 7** show how 3D-OMiTEM results can be used in multiple ways to extract different information. Chapter 5 uses 3D-OMiTEM to examine crystallographic texture, chapter 6 uses 3D-OMiTEM to make a morphological analysis of crystallites and particles and chapter 7 uses 3D-OMiTEM together with EFTEM to obtain transport properties,

Chapter 8 describes the progress made for measuring the conductivity of electrospun nanofibres during this project. This chapter will describe the approaches and challenges when measuring conductivity of single electrospun gadolinium doped ceria (CGO) nanofibres.

Chapter 9 summarize the conclusions found in the previous sections and discuss future work.

Chapter 2

Mathematical Formalism and Definitions

This chapter presents the mathematical formalism and definitions used to describe crystallographic orientations and the tools for describing the characteristics of grain boundaries in polycrystalline solids.

2.1 Crystallographic Orientation

The orientation of a grain can be described by a rotation that brings the crystal lattice to coincidence with a reference. A rotation can be described by a real, orthogonal 3x3 rotation matrix with a determinant of 1. The vector \mathbf{u} can be rotated by a rotation matrix \mathbf{B} to produce a new vector \mathbf{u}' by the following equation^{22,23}.

$$\mathbf{u}' = \mathbf{B}\mathbf{u} \quad (2.1)$$

The orientation is a result of one or multiple rotations of an object with regards to a reference coordinate system. The space that describes the group of rotations in euclidean space \mathbb{R}^3 is denoted $SO(3)$ ^{22,24}.

An object can be rotated to have the same orientation in multiple equivalent ways. An example is that a rotation of $\frac{\pi}{2}$ is equivalent to a rotation of $\frac{5\pi}{2}$. Therefore, rotations are often only considered in the $[0 : \pi]$ range²³. The object in itself, in this case a crystal, can have symmetries that can further cause multiple equivalent orientations. For the cubic crystal system there are 24 symmetry operations that would cause equivalent orientation. Thus, multiplying the rotation matrix by the symmetry operations would lead to 24 equivalent orientations^{22,23}.

2.1.1 Pole Figure

The orientation of a crystallographic plane can be visualized on a hemisphere. The plane is placed at origo of the reference coordinate system, then a line is drawn with the direction normal to the plane. The line will intersect a unit hemisphere at a point p which will fully describe the orientation²³.

A 2D plot can be created by a stereographic projection of the hemisphere. This is called a pole figure. A simple stereographic projection of the positive hemisphere will project the point p to p' . For an intersection of the line, going from $(0,0,-1)$ to $p(x,y,z)$, with the plane $z=0$ the projection can be created by the following²³:

$$x' = \frac{2x}{1+z} \quad y' = \frac{2y}{1+z}, \quad (2.2)$$

where x , y , and z are the coordinates of the point p , x' and y' are the coordinates of the point in the projection p' .

However, the equation will depend on the projection plane of interest.

In the pole figure the sample direction is thus aligned to a particular crystallographic pole.

Inverse pole figure

The inverse pole figure (IPF) is the opposite of the pole figure. Here the crystallographic poles are aligned with a specific sample direction²³.

Due to symmetry of the studied crystallographic phase the IPF will also contain the symmetry. For a cubic crystallographic group the IPF can therefore be visualized by a triangle section of the pole while still showing all crystallographic orientations. This will be the fundamental zone²³.

The sample can be coloured by IPF colouring in a specific sample direction e.g. x-direction IPF colouring. Then a triangle colorbar is generated where all colors represent a specific crystallographic orientation. The orientations with reference to the x-direction is thereby uniquely coloured. This is of particular interest when it is interesting to determine if grains are textured in a specific direction e.g. along a fibre.

2.2 Characterization of Grain Boundaries

As previously mentioned we can describe the orientation of the grains with respect to a reference sample direction by e.g. IPF colouring. However, it is also possible to

characterize the material by the orientation of a grain with reference to its neighbouring grain i.e. the grain boundaries. This is called the Grain Boundary Character Distribution (GBCD)^{24,25}.

The GBCD is described by five independent parameters: Three parameters for describing the misorientation between the neighbouring grains and two parameters for describing the grain boundary plane²⁵.

The grain boundary plane is described by the Miller indices. However we only need the unit vector describing the direction of the miller indices (hkl). Two angles will therefore be sufficient. The last angle can then be determined by the euler relation: $\sin^2 \alpha + \sin^2 \beta + \sin^2 \gamma = 1$.

To describe the misorientation three parameters are necessary. A direction relative to the boundary plane (two parameters as just described) and one parameter describing the angle of rotation.

The five-parameter GBCD can be used to describe different characteristics of the material. The parameters can be visualized and analysed in three different ways²⁴:

- Misorientation Angle Distribution (MAD) (one parameter). For example see figure 2.1a.
- Grain Boundary Plane Distribution (GBPD) (two parameters). For example see figure 2.1b.
- GBCD (five parameters). For example see figure 2.2a.

The MAD is a histogram of the frequency of neighbouring grains with a specific misorientation angle between them.

The GBPD is a diagram showing the frequency of grain boundary plane normals. The frequency is normalized to the distribution of a random isotropic material. Therefore, the unit is Multiples of Random Distribution (MRD).

The GBCD is a hemisphere and describes all the orientations. A section of the GBCD can be picked for a specific misorientation. In this way a misorientation type is chosen (an axis and an angle) and the frequencies of the grain boundary normals are shown. The frequency is normalized to the distribution of a random isotropic material. Therefore, the unit is MRD. An example is shown on figure 2.2a.

The grain boundaries can be characterized by at least one of the following types; twist-, tilt-, symmetric- or 180-tilt boundaries. They are characterized in the following way²⁴:

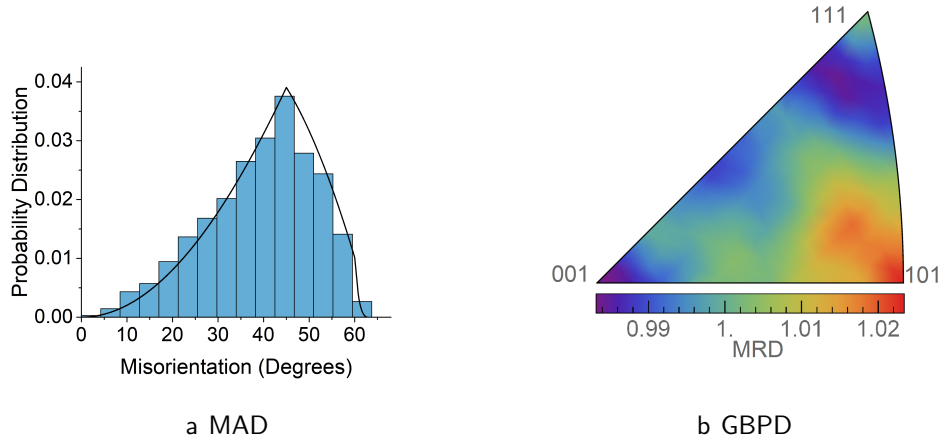
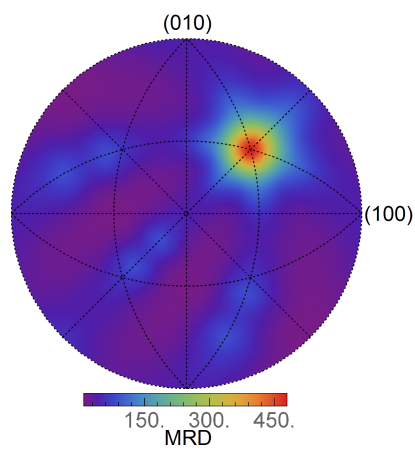


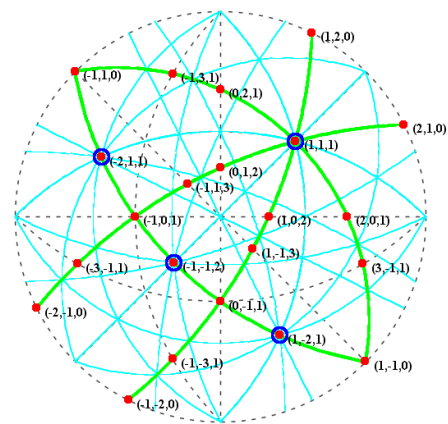
Figure 2.1: Examples of results from electrospun gadolinium doped ceria nanofibre. Left: Example showing MAD (blue histogram) and Mackenzie distribution (black line) showing orientation distribution for randomly orientated cubic crystals. Right: A GBPD.

- A twist boundary is characterized by the grain boundary plane being perpendicular to the misorientation axis i.e. $(\mathbf{u} \cdot \mathbf{m} = 1)$, where \mathbf{m} is the unit vector normal to the boundary plane and \mathbf{u} is the misorientation axis).
- A tilt boundary is characterized by having the misorientation axis in the grain boundary plane. i.e. $(\mathbf{u} \cdot \mathbf{m} = 0)$.
- A symmetric boundary is characterized by being a mirror plane. It is also a 180° -twist boundary.
- A 180° -tilt boundary is characterized by the two neighbouring crystals having miller indices belonging to different families.

By analysing the GBCD for a specific misorientation it is possible to identify what types of grain boundaries are present in the material. This can be done by constructing a diagram showing the position of the different types of grain boundaries for specific orientations. An example is shown on figure 2.2b. By comparing the diagram to the GBCD generated from the data it is possible to determine what types of grain boundaries are in the material. The diagram can be created by using the software GBtools described in reference²⁶.



a GBCD for misorientation $60^\circ/\{111\}$



b Diagram of positions of characteristic tilt- (cyan lines), twist- (red), symmetric- (blue) and 180° -tilt boundaries.

Figure 2.2: Example showing GBCD for silver nanowire and diagram showing positions of characteristic grain boundary types for cubic fcc $m\bar{3}m$ material for misorientation $60^\circ/\{111\}$ generated with GBtools²⁶.

Chapter 3

Experimental methods

This chapter aims at describing the experimental methods used in this work to obtain the results in chapter 5, 6 and 7.

3D-OMiTEM is the main method used in this work. Therefore, this chapter will have an emphasis on describing the theory behind 3D-OMiTEM working principles as well as describing the 3D-OMiTEM procedure. Hereafter, since 3D-OMiTEM is not a conventional technique yet, calibration procedure of parameters normally not calibrated regularly is described. Finally, a section is dedicated to describing the reconstruction procedure and methods for the data analysis.

The second microscopy method used in this work is Energy Filtered Transmission Electron Microscopy (EFTEM). The last section in this chapter will describe the EFTEM technique including a section describing quantification of results and lastly additional calibration procedures.

3.1 3D-OMiTEM

The objective of this work was to conduct orientation mapping in 3D with nm-resolution ($\sim 1\text{-}3$ nm) using a non-destructive technique. The TEM is well known for its high resolution and therefore serves as a good candidate for conducting the 3D orientation maps. However, the challenge of conducting 3D orientation maps in the TEM was described by Weyland and Midgley (2016) in Williams and Carter's supplementary book.

(...) we need a system where it is experimentally feasible to track such a diffraction feature through tilt. For arbitrarily oriented crystals in a similarly arbitrarily oriented, or amorphous, matrix this would be all but impossible. (...) The experimental difficulty of

*DF tomography is its central limitation. However, (...) it is potentially the only suitable technique for 3D imaging of structures (...) where the only difference between an object and its surroundings are purely structural" (...)*²⁷.

This calls for a new way of conducting orientation mapping in the TEM. This work has used the technique 3D-OMiTEM to conduct orientation mapping. 3D-OMiTEM utilizes dark-field (DF) conical scanning in combination with sample tilts to obtain combined reciprocal and direct space information²⁰. The subsequent reconstruction procedure provides orientation determination locally in the interior of the sample. The conical scanning uses beam tilt to choose diffraction rings from which dark field images are formed. Therefore, the reciprocal information is given by the beam tilt and sample rotation. We choose a specific Bragg reflection and form a DF image where the projection only shows the part of the sample with the specific diffraction condition. Each image thus constitutes a 2D-projection of the 3D grain shapes observed for a point in the reciprocal space. This is done for beam tilts along the selected ring, for 360° in 1-2° steps. Typically, each of the 5-10 inner rings in the diffraction pattern is used for every sample rotation angle. For aligning the direct space information a bright field (BF) image is recorded by setting the beam tilt to 0 (direct beam) every 10th image. The result is 70.000-200.000 images that are reconstructed into a 3D grain orientation map. The 3D-OMiTEM procedure requires a beam stable sample and support since the sample is illuminated for several hours (approx. 10 hours) depending on tilt angles, step and number of probed reciprocal space coordinates.

3.1.1 Theory behind Working Principles of 3D-OMiTEM

TEM modes

The TEM can be operated in two modes: An image mode and a diffraction mode. To switch between these two modes the intermediate lens strength is adjusted making sure either a diffraction pattern or an image appear in the viewing screen as shown on figure 3.1. The diffraction mode contains reciprocal space information of the image (direct space)²⁸. In 3D-OMiTEM we combine information from these two modes.

Dark Field Imaging

Dark field imaging is a way of choosing a part of reciprocal space to be imaged. This is done by inserting an objective aperture into the back focal plane of the objective lens. The aperture can then be used to select a diffraction spot from the diffraction pattern and only electrons that have scattered to this Bragg condition will light up in the image

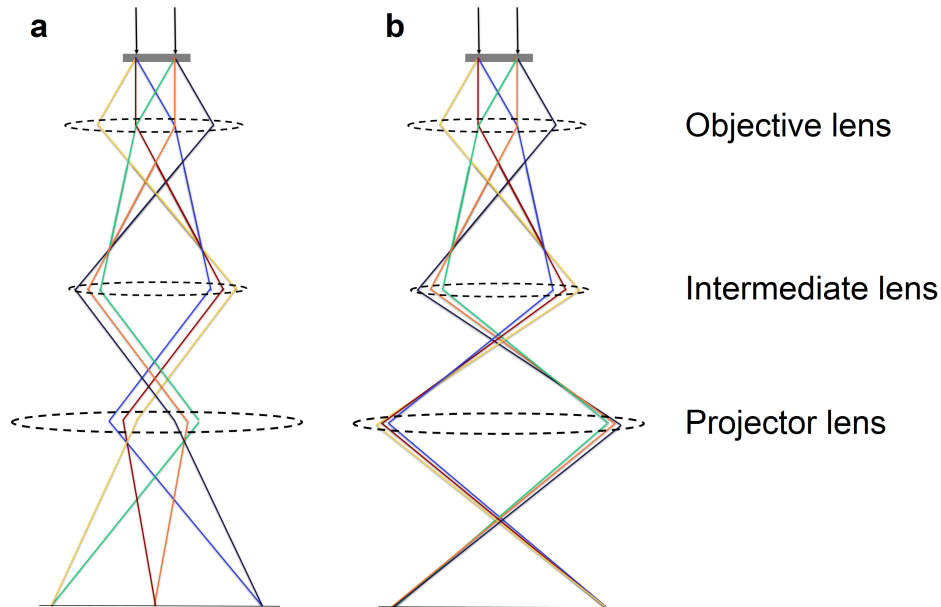


Figure 3.1: Ray diagram of TEM. a) shows the ray diagram for forming a diffraction pattern, b) show the ray diagram for forming an image.

(see figure 3.2b). If the center spot is chosen a true bright field image is formed where scattered electrons are filtered away (see figure 3.2A). Dark field imaging is the term used when any other of the diffraction spots is chosen²⁸.

If a diffraction spot is chosen by moving the aperture it is called displaced-aperture DF (figure 3.2B). However, by doing so, the electrons will travel off the optic axis which can cause aberrations in the form of astigmatism and focussing becomes more challenging. Instead it is possible to tilt the incident beam so that the diffracted spot moves to the center. This is shown on figure 3.2C.

DF imaging thereby gives the opportunity to image selected crystal planes and orientations as already mentioned in the Williams and Carter quote.

Orientation Mapping Using Hollow-Cone DF

DF imaging is a technique where we can image specific orientations, one crystal plane per image. Therefore, it is possible to do a full orientation map by systematising the DF collection. This is what 3D-OMiTEM exploits. 3D-OMiTEM uses hollow-cone or conical scanning where a whole family of planes are recorded instead of just one plane. In practice this can be done in two ways; by using hardware or software. Hardware requires an annular DF aperture where a whole ring instead of just one diffraction spot can be chosen. However, this aperture will have a fixed size and this method will therefore not be flexible. Another way is to move the aperture along the selected ring. However it is

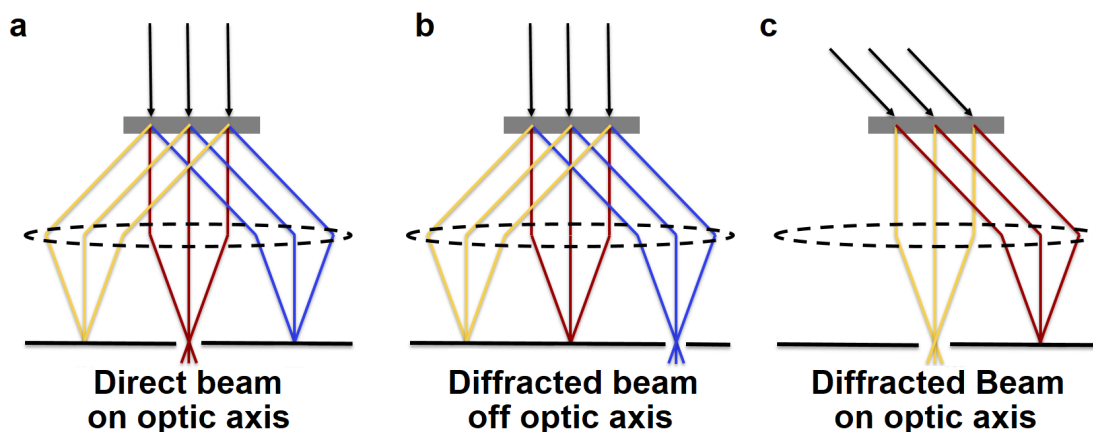


Figure 3.2: Centered Dark Field. a) formation of true BF, b) formation of DF and c) formation of centered DF by tilting incident beam. Black arrows represent the incident beam, red lines represent the undiffracted beam and yellow and blue lines represent diffracted beams.

very difficult to move the aperture with such precision and as a result it would be very time consuming. Furthermore, the aberrations caused by the electrons travelling off axis, as explained previously, would also be an issue²⁸.

Therefore, in this work, software was used to tilt the beam as in centred DF imaging making sure the whole diffraction ring was probed while collecting all images. With this method it is possible to select many diffraction spots. The result will be a whole family of images that together holds information on a set of family planes. By doing this for multiple diffraction rings we record images containing all possible orientations as can be seen on figure 3.3. This is done for multiple sample tilts to get the 3D tomographic information. By noting the sample tilt angle ω , the beam tilt angle β and ring number α for each image it is possible to reconstruct an image containing orientation information.

By using conical scanning we thus obtain a whole family of planes instead of just one DF image from one Bragg condition.

Artefacts

Artefacts are common when dealing with diffraction in TEM. Much of the theory developed for analysing diffraction patterns is based on a kinematical approach meaning that the electron beam is only scattered once²⁹. In practice this is not always true. One common reason for artefacts is double diffraction. Here a diffracted beam is re-diffracted on the same crystal planes or another set of crystal planes. This can result in very complicated patterns³⁰.

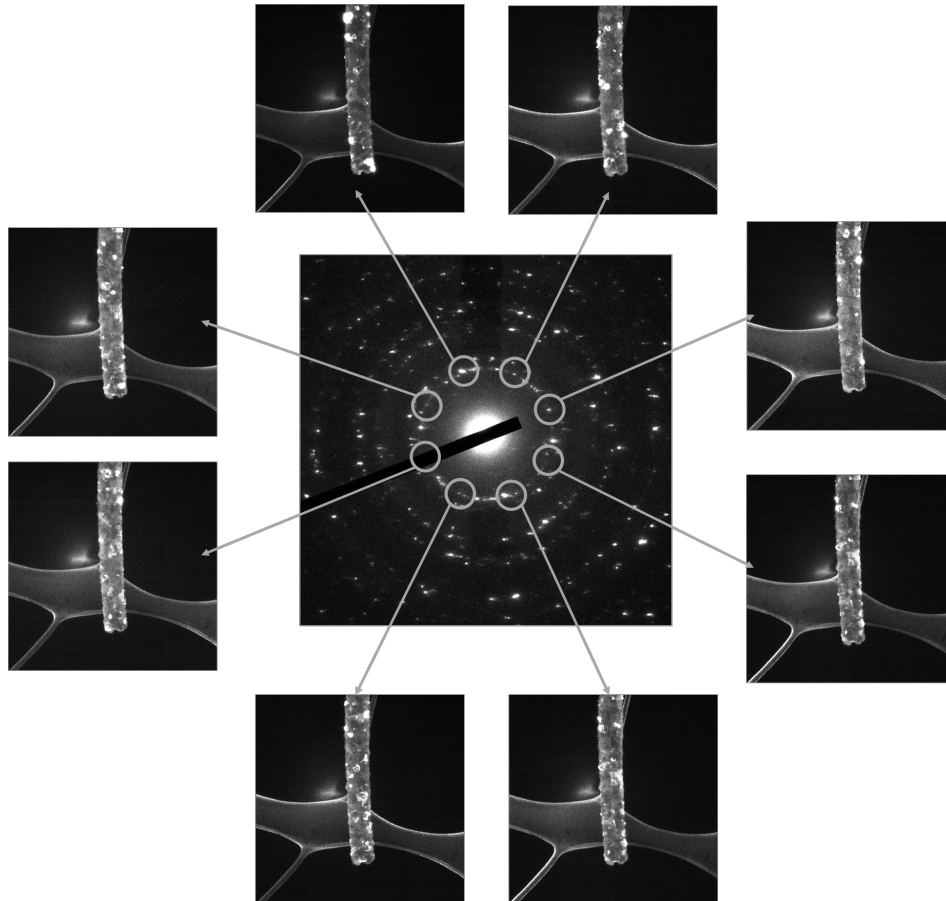


Figure 3.3: Principle of conical scanning

Another phenomena is dynamical diffraction. This gives rise to artefacts that stems from the strongly diffracted beam being diffracted back to the direct beam by the same set of planes. The beam can thereby be diffracted many times. This especially happens for thick samples. The result is that forbidden diffraction spots can appear. E.g. a scattered electron from a $(11-1)+(1-11)$ can show up as a (200) diffraction spot in the diffraction pattern even if this reflection is forbidden³¹.

This artefact can be avoided by slightly tilting the sample. When the sample is slightly off zone axis, not many reflections are simultaneously excited and the forbidden spots disappear while the true spots will stay. This can also be achieved by using a double conical rocking beam. This technique is called precession diffraction and is done by using DF coils in a circular hollow way just as in conical scanning and then de-scan the beam back onto the diffraction plane³⁰. In conical scanning it is the same effect. Since we collect a whole set of hkl -families the forbidden spots average out especially if the angle is large. Furthermore, since we also tilt the specimen we in principle get the whole diffraction in 3D and forbidden spots average out.

3D-OMiTEM procedure

As described earlier 3D-OMiTEM acquires a set of DF images from conical scanning. From these, the crystal orientation can be determined. By tilting the sample in 3D the tomographic 3D information is acquired with information from the interior of the sample.

By knowing the specific crystal parameters it is possible to calculate the positions of the diffraction rings and it is only necessary to probe these. To check if the rings are as expected, normally a diffraction pattern is recorded prior to 3D-OMiTEM acquisition and the ring positions are determined. Once the rings are selected for probing it is crucial to make sure that the objective aperture is centred. The easiest way to do this is to insert the objective aperture while in diffraction mode. Here the aperture should be centred around the center spot. In image mode it is now possible to spread or condense the beam making sure that the aperture is not shading. A finer centring is done by the software by using beam shift while recording a BF image. First the software shifts the beam in the x-direction and then in the y-direction. The center is then chosen by choosing the beam shift used to create the image with highest counts (no shading). This should be repeated at least three times. The centring of the objective aperture should be done for every sample tilt as the stage tilt can affect the position of the aperture.

Now, in principle everything is aligned provided that normal microscope alignment has been done and the microscope is ready for 3D-OMiTEM acquisition. The ring locations are simply input.

The 3D-OMiTEM is set up to do multiple steps in order to automatize the acquisition requiring minimal assistance once the software is started. The following steps are done for every sample tilt: 1. focussing, 2. tracking, 3. search (optional) and 4. exposure.

In the *focussing* step the image is auto focussed. This is done by applying a small beam tilt and recording how the image shifts. By minimizing this shift while changing the focus, the sample is auto-focused. After this, the objective aperture should be centred but this is optional.

In the *tracking* step the position of the object in the image is compared to the position from the previous sample tilt. This is done to avoid the sample moving out of the field of view. Any potential movement is corrected with a rough image shift. If the movement of the sample is larger than what an image shift can correct for, it is necessary to use the stage to move the sample. If the stage shift option is set the "search" step will be mandatory.

If the image shift, necessary to center the sample, is above a set limit the search step

will shift the stage. Then it will be re-focused and re-tracked.

The final step is the *exposure*. The previous steps have made sure the sample is in focus, the aperture is centered and the sample is centered. Now the actual acquisition can start where the beam tilt is used to record all DF and BF images.

For information on more specific options read the acquisition manual (appendix).

After the acquisition, it is possible to reconstruct a rough diffraction pattern for each voxel and thereby determine the orientation. In practice this is done with an in-house developed software. The software creates a confidence index. If many images point to a specific orientation, a high confidence is achieved. If on the other hand, the sample is too thick the information from the interior of the sample will have a low confidence index while it remains high at the boundary where the sample is thinner.

3.1.2 Calibration

3D-OMiTEM is not yet a standard TEM technique and therefore some parts of the microscope normally not used should be calibrated.

Since software is used to control the beam tilt it is essential that it is correctly calibrated. If not calibrated correctly the beam tilt will not shift in a circular path selecting all rings but rather an elliptical shape resulting in wrong or even black images (see figure 3.4).

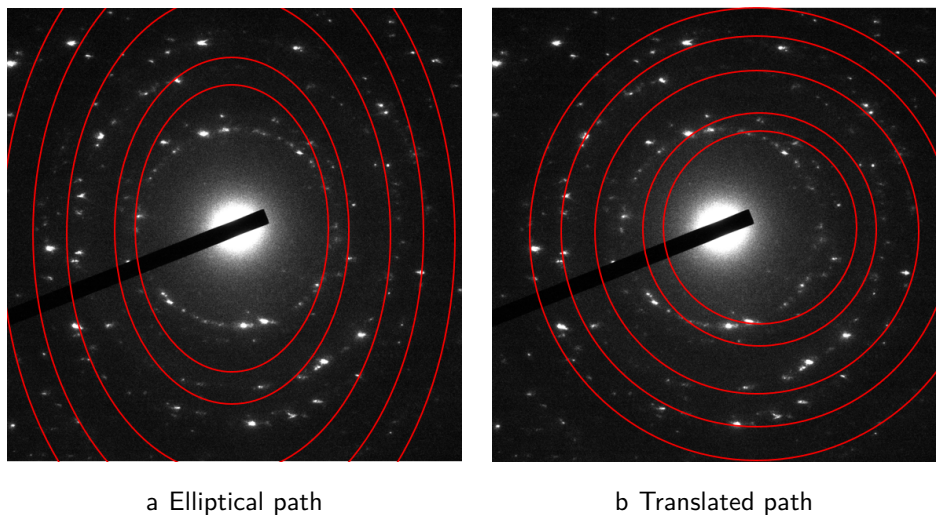


Figure 3.4: Effect of non-calibrated beam tilt

The beam tilt is controlled by a set of deflector coils. To calibrate the beam tilt correctly these dark-field deflector coils above the objective lens are calibrated. This is done by following the steps:

1. Create a diffraction pattern
2. Center the center spot using the projector lens
3. Insert the beam tilt angle corresponding to the first ring. Then correct with the dark-field deflector in x and y until the part of the ring is in the center.
4. Change the azimuthal angle (deg) to see the diffraction pattern move around in a ring. Correct with x and y until you see a circular shape following the selected ring
5. Repeat 3 and 4 until satisfied.

Since the software used for the 3D-OMiTEM acquisition is not standard, it needs to be calibrated for every magnification used. The 3D-OMiTEM software automatically tracks the sample and uses image shift in combination with stage shift to center the image after each tilt. If this is not correctly calibrated it will result in the sample shifting out of the field of view and the software will try to correct for this with a mix of sample control, beam shift and image shift. Finally, this results in the software failing and the microscope being very misaligned with the beam far out of the viewing screen. It will often be necessary to load old alignments. Therefore, it is good practice so save an alignment file before 3D-OMiTEM acquisition. This effect can also be seen if the tilt step is too high or the eucentric height is not correctly set. Then the sample can shift out of the field of view resulting in the same problems as a mis-calibrated stage or image shift. Therefore test this before redoing calibrations.

If stage shift is enabled it is furthermore important that the threshold for when to use stage shift or image shift is set correctly. If the threshold is set too low the stage will keep correcting in a loop until satisfied which can be infinity if the threshold is too low. If the threshold is set too high the image shift will shift until no beam is visible in the imaged area resulting in a black image. The software will fail.

To find the correct threshold follow the steps:

1. Set the microscope as to acquire 3D-OMiTEM (see manual in appendix).
2. Note the image shift.
3. Shift the beam using image shift. Note the image shift when the beam is no longer visible.
4. Test what the maximum image shift is. The software will stop when it cannot be shifted any more.

The limit should then be set as $L = \frac{IS_c - IS_{edge}}{IS_{max}}$, where IS_c is the image shift when the image is centred, IS_{edge} is the image shift when the beam is no longer visible and IS_{max} is the maximum shift. This should be done every time microscope settings are changed.

3.1.3 Reconstruction

This section will describe some of the theory behind the reconstruction procedures. For details on the reconstruction procedure read the reconstruction manual in the appendix.

Image processing

The 3D-OMiTEM reconstruction is done from the DF images. The BF images are used only for drift correction and masking the outer boundary.

The images should be aligned in order to make a tomographic reconstruction. This can be done in numerous ways and there exists a number of papers with different approaches. The approach used in this work has been to use filtered BF images and align them using image cross-correlation³². After aligning the BF images the DF images are corrected with a linear interpolation between the shifts for correcting the BF images. This approach assumes that the shifts do not experience any sudden moves and is sufficient for this purpose.

Another parameter important for a good reconstruction is the rotation center. This is also found using the BF images. As with conventional X-ray tomography a slice is reconstructed and the reconstruction is evaluated. By minimizing wrong rounded elongated shapes the rotation center is found. In the TEM the rotation direction will be in the stage direction. This is specific for the magnification and TEM. For the TEM and magnification used in the project, the images should be rotated 23 degrees to get a correct reconstruction. Hereafter the rotation center can be found.

For the tomographic reconstruction this is sufficient. However in order to achieve crystal orientation a few more steps are necessary.

The reconstruction algorithm works on binarized DF images. Or said in another way; either the grain lights up and fulfil the probed Bragg condition or it does not. Therefore, all images need to be binarized. If the threshold is set too low the background will give noise to the orientation determination. Noise will be even more severe due to diffuse scattering from the support especially when using amorphous support. However, if the threshold is too low there will be missing information from parts where the sample is thick. To avoid this, it is possible to use a low threshold for the interior of the sample

and higher threshold close to the sample boundary. However, this is still an assessment during sample reconstruction.

The aligned and binarized images can now be used to reconstruct the orientations in each voxel.

Orientation reconstruction

To determine the possible orientations, the binarized DF images are used and marked with the acquisition parameter ω , β and α (i.e. $\{hkl\}$ -family). Each voxel in the reconstructed volume contain the same information as in a diffraction pattern. In practice each voxel is recorded by probing reciprocal space and for specific ω , β and α -parameters the voxel light up. When it light up it corresponds to a spot in the diffraction plane. The diffraction pattern is constructed in each voxel.

From the diffraction pattern it is possible to determine the orientation by pattern indexing. The reconstruction software for 3D-OMiTEM is based on forward modelling based indexing which has proven to be better than backward modelling for noisy data²².

The method behind the orientation reconstruction is described in detail by Larsen and Schmidt (2017)²². The following is based on this reference.

The forward modelling based indexing is also called dictionary indexing as the method compares a dictionary containing diffraction patterns of orientations and compares to the experimentally recorded diffraction patterns. The indexing can be divided into three steps:

1. A set of orientations are selected.
2. Diffraction patterns are simulated for the set of orientations.
3. The simulated diffraction patterns are compared to the experimental diffraction pattern and the most likely orientation is chosen.

Since all experimental patterns have to be compared to all dictionary orientations the method is computationally demanding. Therefore, it is beneficial to reduce the numbers of dictionary orientation by choosing an optimal set of orientations.

Optimal set of orientations

The orientation of a grain can be described by a rotation that brings the crystal lattice to coincidence with the sample reference. This can be described by a rotation and a rotation axis. The space that describes the group of rotations in euclidean space \mathbb{R}^3 is denoted $SO(3)$ ²²⁻²⁴.

The rotation can be described by an angle θ around a unit vector axis i.e^{22,23}.

$$\mathbf{u} = u_x \mathbf{i} + u_y \mathbf{j} + u_z \mathbf{k} \quad (3.1)$$

In the quaternion representation this is written as:

$$\mathbf{q} = \exp\left(\frac{\theta}{2} (u_x \mathbf{i} + u_y \mathbf{j} + u_z \mathbf{k})\right) = \cos \frac{\theta}{2} + (u_x \mathbf{i} + u_y \mathbf{j} + u_z \mathbf{k}) \sin \frac{\theta}{2} \quad (3.2)$$

Thus \mathbf{q} is a four dimensional vector and can be written as $\{w, ix, jy, kz\}$ where w x y and z are real numbers and \mathbf{i} , \mathbf{j} , \mathbf{k} are complex numbers that can be interpreted as unit-vectors pointing along the three spatial axe^{22,23}.

Unit quaternions, where $\sqrt{w^2 + x^2 + y^2 + z^2} = 1$, are points on a four-dimensional hypersphere. The space describing these points are denoted \mathbb{S}^3 and is the double covering of $SO(3)$ since \mathbf{q} and $-\mathbf{q}$ represents the same orientation.

To find the optimal set of dictionary orientations we need to find the optimal distribution of a set of points on the \mathbb{S}^3 space.

To evaluate if the set of orientations are good or bad, an error estimation is made by calculating a covering radius. The optimal set of orientations will have a minimal covering radius. To find the covering radius for the set of N points $\mathbf{P} = \{p_1, p_2, p_3 \dots p_N\}$ the following steps are done:

1. The \mathbb{S}^3 space is divided by delaunay triangulation. The vertices will then correspond to the points \mathbf{P} (see figure 3.5a for example in 2D space).
2. The voronoi cells are found for each point in \mathbf{P} : The vertices are the circumcentre of the delaunay triangles (see figure 3.5b).
3. The covering radius is found. It corresponds to the maximum distance between the voronoi vertices and its corresponding point in \mathbf{P} i.e. the triangle vertex (see figure 3.5c).
4. The maximum radius corresponds to the covering radius.

For crystallographic point groups with high symmetry it is not necessary to cover the whole \mathbb{S}^3 hypersphere. Therefore symmetry operations are applied depending on what crystal structure the material of interest has to make sure only the fundamental zone is covered.

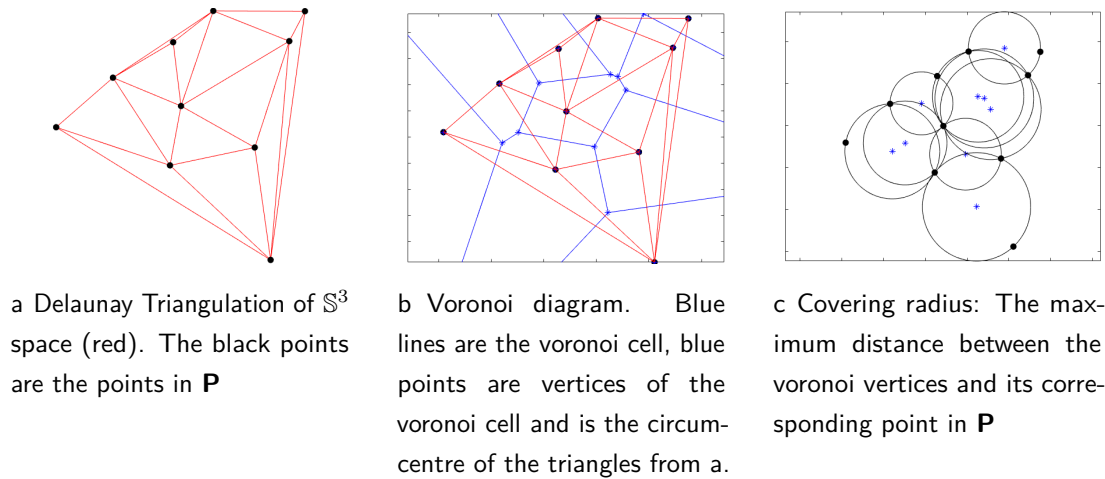


Figure 3.5: Example of finding the covering radius. The example is shown in 2D but is similar for \mathbb{S}^3 .

Computation of orientation sets

The procedure for computing the dictionary orientation sets is presented in the following:

1. The initial choice of the set of orientations, i.e. points \mathbf{P} on \mathbb{S}^3 , is found by random sampling of $SO(3)$.
2. The distribution of points \mathbf{P} are optimized by minimization of the Riesz energy i.e. the energy of the configuration of points. This makes sure we have an optimal distribution of points which reduce the covering radius.
3. The delaunay triangulation is smoothed. The minimization of the Riesz energy only considers the relative position of the points. However, by creating a smoother triangulation the covering radius can be further optimized.
4. The local orientation, i.e. the position of the vertices, are optimized by an iterative refinement.

For further information on the steps refer to²².

Once the dictionary orientations are generated, for the desired material, diffraction patterns can be simulated and compared to the experimental diffraction patterns. The most likely orientation can then be chosen.

Finally, the ratio between the observed diffraction-vectors and the dictionary are calculated and assigned to the individual voxel as a confidence index.

3.1.4 Data Analysis

The analysis of the 3D-OMiTEM data is mainly done in Matlab and Dream3D. Dream3D is a software developed for EBSD but apart from the scale the 3D-OMiTEM data contain the same information as conventional 3D-EBSD data. DREAM3D consists of multiple ready-made filters or functions that are combined into a pipeline. To make sure the data format is readable for Dream3D the data should be converted with a Matlab script developed as part of this project. For further information see appendix.

Segmentation

Segmentation is done by grouping voxels with orientations closer than a set threshold. The segmentation is used to define what a grain is for later structural analysis. Then it is possible to extract statistics of the grains. For some techniques for example X-ray tomography it can be necessary to filter the structure before segmenting because of noise. However, in all samples in this work this has not been necessary. However, filtering was done after segmentation to remove small segmented grains.

Image Analysis

Filtering is done to remove small noise of poorly indexed grains. This could either be seen as voxels with low confidence index or very small grains in the middle of another well defined grain. The threshold can be found from a histogram. By plotting a size histogram, it is obvious if noise is present in the data. This will show as a very high narrow peak around 0. The threshold is then set between the very high peak and the smaller peak with the correct size distribution

To create the size distribution the equivalent diameter is calculated for each grain. The equivalent diameter is computed from the volume of the grain by counting how many voxels belonging to a grain. From this a sphere with the same volume is computed and the diameter is calculated. After filtering the structure can be analysed by extracting morphological- or crystallographic information and performing statistical analysis of the grains. This could include but is not restricted to grain size distribution, shape analysis, distance maps, clustering analysis or missing wedge analysis.

Supplementary to characterizing the structure of the grains, it is possible to analyse the sample in terms of the grain boundary. 3D-OMiTEM does not as such resolve the grain boundary but the grains. However, by comparing two neighbouring grains it is possible to determine the misorientation of the GB. This is done by creating a neighbour list. Each neighbour is assigned with a grain id and a list of which grains are neighbours

is created. With this list all neighbouring orientations can be compared and since the crystal structure is known, it is possible to determine the misorientation applicable to many problems. For an example read the results on CGO fiber in chapter 7.

For polycrystalline samples the orientations can be characterized by comparing the orientation distribution to the one of a random thereby determining if any texture in the sample is present. For a random isotropic cubic structure the distribution follows the Mackenzie distribution³³. If the distribution resembles this, the sample does not have texture. Other analysis using geometric or orientation parameter or a comparison of these can also be done from this.

Meshing

To characterize the grain boundaries further it is possible to create a mesh with the faces of the grains i.e. the grain boundaries. Then statistics can be extracted of these. To do this firstly the grains are smoothed as small changes will give misleading information. Then the faces are triangulated thereby creating a mesh of triangles describing the faces. From this, other types of orientation analysis can be done easier since it allows sampling of the GB. This enables calculation of the GBCD and analysis as described in chapter 2.

3.2 Energy Filtered Transmission Electron Microscopy (EFTEM)

Energy filtered transmission electron microscopy (EFTEM) can be used to map electrons which have lost a specific energy. This can be used to do elemental mapping.

When electrons pass through the sample they either lose no energy or have suffered from inelastic scattering. In Electron Energy-loss spectrometry (EELS) the energy distribution of the electrons after passing through the sample is mapped into a spectrum. By analysing this spectrum, it is possible to say something about the sample's elemental- and chemical composition as well as the physical state³⁴.

In Energy Filtered Transmission Electron Microscopy (EFTEM) we select electrons with a specific energy-loss range and create an image of these. EFTEM thereby makes it possible to create images containing elemental-, chemical- or physical state information. To produce an elemental map, energy range is chosen around the ionization edge³⁴. However before this image can be used for quantification it is necessary to go through some steps.

3.2.1 Quantification

First of all the electron-energy loss spectrum has a background. The images acquired by EFTEM will contain this background. To correct for this it is necessary to collect two pre-edge images to create the background and one post-edge image. This is called the three-window method. The background intensity has the form $I(E) = AE^{-r}$ and the exponents are found by the following two equations^{32,34}:

$$r = \ln\left(\frac{I_1}{I_2}\right) / \ln\left(\frac{E_1}{E_2}\right) \quad (3.3)$$

and

$$\ln A = \frac{1}{2} \left[\ln\left(\frac{I_1}{I_2}\right) + \ln\left(\frac{E_1}{E_2}\right) \right] \quad (3.4)$$

I_1 is the intensity of the first pre-edge image, I_2 is the intensity of the second pre-edge image, E_1 is the energy at which image 1 was acquired and E_2 is the energy from which image 2 was acquired. The background contribution I_b to each pixel can then be found by integrating $I(E)$ over the energy range Δ .

After subtraction of the background, the image will show the integrated edge intensity. However, since EFTEM is normally operated in TEM mode it will suffer from diffraction and thickness effects. To remove these artefacts and get a quantification it is in principle necessary to get a low-loss image and use the following equation^{32,35}:

$$N = \frac{I_K(\beta, \Delta)}{I_{low}(\beta, \Delta)\sigma_K(\beta, \Delta)} \quad (3.5)$$

In practice this is not possible with the microscope used in this project. The two images need to be acquired under the same conditions. If the illumination is optimized for the core-loss region it will not be possible to acquire the low-loss region without saturation of the CCD. On the other hand if the illumination is optimized for the low-loss region the core-loss region will suffer from too low counts.

Instead it is possible to achieve quantifiable atomic ratio maps. If the edge shapes are similar, the illumination conditions and integration range is the same for the two elements, the diffraction and thickness effects will cancel out and it is no longer necessary to map the low-loss region. Then the elements can be quantified by³⁵:

$$N = \frac{I_A(\beta, \Delta)\sigma_B(\beta, \Delta)}{I_B(\beta, \Delta)\sigma_A(\beta, \Delta)} \quad (3.6)$$

3.2.2 Condenser Correction

When performing EFTEM an offset is applied to the high tension. This ensures that the energy-loss image remains at focus since the energy of the electrons will be the same as when aligning the microscope. However because of this, the illumination convergence and position on the sample will change. This will look like the beam is being condensed or spread and the illumination disk will become visible in the image (see figure 3.6). For large energy-loss this will be a significant problem and it needs to be corrected with a "condenser correction" and can be done with the EFTEM software. This is done first noting the illumination area, then applying the offset and applying the correction until the illumination area is constant.

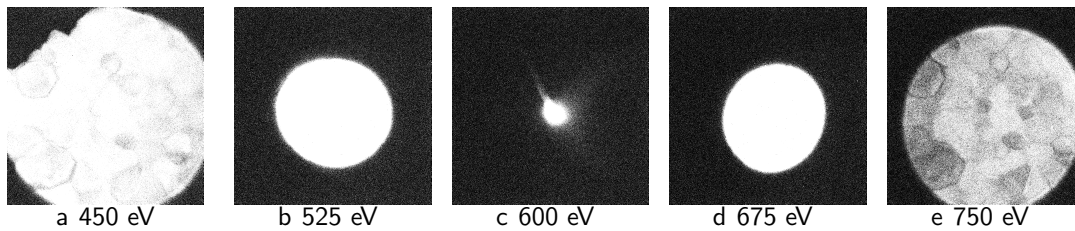


Figure 3.6: Uncalibrated condenser correction

Chapter 4

OMiTEM Parameter Testing

The aim of this chapter is to describe and show some of the challenges in regards to sample degradation during OMiTEM acquisition and provide some examples of what effect it has on the reconstruction to change the acquisition parameters.

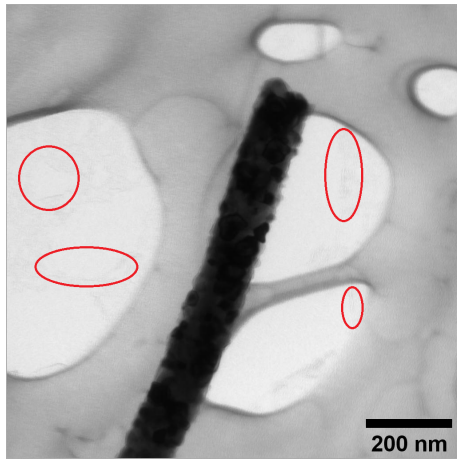
In the 3D-OMiTEM acquisition hundreds of thousands (70.000-200.000) images are recorded. Therefore, the sample is typically illuminated for several hours (5-20 hours) depending on the chosen acquisition parameters. This requires that both the sample and sample support is stable enough during beam exposure to avoid beam damage. Most TEM sessions are not longer than 4-8 hours and even then, the same area of the sample is rarely illuminated during the whole session. Therefore, sample that otherwise seem to be stable can unexpectedly show beam damage during the acquisition. If this is the case, the acquisition parameters can be modified to reduce illumination time.

4.0.1 Beam Damage on Sample Support

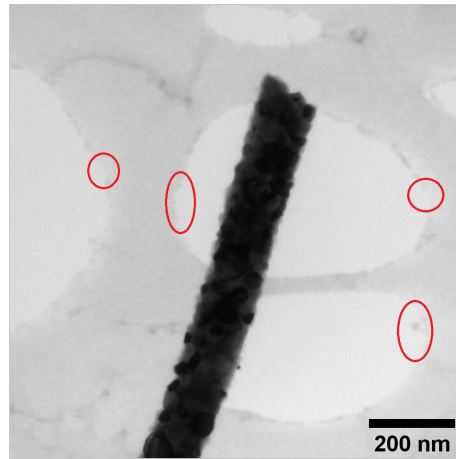
Beam damage was tested on different sample support in order to find a sample support which is beam stable for high exposures over several hours. The first test was done on a conventional copper grid with amorphous holey carbon covered with an extra amorphous ultrathin layer of carbon. The idea of this type of sample support was that the extra carbon layer would reinforce the support.

The sample was tested by starting a normal OMiTEM acquisition. Figure 4.1 presents bright-field TEM images of a CGO fiber recorded during the OMiTEM image acquisition at 1, 6, 10 and 11 hours after starting the image acquisition i.e. after alignment and setting up for OMiTEM.

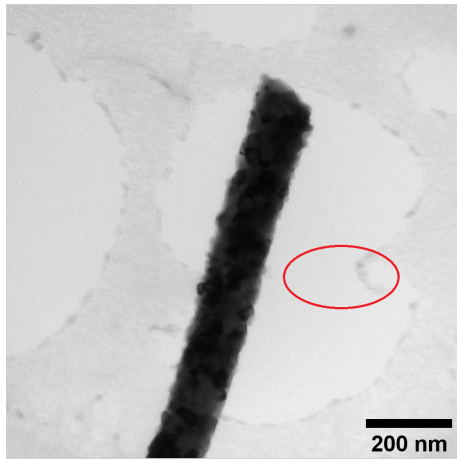
The image sequence in figure 4.1 shows that the sample support starts to disappear



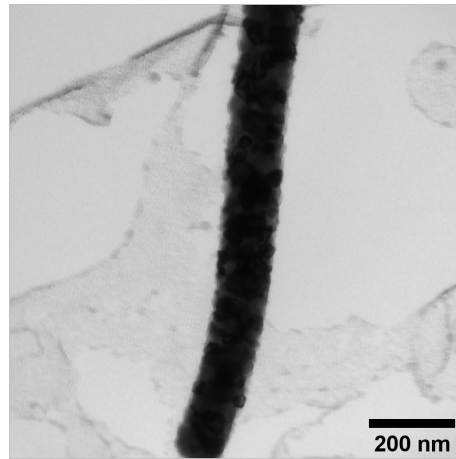
a 1 hour exposure. Ellipses indicate the areas with damaged ultrathin carbon support.



b 6 hour exposure. Ellipses indicate the areas with damaged holey carbon support.



c 10 hour exposure. Ellipse indicate a piece of the holey carbon between two holes starting to degrade.



d 11 hour exposure

Figure 4.1: Beam damage on ultrathin Carbon on holey Carbon. Red ellipses show areas where the sample support has disappeared.

indicated by the red ellipses. Already after one hour on figure 4.1a the ultrathin carbon start to degrade. Hence the ultrathin carbon is not contributing to the stability after one hour. After six hours (figure 4.1b) the holey carbon start to degrade indicated by red ellipses. The holey carbon is damaged from the edge of the holes and slowly works its way in. After 10 hours (figure 4.1c) a piece of the holey carbon between two holes is damaged so severe that it breaks indicated by red ellipse. However, the sample at this point is still stable and do not suffer from any unwanted movements (because of missing support). After 11 hours the support is so severely damaged that the sample is no longer stable and moves around during acquisition. From here on the images are useless for

OMiTEM reconstruction as we no longer know the position of the sample (rotation and translation). From the results it is concluded that holey carbon or holey carbon with ultrathin carbon clearly shows evidence of beam damage. As a consequence, it is not recommended to use these types of supports for OMiTEM with acquisition for more than 10 hours.

The OMiTEM acquisition takes approximately seven minutes per tilt when mapping the six inner rings with a beam tilt step size of two degrees and exposure time of 150ms. This means that during 10 hours it is possible to acquire approximately 85 tilt steps. However, due to the degradation early in the acquisition it is possible that the sample experience unwanted movements. However, this has not been tested in this work. As a conclusion it is not recommended to use carbon supported grids unless only very few tilt steps are required e.g. if 3D information is not required or if only few points in reciprocal space are probed.

The more stable commercial 50 nm silicon nitride support on a 200 μ m silicon frame for TEM was tested. The silicon nitride support had a window size of 0.5x1.5 mm designed for high-tilt tomographic applications enabling imaging with up to 75° tilt. The silicon nitride showed no signs of degradation not even after acquiring two full OMiTEM datasets. This is shown later in chapter 7 in figure 7.7. The silicon nitride support was therefore chosen for most acquisitions. However for some applications e.g. EFTEM or EELS it is necessary to have holey areas of the sample in order to calibrate the zero-loss peak. In such cases holey carbon support was chosen and care was taken not to expose the sample for long hours by adjusting the acquisition parameters compromising the 3D information.

4.0.2 Beam Damage on Sample

In this work three different types of samples were investigated; a silver nanowire, γ -Fe₂O₃ magnetic nanoparticles and gadolinium doped ceria (CGO) nanofibres. Every time a new type of sample is investigated it is necessary to check how much the sample has been damaged during the OMiTEM acquisition. BF images recorded as part of the OMiTEM-acquisition can be used for this. As shown later in chapter 7, in figure 7.7, beam damage on CGO was not observed for any of the measurements. However, the silver nanowire showed beginning signs of degradation as presented on figure 4.2.

The image sequence in figure 4.2 shows that after two to three hours the silver nanowire starts to have bumps on the surface indicated by red rings. Since the nanowire had a smooth surface without these bumps prior or at the beginning of the acquisition this

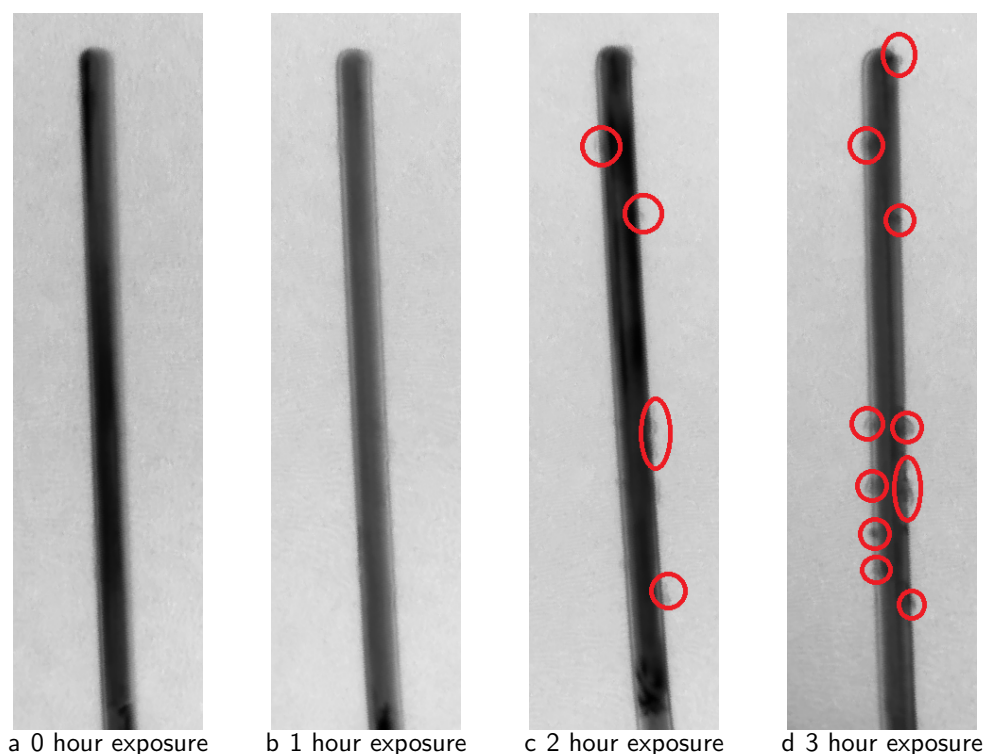


Figure 4.2: Beam damage on Ag nanorod indicated by red rings

indicates that the sample has changed during beam exposure and are thus signs of beam damage. Because of this, considerations on minimizing total beam exposure by changing the acquisition parameters need to be addressed. Normally, beam exposure can be reduced by choosing a larger spot size. However, in the case of OMiTEM there is an optimal spot size which produces the most parallel beam. Therefore, the spot size cannot be chosen randomly. Another solution could be to choose a smaller condenser aperture. This should be tested in future work. Finally, it could be exploited that the silver nanowire only has five different crystal orientations by only probing these in the reciprocal space reducing the beta tilt steps. To do this, an analysis of the diffraction pattern should be conducted before the full OMiTEM acquisition. With this knowledge it will be possible to acquire more tilt angles with a higher β step. This should be done in future work.

4.0.3 Resolution and Acquisition Parameters

If 3D information is necessary for the study when the sample suffers from beam damage, it is possible to adjust the acquisition parameters with the purpose of reducing total beam exposure time. In this section a CGO nanofiber sample is reconstructed with reduced β steps and ω steps to see how it affects the resolution of the final reconstruction.

The results is shown in table 4.1. The middle column in table 4.1 shows the sample with normal acquisition parameters with a sample tilt of [-60:+60]. It shows the most accurate crystal orientations. Here the grains are well defined and only a small missing wedge effect, seen by only small elongations of the grains, is present.

In the left column in table 4.1 the number of image projections used for the reconstruction are reduced by reducing the sample tilt range to [-30:+30]. This reconstruction contain more obvious missing wedge effects as elongations or the grains are present in the xz planes. Because of the elongation some of the grains with smaller confidence index are shadowed resulting in some grains not being segmented.

In the right column in table 4.1 the number of image projections used for the reconstruction are reduced by increased tilt step to 4°. Here the missing wedge effect is reduced compared to left column and the positions of the grains are more similar to the middle column. However, the reconstruction suffers from more noise which, if severe enough, could result in some grains not being segmented as they could be mistaken to be noise. Some grains are even difficult to see.

Changing the acquisition parameters naturally change the resolution of the tomographic reconstruction and the elongation. The best resolution of the tomographic reconstruction, that can be obtained from the acquisition parameters, can be calculated by Crowther's criterion³⁶ (equation 4.1). Crowther's criterion is a measure of the resolution as a function of number of projections in the absence of noise.

$$d = \frac{\pi D}{N} \quad (4.1)$$

where d is the resolution, D is the diameter of the volume to be reconstructed and N is the number of projections. However, the elongation due to the missing wedge also change the resolution. The elongation factor (equation 4.2)³⁷ is a measure of how much the missing wedge contributes to the change in resolution.

$$e = \sqrt{\frac{\omega_{max} + \sin \omega_{max} \cos \omega_{max}}{\omega_{max} - \sin \omega_{max} \cos \omega_{max}}} \quad (4.2)$$

where e is the elongation and ω_{max} is the maximum tilt angle and the total resolution will correspond to $d_{total} = de$

The resolution and elongation when using the acquisition parameters from table 4.1 are summarized in table 4.2 assuming a mean object diameter of 35 nm as found by X-Ray Diffraction (XRD) (This sample will be further described and analysed in chapter 7). In this table the directions, x , y and z are the same as shown in table 4.1.

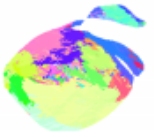
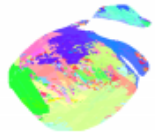
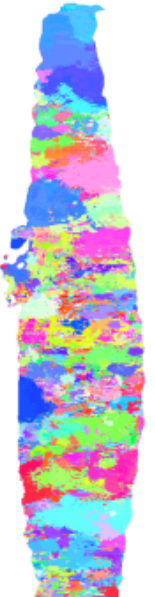
	ω range: ± 30 Stepsize: 2°	ω range: ± 60 Stepsize: 2°	ω range: ± 60 Stepsize: 4°
xy			
xz			
yz			

Table 4.1: Effect of acquisition parameters

	$\omega: \pm 30$, stepsize: 2°	$\omega: \pm 60$, stepsize: 2°	$\omega: \pm 60$, stepsize: 4°
d_z, d_y	3.5	1.8	3.5
d_x	11.72	2.80	5.50
e_{xy}	3.25	1.55	1.55

Table 4.2: Resolution and elongation for different acquisition parameters. The resolution is calculated by Crowther's criterion³⁶ and the elongation factor is calculated as by Radermacher³⁷. d_i is the resolution in the i 'th direction in nm, e_{ij} is the elongation factor in the ij -plane.

Table 4.2 shows that decreasing the number of projections from 61 to 31 decrease the resolution from 1.8 nm to 3.5 nm. Furthermore, the elongation only increase if the maximum sample tilt is reduced. Reducing the sample tilt range from $w_{max} = 60^\circ$ to $w_{max} = 30^\circ$ decrease the resolution dramatically in the x-direction from 2.8 nm to 11.7 nm resulting in elongations in the xy-plane and xz-plane.

The best possible resolution for the 3D-OMiTEM acquisitions of the three samples studied in this work are summarized in table 4.3 and are calculated based on the crystallite sizes found throughout this dissertation and the acquisition parameters.

	Silver nanowire	Maghemite nanoflowers	CGO nanofibre calcined for 1 hour	CGO nanofibre calcined for 10 hours
d_y, dz (nm)	1.0	0.31	1.3	1.5
d_x (nm)	3.1	0.5	1.6	1.9

Table 4.3: Best possible resolution for different samples and their acquisition parameters

From table 4.3 we see, that the resolution is the best for the maghemite nanoflowers. This is because their mean size is ~ 6 nm compared to 30-35 nm for the CGO nanofibres. However, the resolution for the maghemite nanoflowers are smaller than the pixel size which was ~ 1 nm for this acquisition. Therefore, the resolution will in this case be limited by the pixel size and not the reconstruction.

In conclusion the acquisition parameters highly affects the final resolution of the tomographic reconstruction and should be chosen according to what information is required for the specific study. If e.g. the sample is thin and not many grains are on top of each other the optimal way of reducing the total exposure is to reduce the sample tilt range. If on the other hand it is important to get the positions of all grains the more useful method would be to increase the sample tilt step. However if a diffraction pattern reveals

that the β tilt step could be reduced without loss of orientation information, this should preferably be done before reducing the number of tilt steps.

Chapter 5

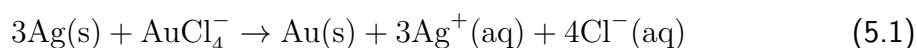
Crystallographic Texture of Silver Nanowire for Galvanic Replacement

5.1 Introduction

The Galvanic Replacement Reaction (GRR) is an efficient method for controlling morphology, structure and composition of metal nanostructures^{38–40}. This can be exploited to create hollow metal structures for applications in e.g. energy devices. The hollow structures have a larger surface-to-volume ratio decreasing the non-reactive volume. This is particularly interesting when working with scarce noble metals. Furthermore, this have proven to enhance ion-conductivity and catalytic activity^{39–42}. Understanding the parameters in the galvanic replacement reaction can help to understand and support development and optimization of such materials.

In the galvanic replacement reaction a mono-metallic nanostructure is used as a sacrificial template together with precursors of a metal with higher reduction potential. When oxidizing the template the metal in the nanostructure is oxidized while the precursor is reduced ultimately forming a hollow nanostructure^{38–40,43–45}.

An example of the GRR is the oxidation of a silver nanowire with an aqueous gold(III)chloride solution (HAuCl₄). This has the reaction:^{38–40,43–45}



In this reaction the Ag nanowire is replaced by a hollow Au nanotube. The replacement or etching favours the facets with highest surface energy and since $\gamma\{111\} < \gamma\{100\} <$

$\gamma\{110\}$ the etching starts from the $\{100\}$ and $\{110\}$ planes^{40,46}. Thus, to predict the etching of the Ag nanowire, it is necessary to understand the crystal structure and orientation of the facets in the nanowire.

Theoretically the Ag nanowire has a fivefold $\{111\}$ twin geometry with five $\{100\}$ outer surfaces as shown on figure 5.1a. The common longitudinal axis for all five triangular crystalline sections (see figure 5.1b) are along the $\langle 101 \rangle$ crystalline direction^{38,47,48}. The five crystalline segments are each rotated 70.53° around the $\langle 101 \rangle$ axis as shown on figure 5.1b which corresponds to a rotation of 60° around the $\langle 111 \rangle$ axis which is the definition of twinning. However, the five 70.53° does not make up the 360° rotation and as a result there is a solid angle deficiency. Previous studies suggests that strain compensates for this deficiency^{47,48}.

Deviations from the pentagonal twin structure can cause other etch directions than predicted. Therefore, researchers have investigated both crystal structures and analysed in-situ electron microscopy data of GRR to establish the actual etching of the wire.

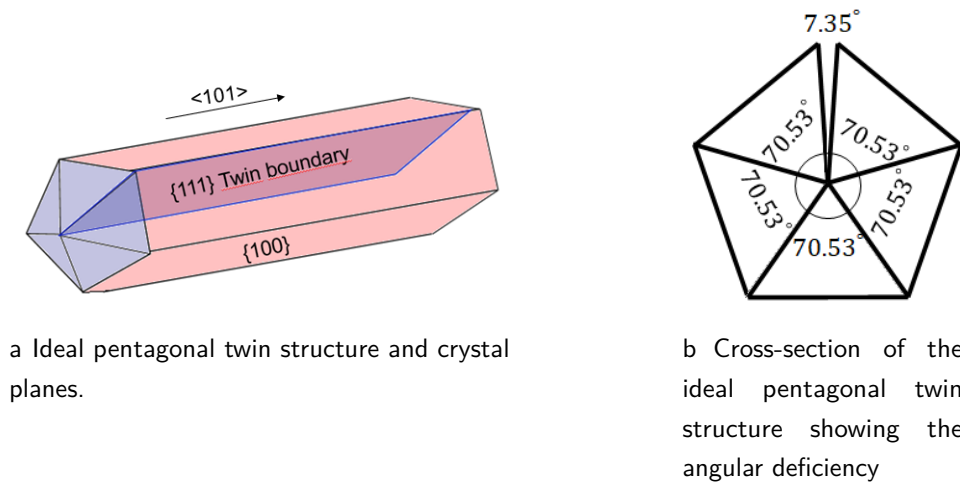


Figure 5.1: Pentagonal twin structure of silver nanowire.

Previously, 3D-electron diffraction has been used to study the strain fields in an Ag nanowire where an internal defect structural model was proposed⁴⁷. Also in-situ studies have revealed non-perfect Ag nanowires. Transmission X-ray microscopy revealed an anisotropic etch⁴⁹ while more recent studies, after the introduction of liquid TEM, suggest a high edge facet selectivity^{50,51}. An in-situ liquid TEM study shows that generally etching is initiated from the side of the wire (one of the $\{100\}$ planes) and progress along the nanowire in the $\langle 101 \rangle$ direction as proposed by theory. Since etching favours facets with high surface energy, etching along the wire is favoured. However, it was also reported

that the etching could happen simultaneously along the five triangular crystalline sections or occasionally along only one of the five triangular crystalline sections. Furthermore, it was observed that the etching could terminate randomly in the wire indicating that defects could both hinder or alter the etching⁵¹.

In this work 3D-OMiTEM is applied on a silver nanowire in order to come a step closer to understand the deviations from the theoretical etch direction. This is done by comparing the theoretical structure to that obtained by 3D-OMiTEM.

5.2 Experimental Methods

Sample preparation

Commercial $\varnothing 45$ nm silver nanowires synthesized by PVP assisted polyol method were mixed with ethanol and directly dropcasted onto a commercial 50 nm silicon nitride support on a 200 μ m silicon frame for TEM. The silicon nitride support had a window size of 0.5x1.5 mm designed for high-tilt tomographic applications enabling imaging with up to 75° tilt.

3D-OMiTEM acquisition

The OMiTEM dataset was acquired using a Jeol2100 TEM-LaB6 and a single tilt holder with a high tilt retainer at 200 keV. A 1k camera was used for fast readout and the magnification was set to x25.000 giving a pixel size of ~ 1 nm. The sample tilt was set to $\pm 60^\circ$ with a 4° sample tilt step to avoid beam damage as described in chapter 4.

To control the beam tilt and objective aperture, the EM-DFOM software by TVIPS⁵² was used. For the DF collection, the 5 inner rings of the diffraction pattern were used with a 2° step (180 images per diffraction ring).

3D-OMiTEM Reconstruction

All images were filtered using a non-local means filter in MATLAB® to remove noise. The search window size was set to 21, the comparison window size to 5 and the degree of smoothing used was the standard deviation of noise estimated from the image. The data was segmented using Dream3D⁵³ with a 5° misorientation tolerance and only grains with a confidence index larger than 0.14 was included. Noise was removed by fitting all segmented grains with an ellipsoid and removing grains having a semiaxis below 4 voxels and finally the data was dilated to fill empty holes.

The grain boundary plane distribution (GBPD) and grain boundary character distribution (GBCD) was calculated using a metric based approach described elsewhere⁵⁴. The GBPD was calculated using 3000 sampling points and a limiting distance of 9° excluding triangles faces directly neighbouring triple lines i.e. only interior facets are included. The GBCD was calculated with 3000 sampling points using a limiting distance of 8° for misorientations, 8° for plane inclinations and excluding triangles faces directly neighbouring triple lines. The GBCD and GBPD were plotted using a Mathematica plotting script developed by Glowinski et al. (2014)⁵⁵. The choice of the limiting distances will be discussed in the results and discussion section.

5.3 Results and Discussion

Pristine silver nanowires were initially inspected in the Transmission Electron Microscope (TEM) to reveal deviations from the ideal structure. This was done in two parts. Firstly, a BF tilt series was recorded, secondly a Dark Field (DF) test was done at 0 tilt.

The BF tilt series on figure 5.2 reveals diffraction contrast inconsistent with the ideal structure shown on figure 5.1. From the ideal structure it would be expected to only see diffraction contrast between the triangular sections i.e. there should be no color difference along the nanowire. However, in figure 5.2(a) a dark feature is visible in the middle of the wire which disappears as the sample is tilted. Because of the shape when tilting the sample, we can conclude that this is not a thickness effect. Furthermore, the contrast in all the images in figure 5.2 is not even. Together these observations indicate that the diffraction contrast stems from a deviation of the ideal crystal structure.

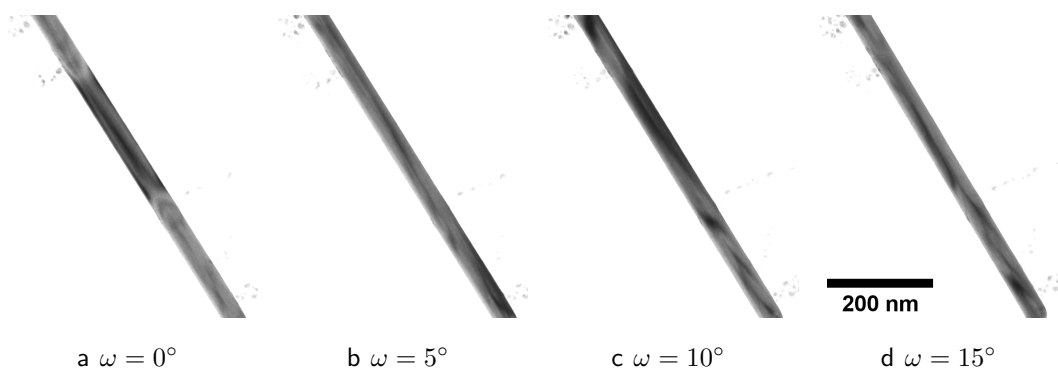


Figure 5.2: BF tilt series of silver nanowire

Deviations from the ideal crystal orientation is further revealed by DF imaging. The DF on figure 5.3(c) shows a strongly diffracting volume where we previously, in the BF image,

saw a dark feature. On each side of the feature there is a small dark volume revealing that the crystal orientation here is different than in the rest of the triangular segment.

The DF series on figure 5.3 shows that defects or deviations from the pentagonal structure are visible with DF and thereby also with 3D-OMiTEM. Thus, further investigation by 3D-OMiTEM would possibly reveal interesting deviations from the pentagonal structure. In DF imaging, as in 3D-OMiTEM, part of the sample lights up when probed. The image has a very low signal in (a) and (b) but in (c) almost half of the wire lights up indicating that it is one of the triangular sections shown in figure 5.1.

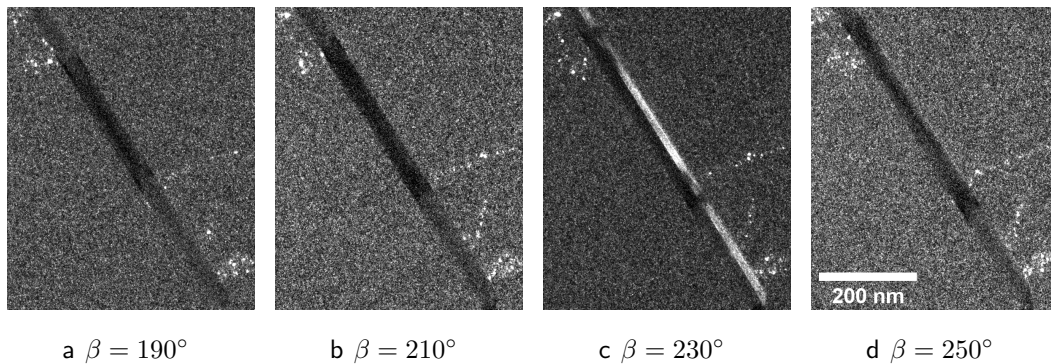


Figure 5.3: DF series of silver nanowire for sample tilt $\omega = 0^\circ$ and ring number $\alpha = 1$

The DF and BF series revealed that the Ag nanowire does not have the perfect structure as shown on figure 5.1. By a quick visual inspection of the sample with multiple nanowires, it is obvious that practically all nanowires have deviations from the perfect structure. An overview image is shown on figure 5.4 containing seven silver nanowires all with uneven contrast indicating deviations from the ideal pentagonal twin structure. This could be the reason why etching happens in different ways in different wires.

By using 3D-OMiTEM these non-perfect structures can be resolved to help improve our understanding of the GRR etching. A silver nanowire with even contrast that had not been exposed to the electron beam was chosen for the 3D-OMiTEM acquisition. A BF image of the nanowire is displayed on figure 5.5.

The corresponding 3D-orientation map is displayed on figure 5.6 and shows the Ag nanowire coloured by crystal orientation in inverse pole figure (IPF) color. Figure 5.6(a) is coloured with x-direction IPF colouring, which is parallel to the electron beam at 0° tilt. (b) is coloured with z-direction IPF colouring, which is perpendicular to the e-beam and parallel to the nanowire.

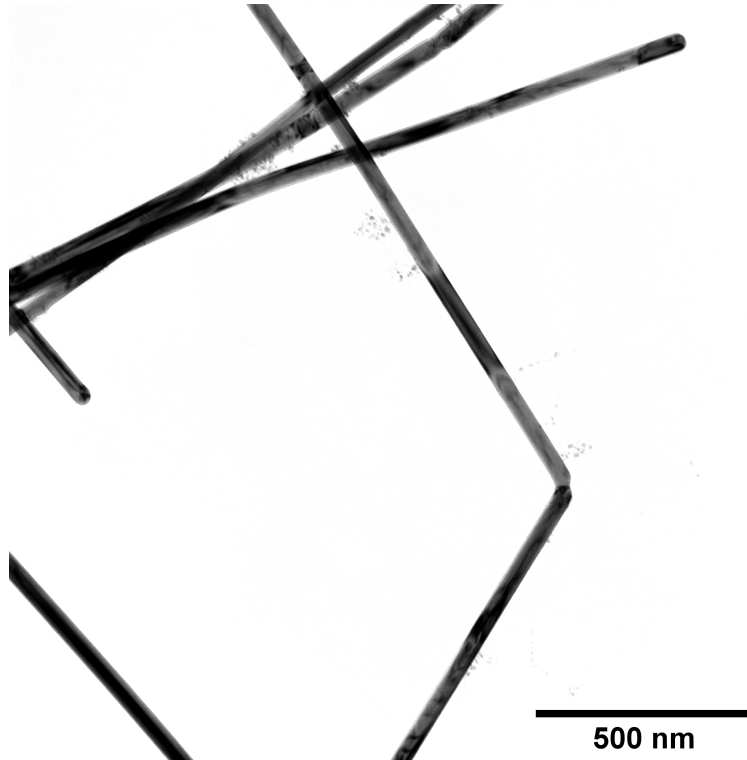


Figure 5.4: Overview image showing seven silver nanowires. All nanowires show sign of uneven contrast indicating deviations from the ideal pentagonal twin structure.

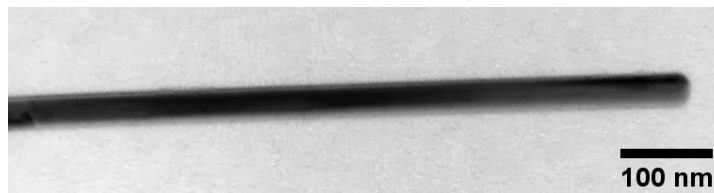


Figure 5.5: BF image of silver nanowire used for 3D-OMiTEM

The first obvious orientation texture seen in figure 5.6 is in (b) where the whole nanowire is green corresponding to $\{101\}$ planes. This means that when looking along the z-direction $[001]$ we only see $\{101\}$ planes confirming the structure in figure 5.1.

The x-direction colouring reveals five different colors corresponding to the five crystal orientations in the triangular segments in figure 5.1. However, the shape of these segments do not correspond to the theoretical structure. Figure 5.6 show the surface of the nanowire from the front and back seen from the beam direction at 0° tilt. If the sample had the ideal structure we would expect that the front and back surface would show two-three different colors with a straight boundary between them. However, even though the surfaces do have the straight boundaries, some segments are gradually

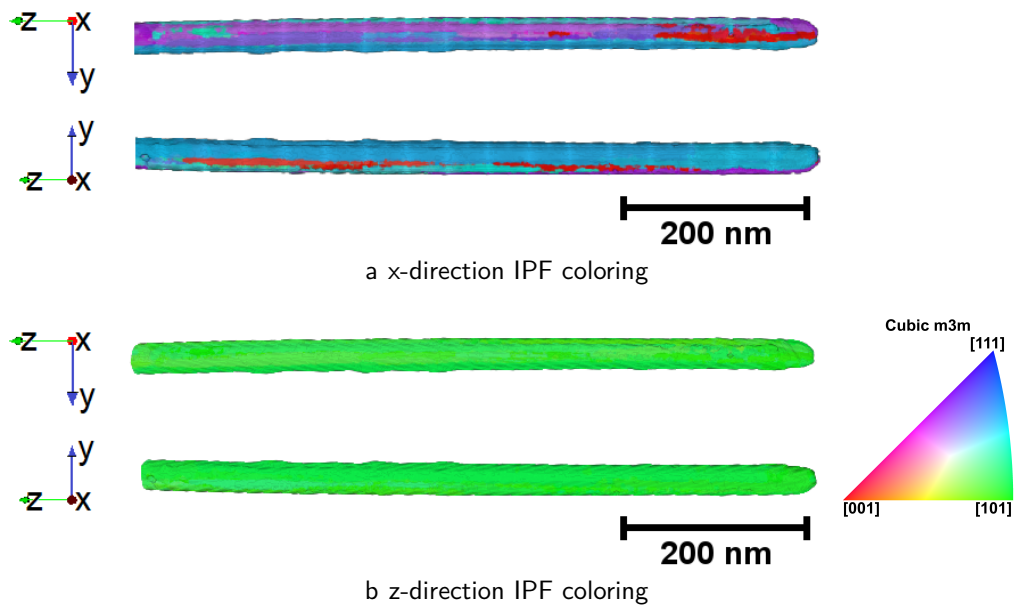


Figure 5.6: 3D orientation maps of silver nanowire. The maps show the surface from two directions, front and back seen from the beam direction at 0° tilt. (a) is the nanowire in x-direction IPF colouring.

replaced by other segments along the wire. This can e.g. be seen on the upper surface in figure 5.6(a) where the dark purple segment disappear and a red segment appears.

To further analyse the structure, the 3D structure is sliced along the x- and z axis. The results are shown on figure 5.7 and 5.8.

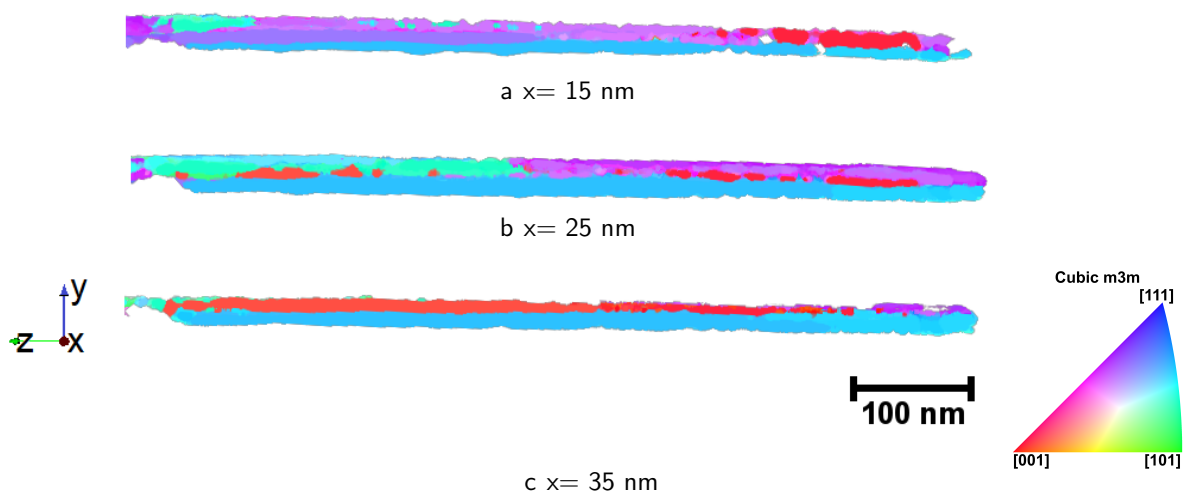


Figure 5.7: YZ-ortho slices through silver nanowire in x-direction IPF-colouring. $x=0$ is set at the surface of the nanowire.

The ortho-slices parallel to the wire reveal the five different crystal segments as expected. The five segments appear in the following order:

- At $x=15$ nm two main crystal orientations (light purple and dark purple) are visible. However, in some areas they are replaced by other crystal orientations (primarily the red and blue).
- At $x=25$ nm a new segment (blue), and parts of a second smaller segment (green), is revealed .
- At $x=35$ nm two main segments are visible (red and blue) and a small green segment.

The ortho slices perpendicular to the nanowire reveal the cross section. The slices on figure 5.8 show that the blue crystal segment is slightly larger than the rest of the orientations. Furthermore it reveals that the green segment is only visible for $z= 400-720$ nm (see figure 5.8). In this region all the crystal segments are evenly distributed and the structure is similar to the ideal shown in figure 5.1.

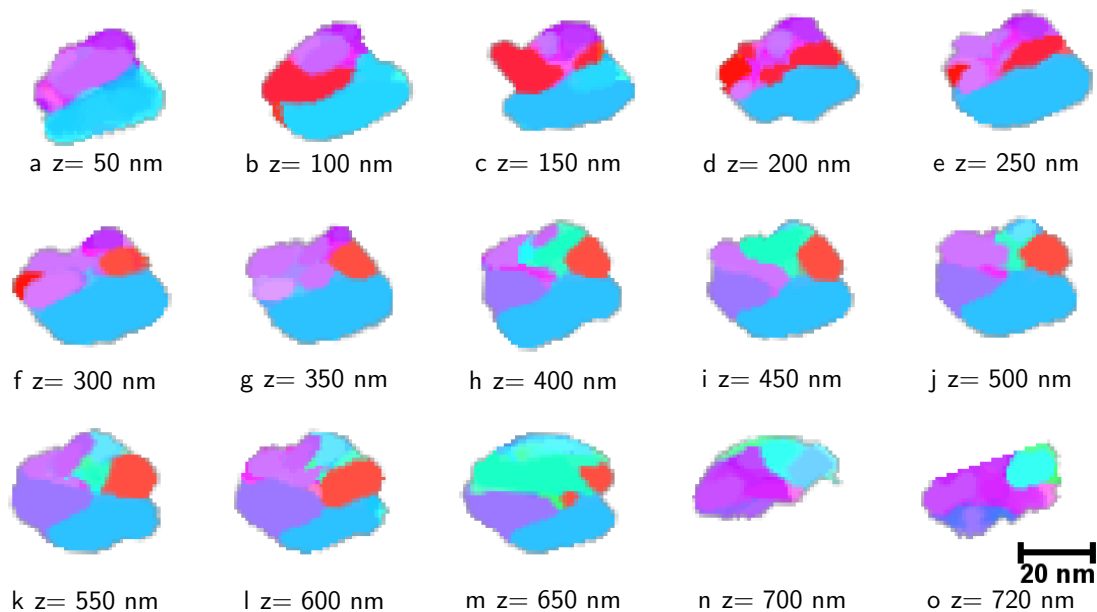


Figure 5.8: XY-Ortho slices through silver nanowire in x-direction IPF coloring

In general the volumes of the crystal segments are not equal and the green and purple segment is only found in a small part of the sample (to the left on figure 5.7). The main segments found in figure 5.8 and 5.7, except the green, have a straight boundary along the whole wire, consistent with the ideal structure. However, in some areas the main crystal segment is replaced by one of the other segments.

Only 30 projections were acquired which have an impact on the internal shape of the segments since the resolution is decreased as described in chapter 4. Furthermore, if particular segments are contained in more projections than others it will result in a higher confidence index which could shadow indexed segments with smaller confidence index³⁷. This could explain why the blue crystal segment is larger than the rest of the segments since this was the crystal segment with highest average confidence index. To avoid these unwanted effects, the orientation map should be recorded at higher angles with a smaller step size. However, as explained in chapter 4 the nanowire suffered from beam damage and therefore the number of projections were reduced. A way to solve this, is to increase the beam tilt angle step size. Since this type of sample only has five main segments, the diffraction pattern would not show a ring pattern but rather individual spots. This could be exploited by only probing these positions in reciprocal space. In this way the number of images, and thereby the total exposure time, would be decreased while maintaining a high number of projections. For further information on acquisition parameters and how they affect the internal structure refer to chapter 4.

The result from both the prior DF series and the 3D-OMiTEM show that the structure does not have the ideal structure as in figure 5.1. Furthermore, the results suggest that defects can change the crystal orientation of a large area not only locally around the defect. This could explain deviations from the expected etch direction.

The discussion and analysis until now has focussed on the morphological shapes of the crystal segments. In the following a crystallographic analysis will be presented. This is done by analysing the misorientations between neighbouring crystal segments and by mapping the Grain Boundary Plane distribution (GBPD) and the Grain Boundary Character Distribution (GBCD).

A segmentation was done by grouping voxels with crystal orientation differing by less than 5° . The segmentation process revealed six crystal segments. The five expected crystal segments and an extra purple segment possibly stemming from a defect. The misorientation between these crystal segments are summarized in table 5.1. The misorientation refers to the minimum rotation angle between two crystal lattices in neighbouring grains. Note that for cubic crystals, the misorientation can not be larger than 62.8° ³³ due to crystal symmetries.

The light blue coloured tabular cells in table 5.1 are the neighbouring crystal segments in an ideal pentagonal structure. These crystal segments have a misorientation of approximately 60° agreeing with the ideal structure. The small deviations from the expected 60° could be the result from averaging of the crystal orientation after segmentation. Artefacts

Crystal Segment	Dark Purple	Purple	Green	Red	Small Purple defect
Blue	58°		34°	54°	37°
Dark Purple		54°	38°	38°	55°
Purple			57°		
Green				58°	60°
Red					35°

Table 5.1: Misorientation between neighbouring crystal segments in silver nanowire. All units are in degrees. Light blue coloured tabular cells show the neighbours in the ideal structure.

due to poorly indexed grains can contribute to the average misorientation however, it could also be the result of defects stemming from the solid angle deficiency previously found^{47,48}.

The pentagonal twin structure showed that the ideal nanowire should have five $\{111\}$ grain boundary planes. The $\{100\}$ sides are surface boundaries and are therefore not included in the GBPD. The GBPD in the nanowire is mapped in figure 5.9 to reveal deviations from the ideal grain boundaries. The GBPD reveals what type of planes are present at the grain boundary and is normalized with a random distribution. Therefore the unit is multiples of random (MRD). Hence a fully random distribution would have a GBPD only containing values of 1 MRD.

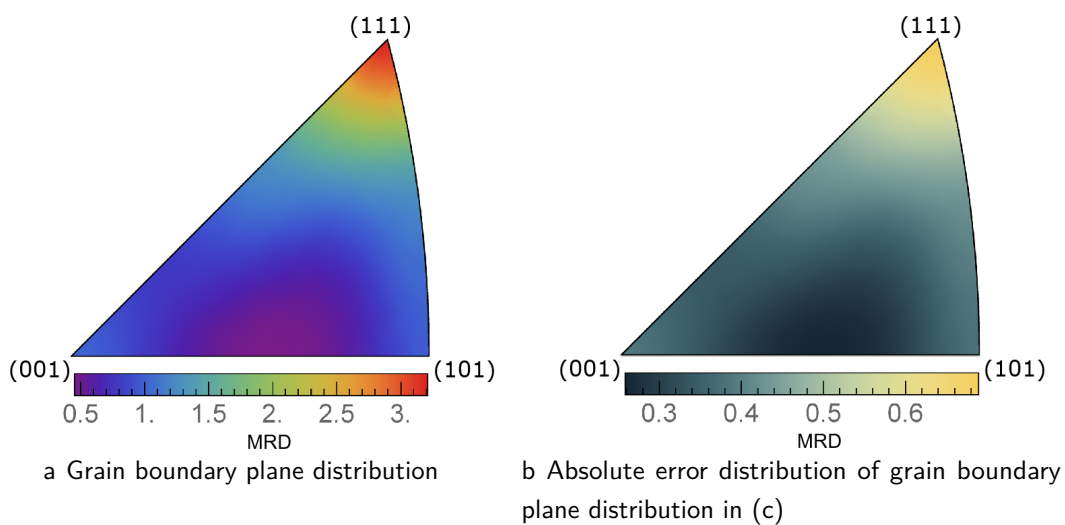


Figure 5.9: Grain boundary plane distribution of silver nanowire

The GBPD in figure 5.9 shows that there is an over representation of $\{111\}$ planes, compared to a random distribution, in good agreement with the ideal pentagonal structure as these should be the only type of GBs in the structure.

The fraction of twin boundaries was calculated by counting how many GBs have a misorientation of 60° around the $[111]$ axis with an axis tolerance of 9° and an angle tolerance of $15\sqrt{3} = 26^\circ$ calculated by Brandon's Criteria⁵⁶. The result was that 65% were twin boundaries. Thus, the remaining grain boundaries are deviations from the ideal structure.

Twinning in fcc metals is defined as a misorientation of 60° around a $\{111\}$ -misorientation axis. In order to determine what grain boundary planes the sample has for this misorientation ($\{111\}/60^\circ$) they are plotted in a stereographic projection. The result is shown on figure 5.10. From this it is possible to determine what type of grain boundaries are dominant in the sample for this misorientation.

Figure 5.10(c) is a diagram showing the positions of different types of characteristic geometric boundaries. By comparing this to the GBCD obtained from the silver nanowire in (a) it is apparent that the sample has twist-, symmetric- and 180-tilt boundaries which is characteristics of a twin boundary. Furthermore, since the most dominant peak is at (111) , most of the grain boundaries are characterized as pure-twist boundaries as the definition of a pure twist boundary is that $\mathbf{u} \cdot \mathbf{m}_1 = 1$, where \mathbf{u} is misorientation axis and \mathbf{m} is the unit vector normal to the grain boundary plane²⁴. However, small peaks at (-211) $(-1-12)$ and $(1-21)$ indicate the presence of a small fraction of mixed tilt and twist grain boundaries.

The presence of twin boundaries is confirmed by the GBCD on figure 5.10 since the signal of the GBCD for twins are within 2 times the error (standard deviation). The GBCD further indicates that a large fraction of the twin boundaries are pure twist boundaries since the peak is very localized around (111) . This is in agreement with the ideal structure.

To determine the angular tolerance, which is the resolution in the boundary plane subspace, the pure-twist twin boundaries were used. The $\{111\}$ peak was fitted with a Gaussian peak to find the standard deviation. The fit is shown on figure 5.11 with the fitting parameters in table 5.2. The fit follows a Gaussian but has a small broadening at the tails. This could be explained by the GBCD not being of the pure twist boundary lines but also has a small presence of 180-tilt boundaries. These can be seen as lines with low intensity in the GBCD in the position as shown with green lines in the diagram on figure 5.10c.

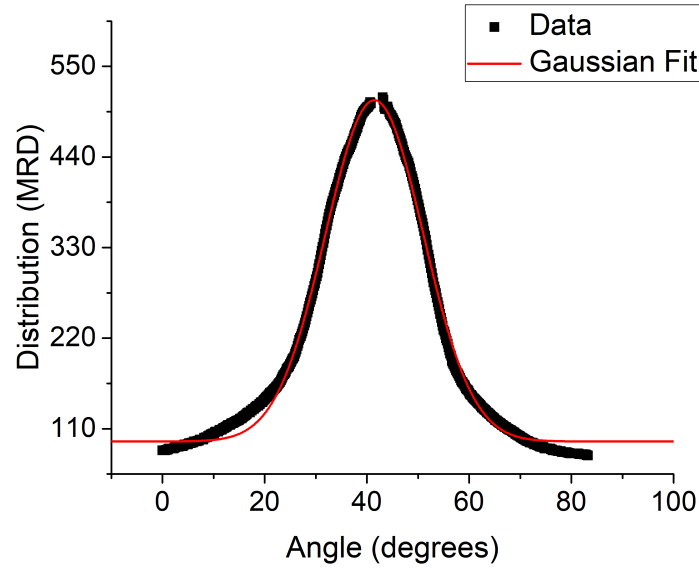


Figure 5.11: Line profile and corresponding gaussian fit of the $\{111\}$ peak in the GBCD on figure 5.10a of fcc twin.

	parameter	value	standard error
$y_0 + \frac{A}{w\sqrt{\pi/2}} \exp\left\{-2\frac{(x-x_c)^2}{w^2}\right\}$	y_0	51.65	2.19
	x_c	17.33	0.03
	w	18.34	0.23
	A	4152.09	94.52
	σ	9.17	0.12
	R^2	0.99369	

Table 5.2: Parameters and goodness of fit of the Gaussian fit in figure 5.11.

tolerance was chosen to be 8° as this was the closest value to the resolution that could be chosen in the software. Judging from the error plot, this tolerance was sufficient for creating a GBCD with minor errors.

5.4 Conclusion

3D-OMiTEM gives the possibilities of analysing structures similar to EBSD but in the TEM increasing the resolution and enabling subsequent TEM based analysis. An example of this was shown by analysing the nanowire with GBPD and GBCD which revealed a disturbed pentagonal twinning structure. 65% of the GBs were twins while the rest

are deviations from the pentagonal twinning structure. These deviations could cause distortions in the otherwise inert $\{111\}$ planes enabling pathways for etching across crystal segments.

This study shows that 3D-OMiTEM is a feasible tool for determining crystal orientation. However, due to the few projections and the missing wedge, the morphology is distorted. This could be corrected by increasing the number of projections. However, due to beam damage, this was not possible by simply decreasing the tilt step size. Instead, a solution could be to probe fewer points in reciprocal space. Since the sample only contain five crystal segments, the diffraction pattern will not be a ring pattern but consist of diffraction spots. By only probing these spots in reciprocal space it will be possible to enable increment of the number of projections without altering the total exposure time and thereby the beam damage.

As a result this example shows that 3D-OMiTEM is a promising tool for determining crystal structures but designing the acquisition prior to data collection is crucial. This can be done with DF and BF tilt series together with an analysis of the diffraction patterns.

Chapter 6

Statistical Morphological Analysis of Maghemite Nanoflower Ensemble using 3D-OMiTEM

6.1 Introduction

Magnetic nanoparticles have a variety of applications. e.g. cleaning contaminated waters, magnetic storage, electronics, magnetic resonance imaging contrast enhancement, drug delivery and hyperthermia treatment of cancer tumors⁵⁷⁻⁶⁰.

Magnetic hyperthermia is a treatment where the magnetic nanoparticles, typically maghemite ($\gamma\text{-Fe}_2\text{O}_3$), are dispersed in or in close proximity of the sick tissue. By applying an AC magnetic field the particles are heated. If the tissue is heated for more than 30 minutes at 42° the tissue dies. With this method it is possible to locally heat the sick tissue without damaging the healthy tissue^{57,61,62}.

Nanoflower shaped maghemite has proven to be a promising material for hyperthermia^{57-59,62,63}. Furthermore, maghemite is abundant and therefore cheap and can be used in bio-medicine as it is non-toxic^{64,65}. The maghemite nanoflower is composed of multiple agglomerated single crystal nanoparticles that together form a flower shape as shown on figure 6.1^{57,62,64}. It has been suggested that the nanoflowers are polycrystalline. The single crystal nanoparticle may in itself be superparamagnetic. However, when multiple single crystals agglomerate to form nanoflowers, magnetic coupling between the crystallite cores results in cooperative behaviour^{57,58,61,63}. The optimal nanoflower size depends on e.g. what excitation frequency is wanted. Thus, by tuning the size it is

possible to tune the particles for different applications^{57,58,62,64}.

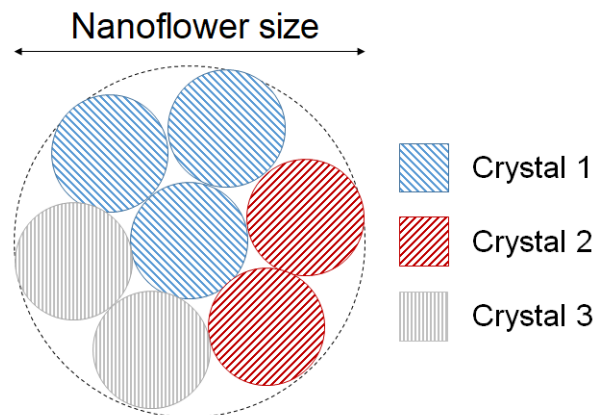


Figure 6.1: Sketch of nanoflower consisting of multiple nanocrystals. The colors indicate crystals with the same crystal orientation. The nanoflower size is the size of the whole agglomerate while the crystallite size is the size of the neighbouring crystals with same crystal orientation.

It is widely accepted that the crystal structure affects the magnetic properties of magnetic materials. Studies have shown that both crystallite size and particle size of the agglomerates affect the overall performance of such nanoflower particles^{57,58,62,64}.

To optimize the heating performance it would therefore be beneficial to study an ensemble of nanoflowers to gain information on their particle morphology, crystallite size and crystal orientations. Previously, this has been studied by a combination of Transmission Electron Microscopy (TEM), High Resolution TEM (HRTEM), Dark Field (DF) imaging, Bright Field (BF)-tomography and X-Ray Diffraction (XRD).

Many studies use a combination of TEM and XRD to compare crystallite size with the nanoflower size^{57,58,63,64}. However, due to the shape of the nanoflowers deviating from spheres it is difficult to extract results from one TEM projection. Therefore, researchers have started to use BF-tomography to calculate a diameter from the whole volume of the nanoflowers instead of only one projection^{58,62}. From these tomograms it has to my knowledge not been possible to study single crystallites so far.

The study of the crystallite sizes and orientations have previously been done using HRTEM^{58,64} and DF imaging^{62,64}. Gavilan et al. (2017) used HRTEM to show that some of their samples had the same crystal orientation throughout the whole nanoflower while others had a more random crystal orientation. However, HRTEM results revealed that the nanoflower seemed to have one shared crystal lattice throughout the whole

nanoflower but DF imaging of another particle in the same ensemble revealed that at most only half of the nanoflower had shared orientation. HRTEM is done at high magnification and as a result only one nanoflower is studied from one projection. Furthermore, in HRTEM the sample is tilted until the atomic columns are clearly visible in one nanoflower. It could be that the HRTEM result was not representative of the whole ensemble. Another explanation could be the HRTEM methodology. Since the nanoflower was tilted until the atomic columns were clear in the whole flower it could be that they chose a projection where this appeared true, but was not representative throughout the depth of the nanoflower. Furthermore, different crystallites can have the same crystal planes when seen from one direction as in the silver nanowire example in chapter 5 where the five different crystal segments had the same crystal plane along the wire. HRTEM is a good way to try to separate crystals with different orientations as the whole flower including atomic columns are visible. In DF imaging only the part of the crystal with a specific orientation will be visible and it is not possible to simultaneously view the shape of the remaining crystallites.

We propose to use 3D-OMiTEM a technique that will be able to show the crystallite sizes and nanoflower sizes in 3D on a whole ensemble of nanoflowers in one measurement. It is thereby possible to achieve similar information as typically gained by HRTEM, DF, BF-tomography and XRD but now in 3D and on a whole ensemble of nanoflowers in one measurement.

In this study 3D-OMiTEM is applied on an ensemble of maghemite nanoflowers to study crystallite size, nanoflower size and crystal orientation. For comparison, HRTEM imaging will be acquired of a nanoflower from the same powder.

6.2 Experimental

Sample preparation

Magnetic nanoparticles of cubic γ -Fe₂O₃s synthesized at DTU Physics (Miriam Varon, Cathrine Frandsen), were mixed with ethanol and directly dropcasted onto a commercial 50 nm silicon nitride support on a 200 μ m silicon frame for TEM. The silicon nitride support had a window size of 0.5x1.5 mm designed for high-tilt tomographic applications enabling imaging with up to 75° tilt.

HRTEM

HRTEM was acquired using a FEI Titan Analytical 80-300ST TEM operated at 300 keV.

3D-OMiTEM collection

The OMiTEM dataset was acquired using a Jeol2100 TEM-LaB6 and a single tilt holder with a high tilt retainer at 200 keV. A 1k camera was used for fast readout and the magnification was set to x25.000 giving a pixel size of ~ 1 nm. The sample tilt was set to ± 60 with a 2° sample tilt step.

To control the beam tilt and objective aperture, the EM-DFOM software by TVIPS⁵² was used. For the DF collection, the 6 inner rings were used with a 2° step (180 images per diffraction ring).

3D-OMiTEM Reconstruction

All images were filtered using a non-local means filter in MATLAB[®] to remove noise. The search window size was set to 21, the comparison window size to 5 and the degree of smoothing used was the standard deviation of noise estimated from the image.

The data was segmented using Dream3D⁵³ with a 2° misorientation tolerance. Finally, noise was removed by fitting all segmented grains with an ellipsoid and removing grains having a semiaxis below 2 voxels and eroding the holes.

The grain boundary plane distribution (GBPD) was calculated using a metric based approach⁵⁴. The GBPD was calculated using 3000 sampling points and a limiting distance of 5° , excluding triangles faces directly neighbouring triple lines (i.e. only the interior faces are included in GBPD) and plotted using a mathematica plotting script⁵⁵.

6.3 Results and Discussion

HRTEM was acquired on a nanoflower to see if the synthesized maghemite in this work has shared lattice planes as previously reported. The result is shown on figure 6.2.

The FFT on figure 6.2b reveals that there is a texture present in the image on figure 6.2a. To colourize the areas with the texture in the FFT, a mask is placed in the FFT only allowing the two inner diffraction spots. By applying an inverse FFT of the masked FFT it is possible to image the areas with texture, colourize the areas and overlay this on the HRTEM image (figure 6.2c). This shows that a large fraction of the nanoflower shares a lattice plane. From figure 6.2c the equivalent diameter of the area with shared crystal planes and an equivalent diameter of the nanoflower was calculated. This was done by creating a circle with the same number of pixels as the area and calculating the diameter. From this, two spheres with these diameters were created and the fraction between the

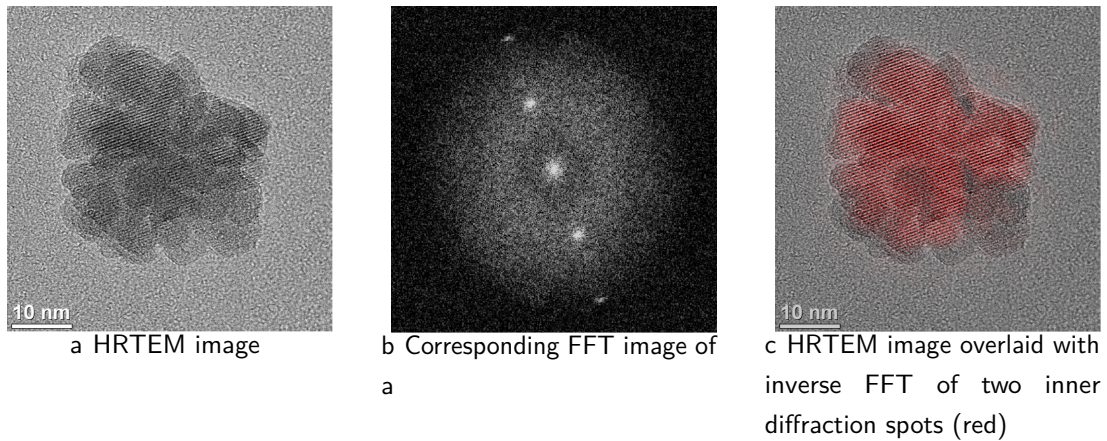


Figure 6.2: HRTEM imaging and corresponding FFT of maghemite nanoflower. The HRTEM (figure a) was acquired by Miriam Varón at DTU physics and printed with premission.

two volumes was calculated. This showed that volume of the largest crystallite, i.e. with the same crystal orientation, was $\sim 68\%$ of the total volume of the nanoflower. The equivalent diameter of the largest crystallite was $\sim 87\%$ of the equivalent diameter of the nanoflower.

3D-OMiTEM was acquired on an ensemble of 62 nanoflowers. An overview image of the sample containing the ensemble of nanoflowers is shown on figure 6.3.

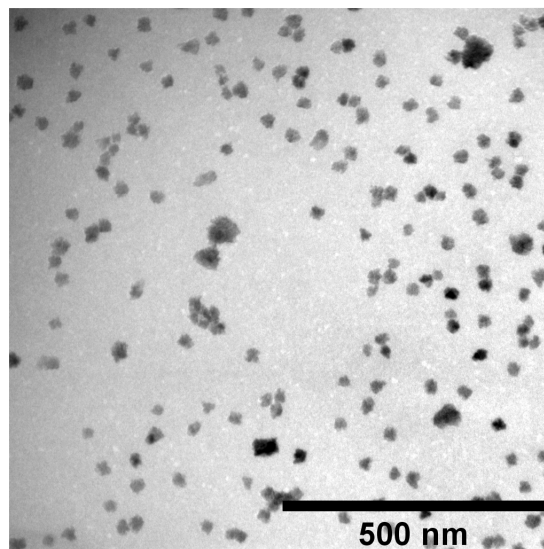


Figure 6.3: BF image showing overview of maghemite nanoflowers.

During the acquisition a set of DF images and a set of BF images were recorded. The result is thus a set of DF images that together form a 3D-Orientation map that

contain information on crystallite size whereas the set of BF images together form a 3D-tomographic reconstruction that contains information on the nanoflower size distribution. Applying 3D-OMiTEM on this type of sample will reveal how both of these informations simultaneously can be used to study if the nanoflower size affects the crystallite size.

The BF image at 0 tilt was cropped in four different regions containing four different nanoflowers and is shown on figure 6.4a, c, e, and g. The corresponding DF images are shown to the right of the BF images, i.e. on figure 6.4b, d, f and h, respectively, and can give an idea of the degree of orientation texture in the different nanoflowers.

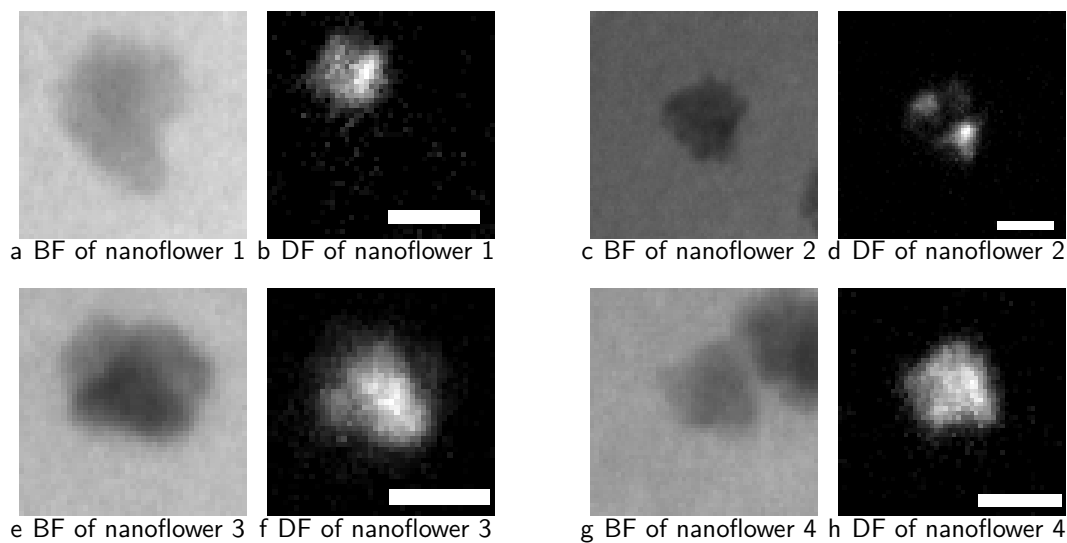


Figure 6.4: BF- and corresponding DF images of four different maghemite nanoflowers. The scale bars are 20 nm

Figure 6.4 shows that nanoflower 1 and 2 do not have one orientation throughout the whole nanoflower as only part of the nanoflower lights up in the DF image. The DF image of nanoflower 3 is brightest in the area where the BF image has the darkest color. This could be because the sample is thicker in this part of the nanoflower and therefore more planes are diffracting. However, it could also be because of difference in orientation and the difference in contrast in the BF image is thereby caused by diffraction contrast. To figure out which of the two explanations is true, the sample should be tilted and investigated further. The BF image of nanoflower 4 also shows part of a different nanoflower adjacent to nanoflower 4. This becomes clear when comparing the BF image with the DF image. The DF image further reveals that in this projection the crystal planes are the same throughout the whole nanoflower which could indicate that the nanoflower only consists of one crystallite.

The four different nanoflowers show a different degree of texture. This indicates that an ensemble can consist of a mixture of nanoflowers with only one crystallite with one crystal orientation and nanoflowers with multiple crystallites with different crystal orientation.

Both crystal orientation and nanoflower size can be studied with 3D-OMiTEM on an entire ensemble as it contains both information. Furthermore, the crystal orientation distribution can be mapped to determine if any texture in the ensemble or single nanoflower exist.

Figure 6.5 show the 3D-OMiTEM results i.e. the 3D reconstructed orientation map masked with the 3D tomographic data. The colors are x-direction Inverse Pole Figure (IPF) colouring. This means that different colors represent different orientations as indicated by the color label.

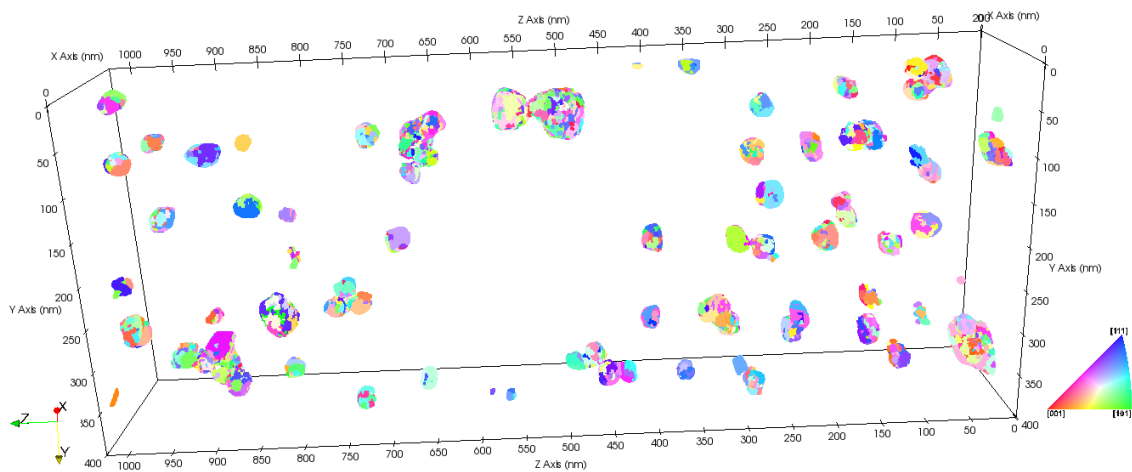


Figure 6.5: 3D-Orientation map of maghemite nanoparticles. Colors are x-direction Inverse Pole Figure (IPF) coloring.

The 3D structure reveals that the ensemble consists of multiple agglomerates consisting of smaller crystallites with different orientation seen as different colors in figure 6.5. The ensemble consist of a few larger agglomerates and many smaller agglomerates. The small agglomerates look like small spheres at this magnification but are in fact the nanoflowers (see figure 6.6a, 6.6b). The larger agglomerates are multiple nanoflowers sticking together as they look like multiple spheres sticking together as in figure 6.6c and 6.6d. Most nanoflowers seem to consist of multiple crystallites as they are multi coloured as in figure 6.6b. However, some of them seem to consist of a few larger crystallites which can be seen as one coloured spheres as in figure 6.6a and left nanoflower in figure 6.6d.

The equivalent diameter was calculated for each nanoflower to compare crystallite- and nanoflower sizes. This was done by computing a sphere with the number of voxels in a

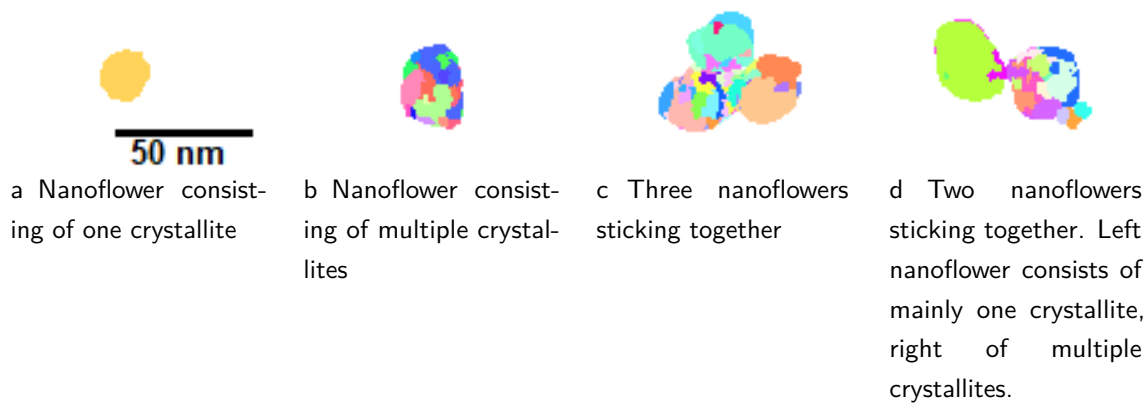


Figure 6.6: Different agglomerates cropped from figure 6.5. Scale bars for all images are as in a.

nanoflower and calculating the diameter. The result revealed that the mean nanoflower size was 26 nm with a standard deviation of 12 nm and that the mean crystallite size was 6 nm with a standard deviation of 2 nm. The distribution of the nanoflower size is shown on figure 6.7a. For 6 nm crystallites the deviations due to the tomographic reconstruction and missing wedge is below the pixel size (1 nm). For the calculation refer to chapter 4. Therefore, the resolution will be limited by the pixel size i.e. ~ 1 nm.

The nanoflowers are composed of 6 nm crystallites with different orientations. However, if a nanoflower consists of one large crystallite and many small crystallites, the mean could be a small value. To determine if this is the case, a histogram of the equivalent diameter of the largest crystallite in each nanoflower was calculated and shown on figure 6.7b. The histogram has a wide spread distribution and reveals that most of the largest crystallites are between 10-25 nm i.e. significantly larger than the mean crystallite size.

To study how the nanoflower size affects the ability for small single crystals to merge and form larger crystallites, the crystallite mean size and max size in a nanoflower is plotted as a function of nanoflower size. The result is shown on figure 6.8a and reveal that the mean crystallite size does not show any evidence of changing with changing nanoflower size. However the plot also reveals that as the nanoflower grows so does the size of the largest crystallite. This suggests that as the nanoflower size becomes larger, more crystallites are agglomerated and the probability for multiple crystallites to merge to form one larger crystallite becomes higher. This result is possible only with 3D-OMiTEM as it contain information of both crystallite size and nanoflower size. Other methods as e.g. XRD only measures the average crystallite size on a whole macroscopic sample and HRTEM becomes time consuming if a whole ensemble of particles (50+) has to be

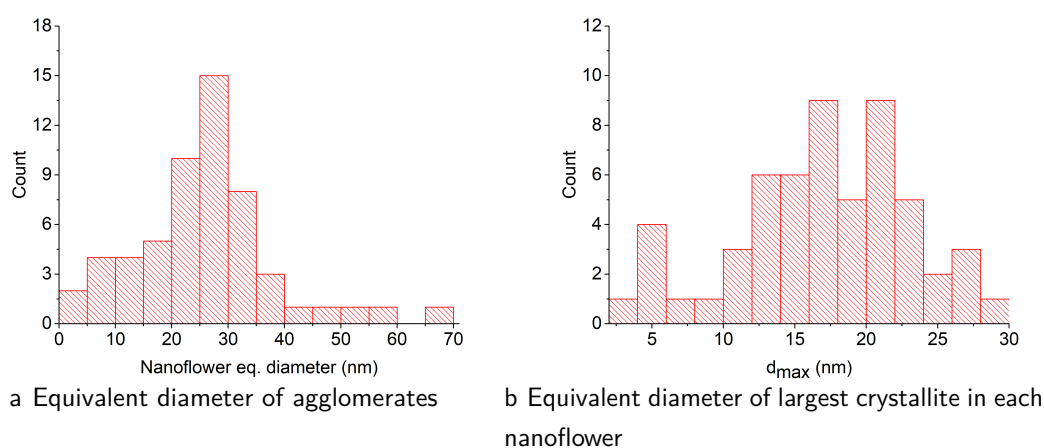


Figure 6.7: Histograms of morphological parameters in maghemite nanoparticles

examined. With 3D-OMiTEM all information is gathered in one acquisition.

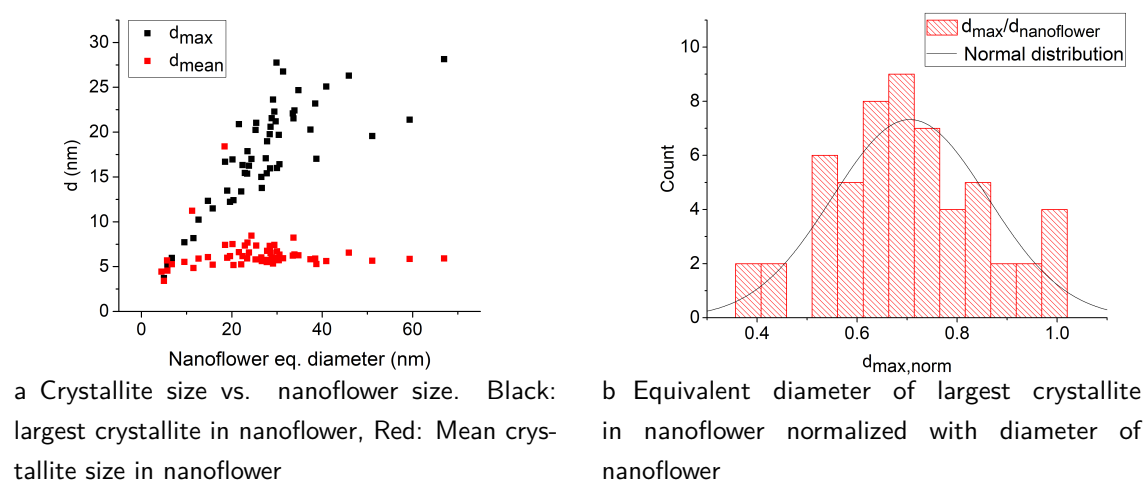


Figure 6.8: Link between crystallite size and nanoflower size of maghemite nanoflowers. (a) is the crystallite size as a function of nanoflower size. (b) b show a histogram of the crystallite size.

The histogram of figure 6.8b is of the crystallite diameter normalized to the nanoflower diameter. This reveals that the largest crystallite size in a nanoflower resembles a normal distribution with a mean of 0.7 and a standard deviation of 0.2. Thus, the largest crystallites typically have a diameter of 70% of the total nanoflower diameter. This could be one of the explanations why HRTEM results show a shared crystal orientation throughout most of the nanoflower. For the HRTEM projection we saw that the largest crystallite diameter was 87% of the total nanoflower diameter which is significantly larger

than the 3D-OMiTEM results. However, the HRTEM was only done on one particle while the 3D-OMiTEM is applied on an ensemble of particles. This could explain the deviation.

The last analysis of the morphology is to look at the position of the largest crystallite in the nanoflowers. To do this the distance between the centroid of the nanoflower and the largest crystallite is calculated and plotted in figure 6.9. The histogram on figure 6.9 has a wide distribution spread and showed no evidence of where the crystal agglomeration is favoured.

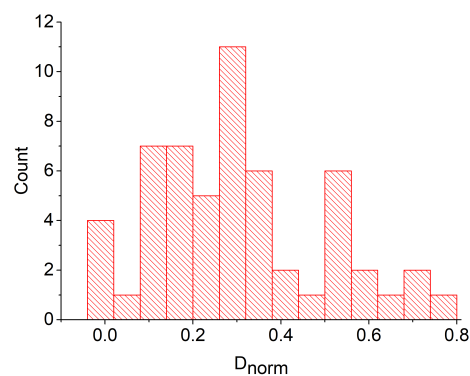


Figure 6.9: Distance between largest crystallite and centroid of maghemite nanoflower normalized to the nanoflower diameter normalized to the nanoflower diameter..

Apart from morphological information 3D-orientation map, acquired by 3D-OMiTEM, also contain information on the crystal orientation. The Grain Boundary Plane Distribution (GBPD) is a tool to show if there is any particular texture in the sample. The GBPD show the crystal plane distribution normalized to that of a random isotropic distribution. Therefore, the unit is multiples of random. If the value is close to 1 it means that the crystal orientation distribution is random. The GBPD shown on figure 6.10 has a maximum value of 1.07 and the error plot distribution shows that the error in this region is approximately 0.02. This means that there are 7% more (101) planes in the ensemble compared to a random structure and fewer (111) planes.

6.4 Conclusion

In this chapter 3D-OMiTEM was applied on an ensemble of maghemite nanoflowers. The example serves to show how statistics on crystallite size and nanoflower size can be extracted from a 3D-OMiTEM data set.

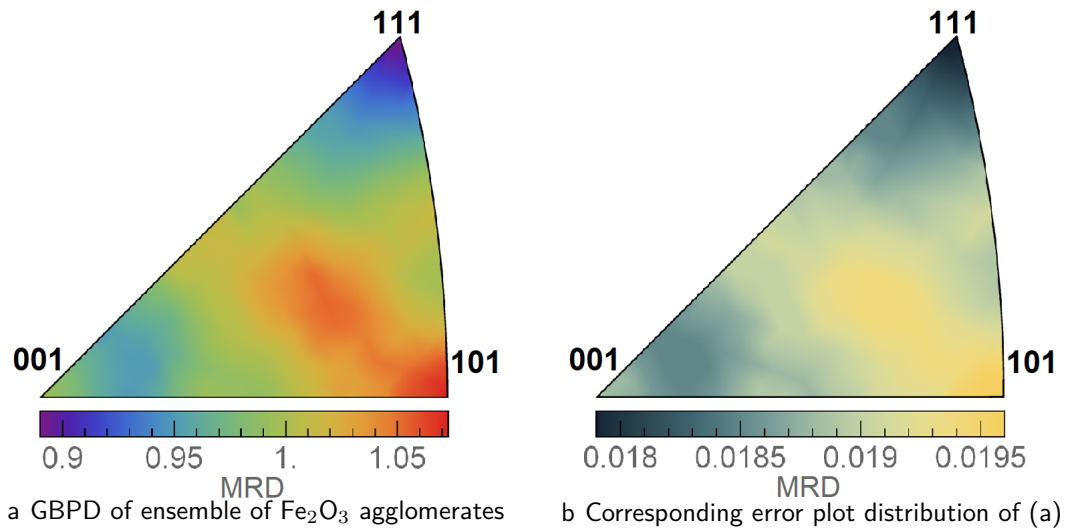


Figure 6.10: Left: GBPD of an ensemble of maghemite nanoflowers. Right: Corresponding error distribution i.e. the standard deviation.

The orientation map had a close to random distribution and supported the theory that nanoflowers are polycrystals composed of small crystallites.

The morphological analysis showed an average crystallite size of approximately 6 nm with a nanoflower size of approximately 26 nm. The mean size of the crystallite size in each nanoflower did not change as the nanoflower size changed. However, the largest crystallite in a nanoflower proved to increase with increasing nanoflower size. With the 3D structure generated by 3D-OMiTEM, simulations on magnetic response should be possible to calculate. OMiTEM can thereby be used as input for simulations in future work.

Chapter 7

Determination of 3D Ion Percolation Path in CGO Nanofibers for Solid Oxide Fuel Cells

This section is based on a manuscript in appendix C "*3D Ion Percolation Path in Gadolinium Doped Ceria Nanofibres for Solid Oxide Electrochemical Cells*". The manuscript in the appendix is the submitted version.

7.1 Abstract

Understanding transport properties in ion conductive solids is key to supporting the development of devices for energy conversion, e.g. solid oxide electrochemical cells. Because of the complex nanostructured nature of such materials they have numerous types of grain boundaries and the prediction of the percolation path becomes challenging. We employ, for the first time, a combination of 3D-Orientation Mapping in the Transmission Electron Microscope and Energy Filtered Transmission Electron Microscopy to map crystal orientation and doping concentration with nm-precision to predict 3D-ion percolation paths in state-of-the-art electrospun ($\text{Ce}_{0.9}\text{Gd}_{0.1}\text{O}_{1.95}$) nanofibres. As expected the structure comprised of hundreds of grains with random isotropic crystal orientation distribution. The results show that the conductivity of CGO nanofibres are affected by grain- and diameter size. Furthermore, we show that 3D-OMiTEM is a powerful non-destructive tool for determining 3D-ion percolation paths with nm-precision of complex nanostructures.

7.2 Introduction

An increasing interest in the use of renewable energy sources emphasizes the need for high performance energy conversion devices. Examples of such devices include, but are not restricted to, Solid Oxide Electrolysis Cells (SOECs) and Fuel Cells (SOFCs). These give an opportunity to exploit fluctuating energy sources. Electrical energy can be harvested by using SOECs during overproduction periods from solar- or wind energy, and utilized in underproduction periods by SOFCs⁶.

Solid Oxide Cells (SOC) are composed of electronic-, ionic- and mixed conductors and high conductivity is an important property for optimal performance. To develop and optimize such devices it is critical to understand the charge transport properties in ion conductive solids^{9,11}.

The ionic and electronic conductivity of functional materials, used in SOCs, are closely related to the nano- and micro-granular structure since they contain a large fraction of grain boundaries (GB)⁹⁻¹⁶. It is widely accepted that the conductivity in the interior of the grains are orders of magnitude larger than at the GB and as a result, the GBs often become the limiting factor for obtaining a higher conductivity^{10,12-16}. The conductivity in the GB is determined by equation 7.1^{9,10}.

$$\sigma_{GB} = \beta_{GB} \frac{n_v^{GB}}{T} \exp\left(\frac{-E^{GB}}{kT}\right), \quad (7.1)$$

where σ_{GB} is the grain boundary conductivity, β_{GB} is the pre-exponential conductivity, which is independent of the doping-concentration, n_v^{GB} is the effective GB carrier concentration i.e. the average concentration of oxygen vacancies in a GB, k is the Boltzmann factor, T is the temperature and E^{GB} is the GB activation energy.

The pre-exponential factor has been widely studied⁶⁶⁻⁷³. However, the activation energy is difficult to determine as it depends on the composition of the individual grain boundary. The complex nano-structured nature of the materials generate a variety of possible GB-types with different atomic structure and composition. This makes it challenging to fully understand the fundamentals and parameters affecting the overall performance.

A recent study by Bowman et al. (2020)⁹ has gathered literature⁶⁷⁻⁷³ on the field to determine the activation energy as a function of grain boundary doping concentration for gadolinium doped ceria (CGO). By fitting the data empirically they determined the relationship in equation 7.2⁹,

$$E^{GB} = 2 \cdot 10^{-4} \left([A^{3+}]_{GB}\right)^{-5} + 0.91 \quad (7.2)$$

where $[A^{3+}]_{GB}$ is the trivalent doping concentration.

The study by Bowman et al. (2020)⁹ furthermore suggests a linear relationship between the crystalline misorientation angle of two neighbouring grains and the GB doping concentration⁹. This gives the opportunity to determine the local GB doping concentration, and thereby the GB- activation energy and conductivity, directly from a crystal orientation map. Hence, a crystal orientation map will be able to predict possible ion percolation paths, which could help determine the overall conductivity of the sample.

The overall conductivity can be affected by cracks or other structural changes⁷⁴. Therefore, the 3D-ion percolation path would be a valuable contribution to understanding the fundamentals of ion conductive solids. Hence, in order to better understand the conductivity of materials for SOCs, it is essential to study their nanoscale crystal orientation on grain level in 3D.

The crystal orientation of grains in SOFCs have previously been studied by Electron Backscatter Diffraction (EBSD)¹⁷⁻¹⁹ and precession electron microscopy (PED)⁹.

EBSD can map out thousands of grain boundaries with good statistical results. Furthermore, it can be conducted in 3D by slicing the sample with a focussed ion beam. However, this technique is highly destructive. Besides, EBSD is a Scanning Electron Microscopy (SEM) technique and as a consequence the resolution is 1-2 orders of magnitude larger than the grain boundary. Therefore, it is not possible to do a simultaneous spectroscopic analysis to correlate chemical composition with the orientation of the individual grain boundaries, simply because the resolution is too low.

PED, on the other hand, is a Scanning Transmission Electron Microscopy (STEM) based technique and has a sub nm-resolution which enables subsequent spectroscopic analysis in the TEM³⁰. However, overlapping grains can disturb the orientation determination and as a consequence, PED is normally only conducted on one slice of material. PED is therefore useful for crystal orientation determination where a subsequent compositional analysis is wanted but the good statistics from the EBSD is lost.

It would be highly beneficial to be able to combine the two techniques to conduct the orientation mapping in a non-destructive way with nm resolution in 3D. This would contribute to the fundamental understanding of the relationship between crystal orientation and the percolation of ions through the material.

This calls for a new way of measuring crystal orientation in the TEM. In this work 3D-Orientation Mapping in the Transmission Electron Microscopy (3D-OMiTEM) a promising technique for non-destructive visualization in 3D is used. Liu et al. first

described the method applied on a simulated data set and on an aluminium thin foil in 2011²⁰. More recently Wu et al. (2020) has described the method applied on a gold nano-island film²¹.

We demonstrate that with this technique it is possible to obtain 3D orientation information of arbitrarily oriented crystals with complex structure and composition using TEM. Although it is still a challenge it is shown that maps can be obtained and reconstructed in a few days making this a feasible tool for electron microscopists.

We employ a combination of Energy Filtered Transmission Electron Microscopy (EFTEM) and OMiTEM to find the linear relationship between the doping concentration and the crystal orientation. The first demonstration is presented of how a 3D-Orientation map, generated by 3D-OMiTEM, in combination with the linear relationship can be used to calculate ion percolation paths with lowest resistivity. This work will contribute to the understanding of how the numerous possible GB-types, with different atomic structure and composition, affect the overall conductivity in the material.

We employ 3D-OMiTEM on a functional material, namely the state of the art SOC material electro-spun Gadolinium doped Cerium Oxide (CGO) nano fibres. These electrospun nanofibres have recently shown potential to be an efficient and cost effective alternative for materials for SOCs. The fibres can form electrodes with high porosity, high pore connectivity and form continuous electron- and ion conducting paths⁷⁵⁻⁸⁰.

We show the first demonstration of the possibilities of 3D-OMiTEM on complex nano structured oxide electrospun fibres. This includes the first 3D-orientation map on nm-scale of an electrospun nano fibre, as well as the analysis of this map, in order to predict and visualize the first ion percolation path in 3D on nm scale. With this powerful tool we thereby come a step closer to understanding and describing the fundamentals of grain boundaries and grain boundary planes in state-of the art electrode materials for SOCs.

To prove the feasibility of 3D-OMiTEM, the results of two different samples are presented and to further evaluate the technique, the obtained mean grain size is compared to the crystallite size obtained from X-Ray Diffraction (XRD).

7.3 Experimental Methods

Sample

The CGO ($\text{Ce}_{0.9}\text{Gd}_{0.1}\text{O}_{1.95}$) nano fibres were prepared by electro-spinning and subsequently calcined. Electro-spun nano-fibres were calcined at 800°C for 1 and 10 hours in atmospheric air. Then ethanol was added to the fibres and the solution was sonicated for

10-20 seconds. Finally, the CGO fibres were dropcasted directly onto a commercial 50 nm silicon nitride membrane with a 0.5x1.5 mm window for TEM.

Electrospinning:

$\text{Gd}(\text{NO}_3)_3 \cdot 6\text{H}_2\text{O}$ (Sigma-Aldrich, 99.9%) and $\text{Ce}(\text{NO}_3)_3 \cdot 6\text{H}_2\text{O}$ (Sigma-Aldrich, 99.999%) were dissolved in deionized H_2O at a molar ratio of 9:1 in order to synthesis CGO ($\text{Ce}_{0.9}\text{Gd}_{0.1}\text{O}_{1.95}$). Polyvinylpyrrolidone (PVP) with an average molecular weight of 1,300,000 was used as a carrier polymer in this experiment. The desired amount of PVP powder was added to the above solution. In the electrospinning solution, the PVP concentration is 10 wt%, and the total concentration of nitrate salts is 25 wt%. This results in a mass ratio of PVP to nitrate salts of 0.4 in the as-spun nanofibres. The resultant electrospinning solution was then loaded into a 10 ml syringe, where a 21 gauge stainless steel needle was attached to the tip of the syringe. The syringe was then mounted on a syringe pump. During electrospinning, the electrospinning solution was pumped out of the needle at an injection rate of 0.3 ml/h with an electrical field of 40 kV. A grounded rotating drum covered by aluminium (Al) foil was used as the collector to collect the electrospun nanofibres. The distance between the tip of the needle and the collector was set as 8 cm. The temperature and relative humidity of the electrospinning chamber was 30°C and 24 RH%, respectively.

3D-OMiTEM collection

Two OMiTEM datasets were acquired. One with the sample calcined for 1 hour and one for the sample calcined for 10 hours.

The OMiTEM datasets were acquired using a Jeol2100 TEM-LaB6 and a single-tilt holder with a high tilt retainer. The magnification was set to x25,000 and a 1k camera was used for fast acquisition giving a pixel size of $\sim 1\text{nm}$. The sample tilt was set to $\pm 72^\circ$ for CGO calcined for 1 hour and $[-72:70]$ for CGO calcined for 10 hours. For both acquisitions a 2° sample tilt step size was used.

To control the beam tilt and objective aperture the TVIPS software, DFOM⁵², was used. For the DF collection, the 5 inner rings were used with a 2° step (180 images per diffraction ring).

3D-OMiTEM Reconstruction

Alignment is necessary for correlating the individual grains containing orientation informa-

tion, from the DF images, to their positions in the overall fibre structure. However, since different parts of the sample light up as they are probed during the acquisition it is not possible to see how the whole fibre drifts during the DF acquisition. Instead, to assess the drift, BF images are recorded after every 10th DF image. Using a linear interpolation, the drift correction is applied to all the recorded DF images for alignment prior to the reconstruction.

All images were filtered using a non-local means filter in MATLAB® to remove noise. Here the standard deviation of noise estimated from the image was used as the degree of smoothing.

The data was segmented using Dream3D⁵³ with a 5° misorientation tolerance and only grains with a confidence index larger than 0.2 was included. Finally noise was removed by fitting all segmented grains with an ellipsoid and removing grains having a semiaxis below 4 voxels for CGO calcined for 1 hour and 5 voxels for CGO calcined for 10 hours.

The grain boundary plane distribution was calculated using a metric based approach⁸¹ with 3000 sampling points and a limiting distance of 5° and plotted using a Mathematica plotting script⁵⁵.

7.4 3D-OMiTEM

During the 3D-OMiTEM acquisition we choose a specific Bragg reflection and form a dark field (DF) image where the contrast in the projection only comes from the part of the sample that obey the specific diffraction condition (7.1b). The DF image is recorded by inserting an objective aperture in the diffraction plane. Depending on what diffraction spot is chosen only grains with this specific orientation will contribute to the contrast in the image. Each image thus constitutes a 2D-projection of the 3D grain shapes observed for a point in the reciprocal space. This is done for beam tilts along the selected ring, 360° with a 2° step. Each of the 5 inner rings in the diffraction pattern was used for every sample rotation angle. For aligning the direct space information bright field (BF) images are recorded by setting the beam tilt to 0 (direct beam) as shown on figure 7.1a. The result is ~70.000 images that are reconstructed into a 3D grain orientation map.

7.5 Results and Analysis

3D-OMiTEM was applied on CGO electrospun nano fibres calcined at 800°C for 1 hour and for 10 hours, respectively, in atmospheric air.

Figure 7.1a shows a BF image of an electrospun CGO nano fibre with a diameter of approximately 200 nm. The BF image shows that the fibre morphology is dense and consists of multiple grains. However, the individual grains are difficult to distinguish which makes it hard to estimate a grain size distribution.

Individual grains can be identified on the corresponding DF image in figure 7.1b. By browsing through the DF images, recorded by choosing different diffraction spots, different grains light up. This reveals that the fibre is a polycrystalline sample with multiple grains with different crystal orientations.

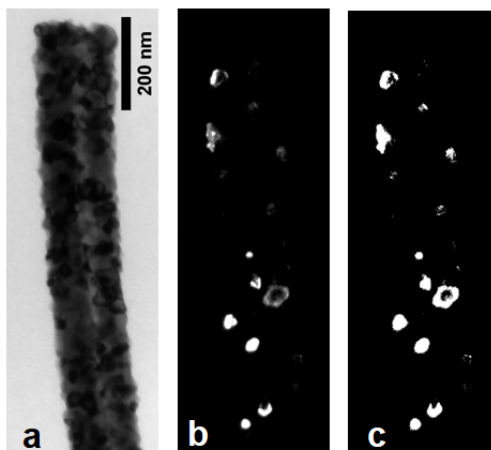


Figure 7.1: TEM images of CGO fibre calcined at 800°C for 1 hour. a) Bright field image, b) one of hundreds of thousands of DF images used for reconstruction. c) binarized image of b) used for reconstruction. All images are scaled to have the same size with scale bar as shown in a).

The DF images are used to determine the crystal orientations as their acquisition parameters carry the corresponding reciprocal space information. The orientation reconstruction is done on threshold aligned DF images. An example is shown on figure 7.1c.

Using in-house developed software, grains are reconstructed resulting in a multi-dimensional data set with x,y,z coordinates each with a confidence index and crystal orientation. The results is shown on figure 7.2.

Since BF images contain more accurate information about the overall morphology of the fibres, BF tomograms were reconstructed in Inspect3D⁸² and used to mask the outer

boundary of the fibres in the final orientation map.

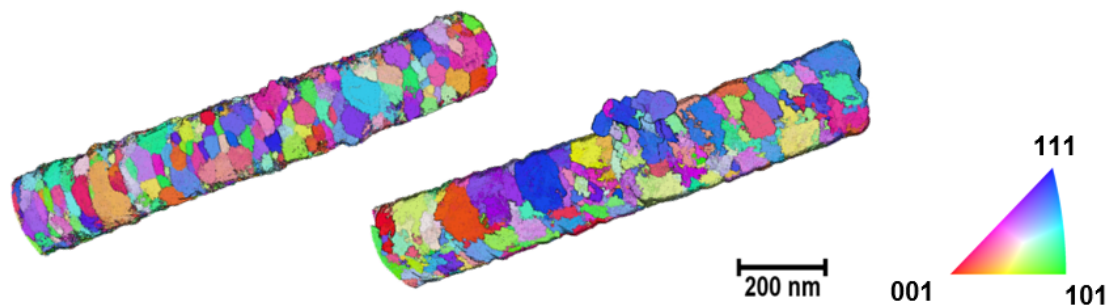


Figure 7.2: Orientation map of an electrospun CGO fibre calcined at 800°C: Left calcined for 1 hours, right calcined for 10 hours. The colors are x-direction inverse pole figure (IPF) coloring showing crystal directions.

The orientation maps produced by 3D-OMiTEM are presented in figure 7.2 and show the electrospun fibres in 3D with grains coloured by their crystal orientation in inverse pole figure (IPF) color. The individual grains are defined as well as the overall morphological structure of the fibre. This enables extraction of geometric and orientation parameters of all individual grains for statistical analysis as well as for orientation analysis. This is the first time this type of 3D analysis has been conducted on electrospun nano fibres.

The 3D orientation map enables analysis and characterization of both the grains or grain boundaries. To characterize the grains, the 3D structure is segmented by grouping voxels with a misorientation smaller than a set tolerance and defining them as one grain.

Each grain is compared to its neighbour and a histogram of the misorientation between neighbouring grains is plotted. The misorientation distribution on figure 7.3b and 7.3d showed no texture in the two fibres. Since it follows the Mackenzie distribution for randomly oriented cubic crystals (solid line in figure 7.3).

This finding is supported by the analysis of the grain boundary plane distribution (GBPD).

The GBPDs of the two electro-spun fibres shown on figure 7.4 are mapped using a metric based approach explained in⁵⁴, plotted using a mathematica script described in⁵⁵ and calculated using Dream3D⁵³. The GBPD of the two electro-spun fibres shown on figure 7.4 describes the measured area of grain boundary planes normalized with respect to a random isotropic distribution⁵⁵. The unit is thus multiples of random distribution. The maxima in the GBPD is 1.03 for CGO calcined for 1 hour (figure 7.4a) and 1.04 (figure 7.4c) for CGO calcined for 10 hours and lies within the statistical error of uncertainty

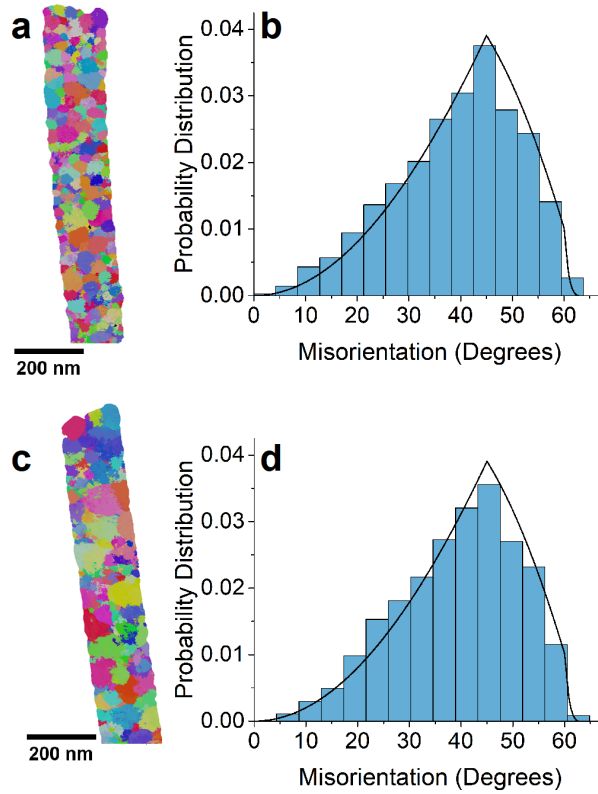


Figure 7.3: a, c shows an ortho slice through the middle of the sample in ipf colors as figure 7.2. b and d is the misorientation probability distribution. The solid line is the theoretical Mackenzie distribution for randomly oriented crystals. a and b are the results from CGO calcined at 800°C for 1 hour, c and d for CGO calcined at 800°C for 10 hours.

(figure 7.4b, 7.4d). Therefore, the grain boundary plane distribution shows a random isotropic distribution for both samples and the two samples are indistinguishable with regards to the crystal orientation.

Both orientation analyses thereby show that grains in both fibres have a random isotropic distribution.

7.5.1 Evaluation of Method

To test how well the 3D-OMiTEM technique actually resolves the structure, the grain size found from 3D-OMiTEM is compared to the crystallite size from XRD data from the powder with the fibres.

The grain size distribution was calculated from the 3D orientation map. From the number

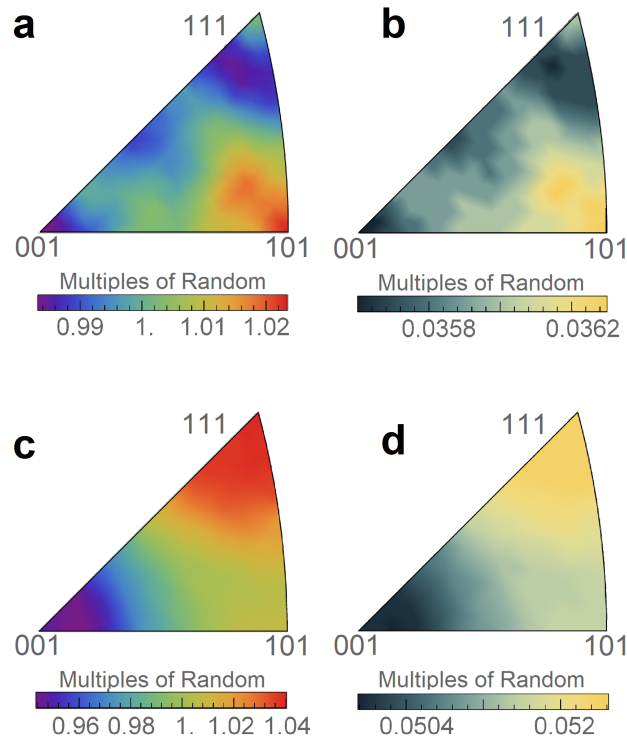


Figure 7.4: a, c show the grain boundary plane distribution (GBPD) with multiples of random scale. b, d is the error distribution of the GBPD in a and c, respectively, in absolute values.

of voxels in a grain, a corresponding sphere was computed and the equivalent diameter was calculated for each grain. The grain size distribution for the two fibres are shown on figure 7.5 as a histogram of the equivalent diameter with a log normal fit.

The grain size distributions on figure 7.5 follows a log normal distribution with no significant noise peaks and reveals, as oppose to the orientation analysis, a difference in the two fibres. From the fits, the equivalent mean diameters can be found. The sample calcined for 1 hour has a mean diameter of 29.89 ± 0.9 nm and after 10 hours it increased to 35.26 ± 1.6 nm i.e. a 18% increase. XRD results shown on figure 7.6 supports these grain sizes.

The XRD data shown on figure 7.6 were collected for CGO electro-spun fibre powder calcined for 1 hour and for 10 hours before drop casting to the TEM grid. The data were analysed and contain the expected peaks from CGO with no additional crystal phases. Assuming lognormal distribution, as confirmed by the grain size distribution in figure 7.5, the mean diameter was calculated to be: 27.8 ± 0.8 nm for CGO calcined at 800°C after 1 hour, which increased to 38 ± 0.3 nm after 10 hours.

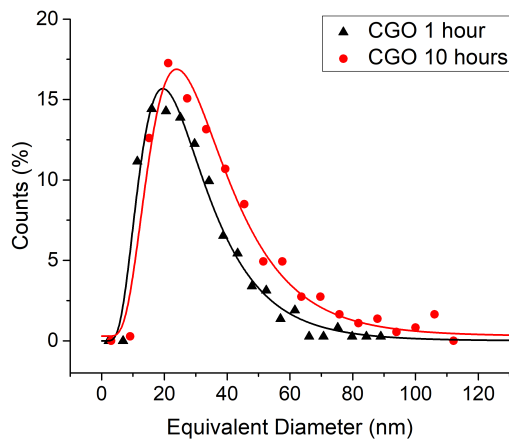


Figure 7.5: Grain size distribution. Black is the size distribution of CGO calcined at 800°C for 1 hour in atmospheric air. Red is the result for the sample calcined for 10 hour in atmospheric air. The solid lines show lognormal distribution fits.

When comparing the crystallite size from the XRD results with the equivalent diameter found from 3D-OMiTEM it is worth noting that the two results are in close agreement. The sample calcined for 1 hour has a mean diameter which is 2 nm larger than the crystallite size and for the sample calcined for 10 hours the diameter was 2 nm smaller than the crystallite size. This suggests that 3D-OMiTEM can be used to not only find the particle size but also the crystallite size. My best explanation of these small deviations is a mix of unfiltered noise and missing wedge effect.

The fibre calcined for 10 hours was thicker than the fibre calcined for 1 hour. As a consequence the signal from the inner part of the sample was weaker resulting in more noise in the reconstruction. This noise will contribute to the calculation as small segmented grains. This could be the cause of the slightly smaller mean equivalent diameter compared to the XRD result.

The sample calcined for 1 hour had a slightly larger equivalent diameter compared to the XRD result. This could be explained by the missing wedge effect stemming from missing high angle projections due to the TEM holder restrictions and the grid shading over the sample.

To examine the missing wedge all grains were fitted with an ellipsoid and the semi-axis were compared. The semi-axis perpendicular to the beam and parallel to the fibre should not show any elongation which was also what was observed on the reconstructed structure. However, an elongation was observed in one of the other axis due to the missing wedge.

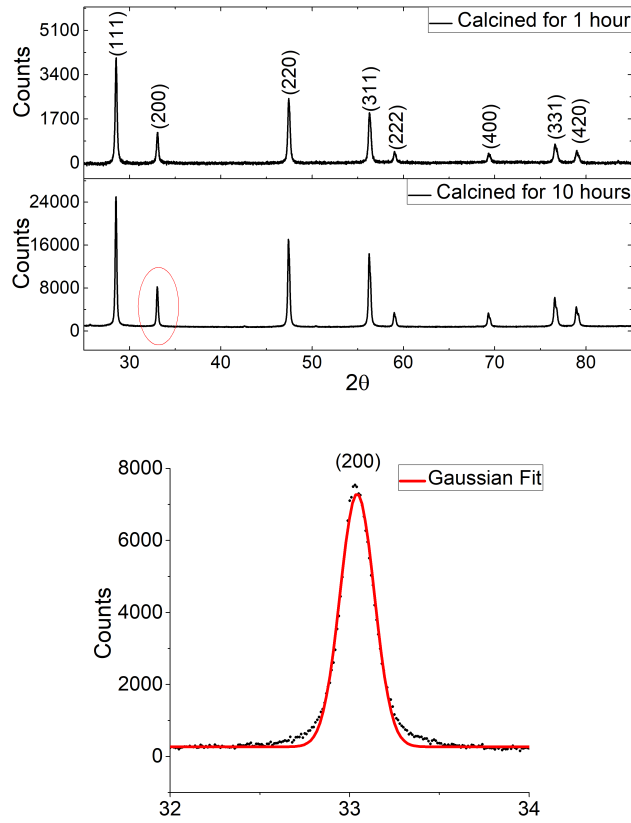


Figure 7.6: Upper: XRD data with indexed peaks from CGO fibres calcined for 1h and 10 h. Lower: Zoom of (200) peak of CGO calcined for 10 hours indicated by red circle in a), the red curve shows a Gaussian fit used for the analysis.

To estimate the effect of the missing wedge on the calculated average equivalent diameter, the diameter was compared to the semi-axis with no elongation using equation 7.3.

$$\delta d = \frac{\sum_{i=1}^N (d_i - 2a_i)}{N} \quad (7.3)$$

where δd is the additional elongation contributing to the calculated mean diameter, N is the number of grains, d_i is the i th computed equivalent diameter, a_i is the i th computed semi-axis length with no elongation.

The result shows that the missing wedge contributed to an elongation of the calculated diameter of 1.11 ± 0.2 for CGO calcined for 1 hour and 0.17 ± 0.3 for the sample calcined for 10 hours.

The result from the sample calcined for 1 hour corresponds well with the deviation from XRD data. It is therefore likely that the larger diameter is caused by the missing wedge.

The OMiTEM results agree with XRD results proving that the 3D-OMiTEM method

is suitable for determining crystallite sizes as well as grain size depending on how the misorientation tolerance is set. These results furthermore indicate that one fibre is representative of the whole powder sample in regards to crystal orientations as all samples, both powders and fibres, proved to have random crystal orientation. However, the sample thickness should not be thicker than 200 nm for CGO with the collection parameters used since it starts to become difficult to resolve the inner part of the sample.

To further evaluate the feasibility of the technique applied on CGO fibres, beam damage was visually inspected qualitatively from BF images. BF images were recorded before and after a full OMiTEM acquisition. No beam damage was observed in the images with a pixel size of 1 nm (see figure 7.7). However, previous attempts showed that applying OMiTEM using conventional carbon supported grids can be problematic since they suffer from beam damage. In this work, a TEM grid with a 50 nm silicon nitride window was used to avoid any beam damage of the support resulting in unwanted rotation of the sample.

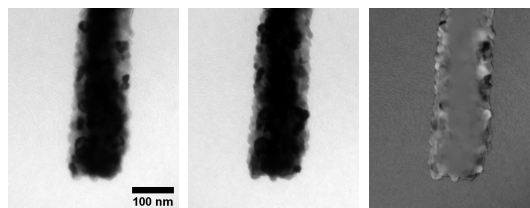


Figure 7.7: CGO calcined at 800C before (left) and after (middle) full OMiTEM collection. The image to the right shows the two images subtracted. The scale is equal for all the images and shown on the left image.

7.5.2 Determination of the Ion percolation Path using 3D-OMiTEM and EFTEM

From the orientation- and structural analysis it is obvious that we can extract overall information from the sample not only on one slice of material but the whole sample in one measurement. This gives us good statistics as well as local information of the entire sample providing new possibilities of extracting information and understanding fundamentals of nano-structured materials. In the following, for the first time, some of the possibilities of 3D orientation map generated by 3D-OMiTEM are demonstrated.

The misorientation of grains can be used to find the local GB doping concentration, as Bowman et al. (2020)⁹. To find the linear relationship between the misorientation and the doping concentration, EFTEM atomic ratio mapping as described in^{32,35} was acquired

(figure 7.8a) followed by 3D-OMiTEM (figure 7.11b) of the same flat area. With the EFTEM technique only two elemental maps are required avoiding time consuming EELS profiles.

The powder sample mostly contain electrospun fibres. However, in some areas the grains have not formed a fibre but rather a flat band. This is ideal for measuring EFTEM since the sample is thin in these areas. Figure 7.8b shows a BF image of such a band.

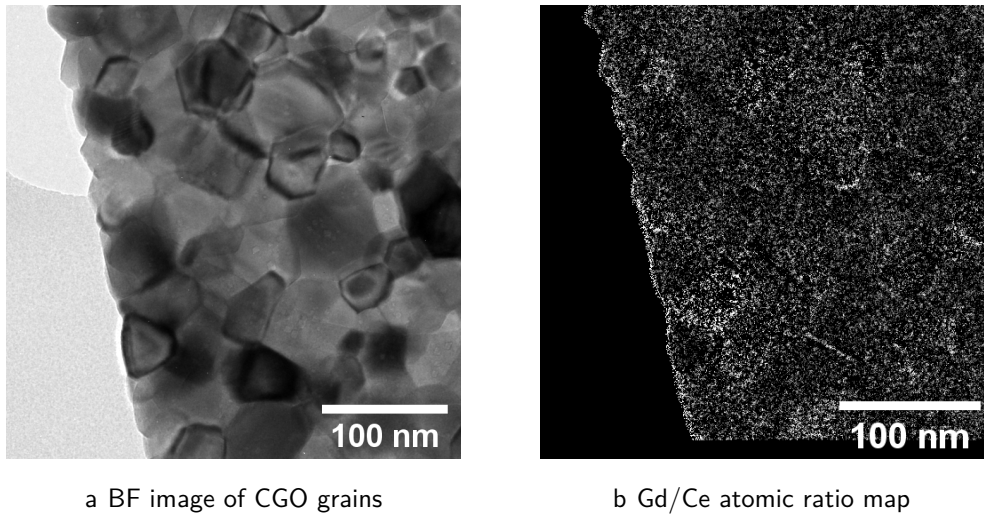


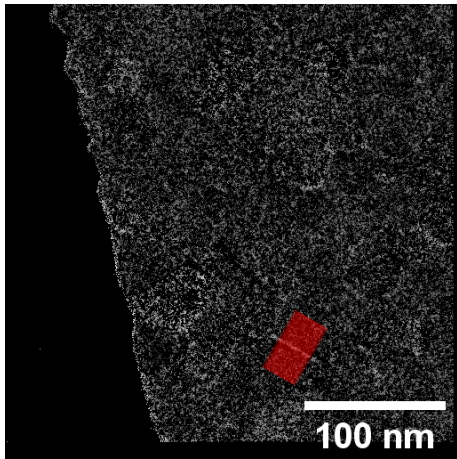
Figure 7.8: Images of CGO grains on a flat area of the sample used for EFTEM atomic ratio mapping and OMiTEM

Using atomic ratio mapping an elemental map of Gd/Ce can be produced. To calculate the absolute concentrations of the gadolinium, the stoichiometry of cerium when doping with gadolinium is used. The doping solute, in this case Gd^{3+} , replace the host cations Ce^{4+} and creates an oxygen vacancy that enhance the ion conductivity. Apart from this it is also a well known phenomena that cerium can change its valence state at the surface of the sample or at the grain boundary from 4+ to 3+ creating more oxygen deficiencies. Thus the chemical formula for gadolinium doped ceria is: $Gd_yCe_{1-y}O_{2-\frac{y}{2}-\delta}$ where $y/2$ is the oxygen deficiency stemming from the Gd and δ is the extra oxygen deficiency stemming from Ce change in valence state.

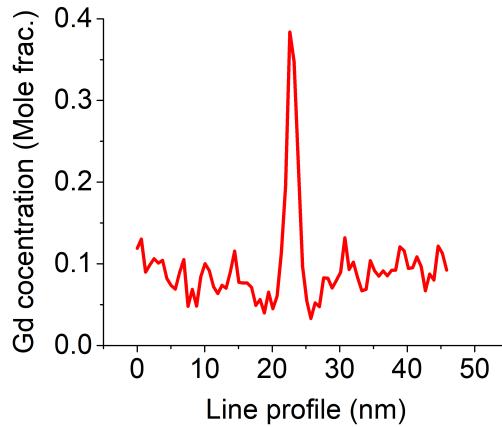
From this it is noticed that the doping concentration y can be found from the ratio map since

$$\frac{Gd}{Ce} = \frac{y}{1-y} \Leftrightarrow y = \frac{Gd/Ce}{Gd/Ce + 1} \quad (7.4)$$

To minimize the noise in the data the gadolinium and cerium elemental maps are filtered using a non-linear means filter in Matlab and a map of y is constructed (Figure 7.9).



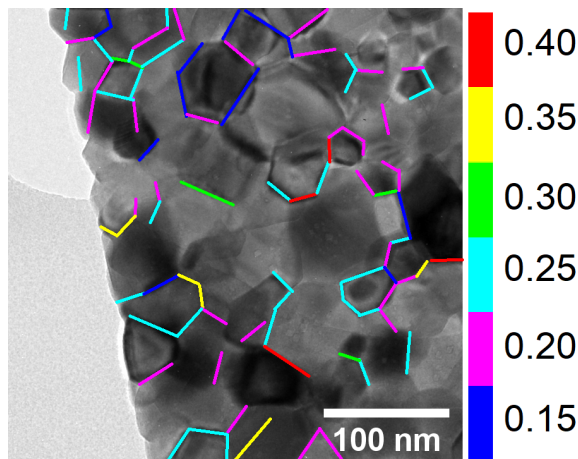
a Gadolinium-map. Red line show the position of the line profile in b)



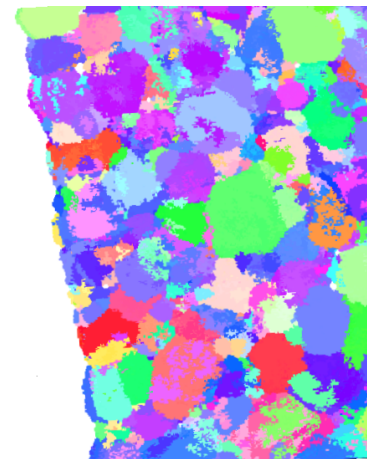
b line profile from position shown in a)

Figure 7.9: Line profiles for determining GB doping concentration

This image now shows a gadolinium doping concentration map and by using a line profile it is possible to determine the concentration in the GBs. This was done for all visible GBs and at the surface. The result is overlaid a BF image and shown on figure 7.10(a). To correlate these found doping concentrations to the misorientation, an orientation map was acquired by OMiTEM shown on figure 7.10(b).



a Doping concentration, obtain using EFTEM, overlaid the BF image



b Corresponding orientation map. The scale is the same as in a)

Figure 7.10: Measurement for correlating misorientation with gadolinium doping concentration

The result is shown of figure 7.11c and the linear relationship, in equation 7.5, was

determined from the fit in well agreement with Bowman et al. (2020)⁹.

$$[A^{3+}] = 8 \cdot 10^{-2} + 4 \cdot 10^{-3} \cdot m \quad (7.5)$$

Where m is the crystallographic misorientation angle of neighbouring grains. The standard deviations of the fit was: $\sigma_{slope} = 0.3 \cdot 10^{-3}$ and $\sigma_{intercept} = 1 \cdot 10^{-2}$.

The EFTEM result furthermore revealed that at the surface the gadolinium content was the same as that of a grain boundary with approximately 62° misorientation, which is the highest for a cubic structure.

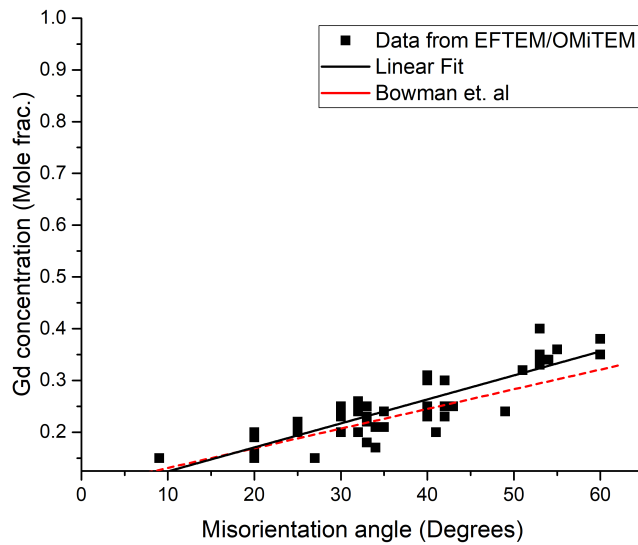


Figure 7.11: Plot showing the linear relationship between misorientation angle and doping concentration. Black squares show the data found in this work with OMiTEM and EFTEM atomic ratio maps. The red line is the linear fit found by Bowman et al⁹

From the local doping concentration, the activation energy and thereby the resistivity can be mapped using equation 7.1, 7.2 and 7.5. As Bowman et al. (2020) n_v^{GB} was approximated to be $\frac{[A^{3+}]_{GB}}{2}$ and β_{GB} was set to 10^3 .

A slice through the middle of the calculated resistivity map, is shown on figure 7.12c and 7.12d. Here the grain interior has been assigned with the value of $\rho=1E3 \Omega \text{ cm}$ as in¹⁰ at 440°C.

A possible ion percolation path is obtained by locating the path with the lowest resistivity in the fibre. This is done by distributing starting points evenly at the end of the fibre.

Furthermore, the surface resistivity was set to have the value as at a grain boundary with 62° misorientation. The obtained percolation path is presented in figure 7.12a and 7.12b.

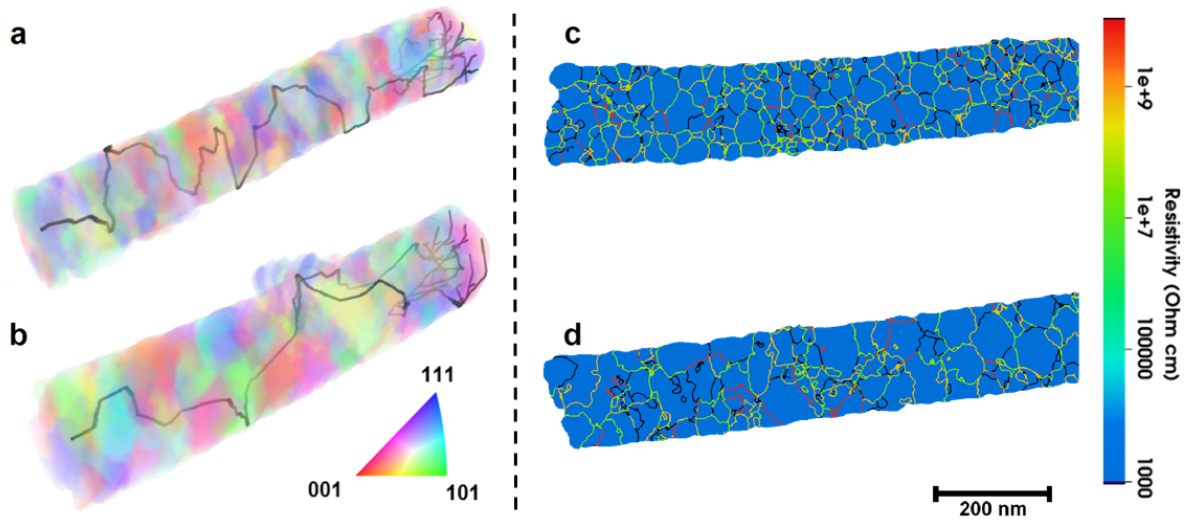


Figure 7.12: Visualization of percolation path and resistivity. a and c show the structure of a CGO nanofibre calcined at 800°C for 1 hour, b and d is the structure of a CGO nanofibre calcined at 800°C for 10 hour. a and b is the 3D visualization including the percolation path. The black path represents the ion percolation path with the smallest resistance. The colors are IPF colors visualizing different orientations. c and d shows a slice through the middle of the sample showing the calculated resistivity at 440°C . The grain interior has been assign with the value of $\rho=1\text{E}3 \Omega \text{ cm}$. The colors represent the resistivity in the structure.

Figure 7.12a and 7.12b demonstrates for the first time the percolation path at such high resolution in 3D. With the 3D information it is possible to determine the percolation path with minimum resistance. This is done for the entire 3D structure and not just for a 2D slice.

To study the percolation path further, the diameter of the nanofibres are virtually shrunk to predict the relation between conductivity and fibre diameter.

The results on figure 7.13 show how the effective resistivity of the percolation path increases as the fibre becomes smaller, with a more rapid increase as the fibre diameter approaches zero. This is a consequence of the fibre containing fewer grains and grain boundaries as its diameter diminishes, leading to an increased probability of the percolation path having to cross a grain boundary with high resistance or having to travel on the surface. The onset of the more rapid increase in resistivity can be seen to occur at small fibre diameters ($< 20 \text{ nm}$). This corresponds roughly to when it would expected that

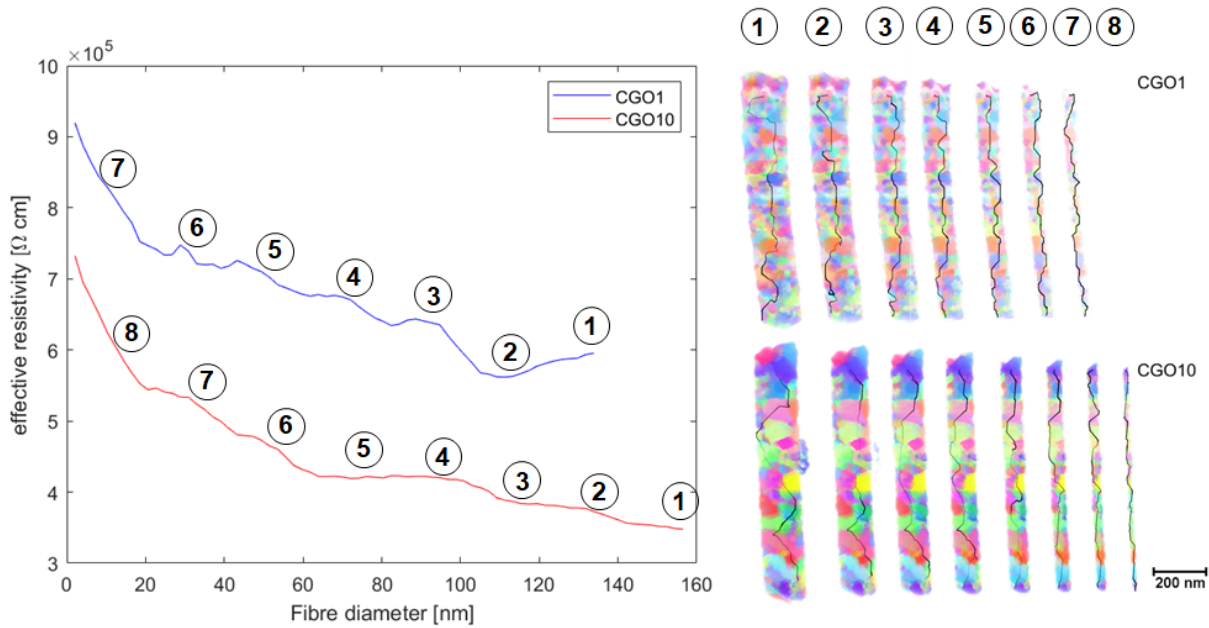


Figure 7.13: Left: Percolation path resistivity as a function of fibre diameter at the narrowest point on the fibre for the CGO calcined for 1 hour and CGO calcined for 10 hours. The largest plotted fibre diameter corresponds to the unaltered fibre before erosion. Right: 3D reconstruction of eroded CGO fibre calcined for 1 hour and 10 hours. Numbers indicate the position on the graph.

the fibre cross section only contain a single grain. With no alternatives for less resistive grain boundaries the percolation path must pass the present grain boundary even at a high resistance i.e. the rapid increase corresponds to a change from few alternative grain boundaries to no alternative grain boundaries.

The percolation path in the CGO fibre calcined for 10 hours is seen to have a significantly lower effective resistivity than the CGO fibre calcined for 1 hour ($3.49 \cdot 10^5 \Omega \cdot \text{cm}$ vs. $6.06 \cdot 10^5 \Omega \cdot \text{cm}$). The main contribution to the resistance in the percolation path comes from crossing grain boundaries rather than the bulk CGO resistivity. The increased effective resistivity in the CGO fibre calcined for 1 hour can thus be explained by the smaller grain size, leading to an additional number of grain boundaries to be crossed in the percolation path.

This study reveals that 3D-OMiTEM is a feasible tool to visualize crystal orientation in polycrystalline nanofibres in 3D non-destructively. The results showed that CGO1 and CGO10 are indistinguishable with regards to the global crystal orientation distribution and only the grain size separates them. From this, and the calculations of the resistivity it is concluded that the conductivity of the nanofibres are both affected by the grain size

and the fibre diameter.

The work offers an insight into the possibilities of 3D-OMiTEM. 3D-OMiTEM can be used to gain 3D orientation information locally on the entire sample enabling orientation- and structural analysis which ultimately can predict possible ion percolation paths. This can prove to be a strong tool to understand the fundamentals of grain boundaries in solid oxide cells and a step closer to understanding pathways in polycrystalline solids to support the development and optimization of devices for energy conversion.

7.6 Conclusion

To summarize 3D-OMiTEM has been successfully applied on state-of-the-art material for SOFC electrodes namely electrospun CGO nano-fibres. The result was 3D-orientation maps with nm-resolution. These maps contained full reconstructed information from the interior of 200 nm fibres with 400-700 grains per sample. This revealed that electrospun nanofibre have a random isotropic crystal orientation and that the mean grain size increase with increasing calcination time.

We showed that with 3D-OMiTEM it is possible to obtain possible ion percolation paths if prior information about the sample is known. This can potentially enable determination and understanding of overall conductivity in polycrystalline samples.

To evaluate the technique it was shown that no significant beam damage was found when using a 50 nm thick silicon nitride support. Furthermore, grain sizes found by 3D-OMiTEM was supported by XRD findings.

In conclusion, 3D-OMiTEM is a feasible tool for microscopists to visualize crystal orientation in polycrystalline samples in 3D non-destructively and that the percolation path can be determined from such a map. This can prove to be a strong tool to understand the fundamentals of grain boundaries in solid oxide cells.

Chapter 8

Preliminary Method Development for Measuring Conductivity of Single Nanofibre

The aim of this chapter is to describe the progress made for measuring the conductivity of electrospun nanofibres during this project. This chapter will describe the approaches and challenges when measuring conductivity of single electrospun gadolinium doped ceria (CGO) nanofibres.

Measuring the conductivity of each individual nanofibre would allow for a more detailed understanding of how the structure and texture of the nanofibre affects the conductivity. It would serve to help at assigning the correct value of the resistivity of the grain interior making the calculated total conductivity trustworthy and it would be possible to compare the grain boundary conductivity calculated from the ion conductivity path to the measured.

The main problem when measuring conductivity of a single nanofibre is the dimensions. The nanofibres have a diameter of approximately 200 nm and a length of 1-3 μm . Contacting such small samples is very challenging. During this project two approaches have been tested. The first approach was to attempt to pick up a single nanofibre and place it on two electrodes. However, this proved to be very time consuming as the sample (in this case CGO) was very brittle and would break when touching it. The second approach was to dropcast multiple nanofibres onto a microchip with electrodes and remove nanofibres if more than one was positioned across the electrodes. Finally, platinum was deposited on top of the ends of the fibre in contact with the electrodes

on the microchip. This approach was the most promising and will be described in this chapter.

8.1 Experimental

Scanning Electron Microscopy

Scanning Electron Microscopy (SEM) was done using a Hitachi table top SEM TM3000 with an acceleration voltage of 15 keV and a secondary electron detector.

Scanning Transmission Electron Microscopy and Energy Dispersive Spectroscopy

Scanning Transmission Electron Microscopy (STEM)- and Energy Dispersive Spectroscopy (EDS) images were acquired using a Jeol2100 TEM-LaB6 at 200 keV with a single tilt holder and an annular dark-field (DF) detector. The EDS maps were acquired for approximately 30 min and Pt M maps were created.

Electron Beam Induced Deposition

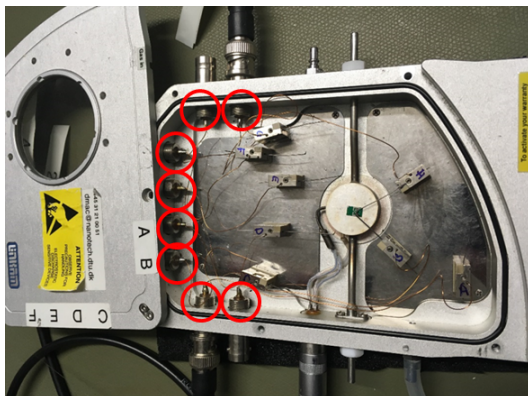
Electron Beam Induced Deposition (EBID) was done on a Zeiss Cross Beam 1540XB with a platinum source at different parameters as described later in this chapter.

IV-measurements

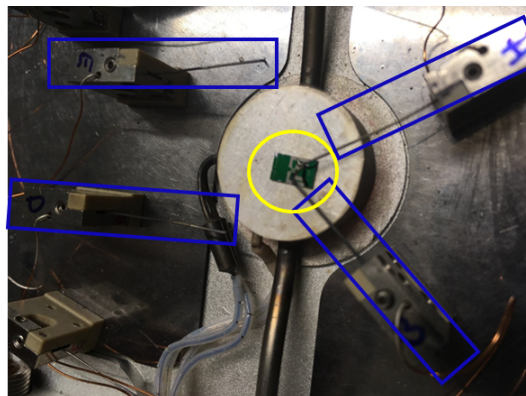
Conductivity measurements or IV-measurements were done using a Linkam LTS600P stage connected to a Keithley 2400 Source Meter SMU and a Keithley 2000 digital Multimeter. The potential between two electrodes was ramped up while measuring the current.

8.2 Set-up

The set-up for measuring the conductivity was a Linkam LTS600P stage connected to a Keithley 2400 Source Meter SMU and a Keithley 2000 digital Multimeter, controlled by Labview and located at DTU Physics. The stage is shown on figure 8.1. It has 8 probes that can be placed on microchips with electrodes down to ~ 200 μm in width. The probes are attached to the stage with magnets to avoid movements during measurement. Furthermore, the stage is equipped with a hot plate enabling measurements at temperatures up to approximately 600°C . The set-up is placed at a grounded table and to avoid damaging of the small nanofibres it is possible to ground the user using a bracelet connected to the table. The stage is connected to a Keithley enabling precise control of the potential or current between the electrodes. The set-up can measure currents down to 1 pA.



a Overview image showing Linkam stage. Red circles frame the connection to the outside of the box.



b Linkam stage zoomed in on the sample where two probes are connected. Blue squares show the probes for connection with magnets for attachment. Yellow ring frames the sample.

Figure 8.1: Set-up for conductivity measurements with Linkam stage.

8.3 Chip Design

The probes in the Linkam stage can be connected to microchips with down to $\sim 200 \mu\text{m}$ wide electrodes. Two chip designs were used with wide electrodes for connection and thinner electrodes for placing the nanofibres. The two chip designs are shown on figure 8.2 and 8.5.

Chip design 1 was designed at DTU Physics and fabricated by microfabrication at DTU Danchip by Johachim Dahl Thomsen⁸³. Any additional information on the microfabrication process can be found in⁸³. The design fits into a protochips holder for in-situ TEM measurements and can also be used in the Linkam stage. The chip has four electrodes (either platinum or gold) with a spacing between them of $3\text{-}5 \mu\text{m}$ (figure 8.2). In the spacing in the middle there is a hole for the electron beam enabling TEM analysis of this area. The spacing can be varied by changing the chip design and can potentially be made down to 100 nm limited by the microlithography process.

The nanofibres are dropcasted onto the chip and the idea is to find a fibre that can be connected with small electrodes being deposited later. Then all excess fibres between the contacts of interest are removed by focussed ion beam or by a Kleindiek micromanipulator. Dropcasting was done on four different chips with chip design 1. SEM images are shown on figure 8.3.

When dropcasting the fibres, ethanol is mixed with the fibres, the solution is sonicated for 20 seconds and dropcasted directly onto the substrate. On normal TEM grids or

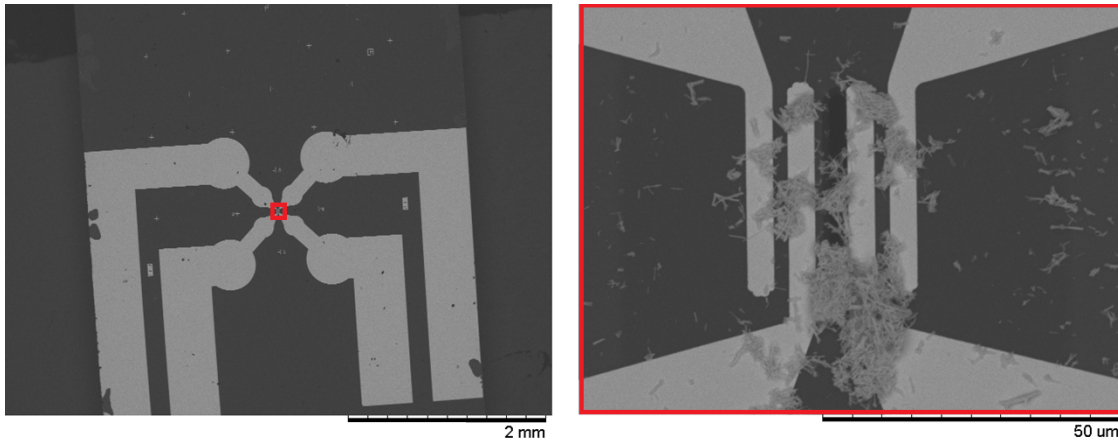


Figure 8.2: SEM image of chip with design 1. The design has four large electrodes for four point measurement. The spacing between the electrodes are 3-5 μm . Left image shows an SEM overview image of chip. Right image shows a magnified area indicated by red square in left image. Between the two middle electrodes is a hole enabling TEM imaging. The light gray fibers are CGO nanofibres dropcasted onto the grid.

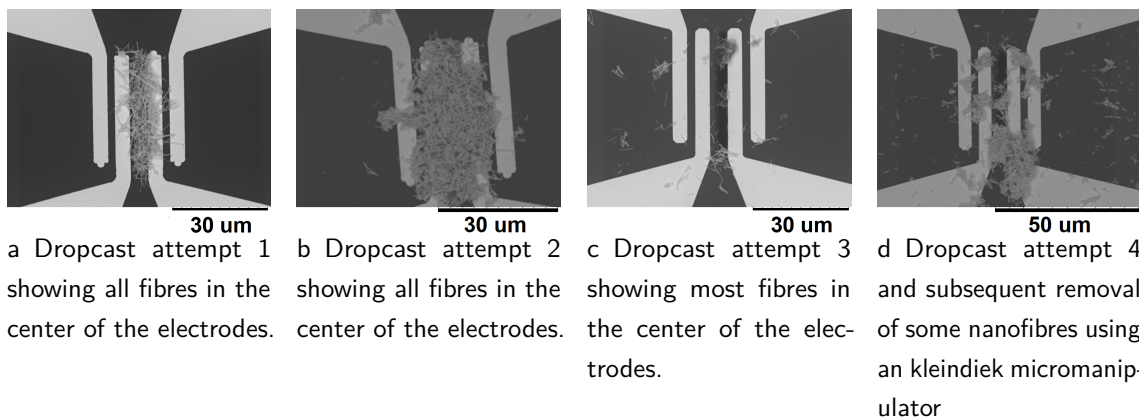


Figure 8.3: SEM images of four chips with design 1. The images show the location and distribution of CGO nanofibres after dropcast.

silicon nitride substrates this leaves the nanofibres separated and evenly spread on the substrate (for example see figure 8.4). However, as can be seen to the right on figure 8.2 and figure 8.3, the fibres tend to cluster in the spacing of the electrodes. This could be explained by capillary forces dragging the solution to the hole in the middle of the electrodes leaving the fibres clustered.

When using the kleindiek micromanipulator to remove some fibres, all fibres in the cluster were moved and would break. As a consequence it was practically impossible to keep just one fibre (see figure 8.3d).

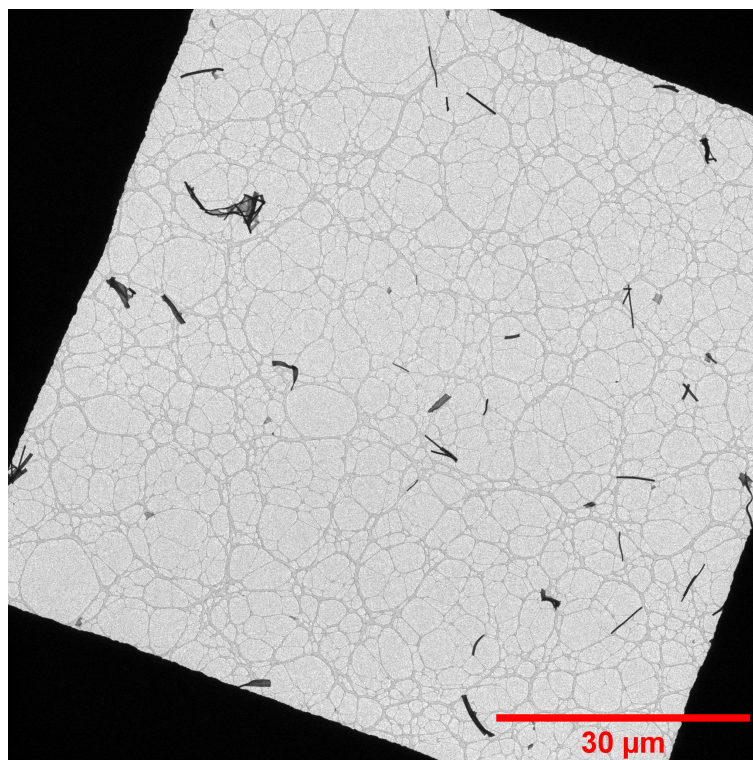


Figure 8.4: BF TEM image at low magnification showing an overview of how fibres are distributed after dropcast.

With this design the fibre to be measured should be in one of the three spacings between two neighbouring electrodes to enable subsequent connection. This makes it practically impossible to contact four electrodes enabling 4-point measurements. Thus, with this set-up only a 2-point measurement of single nanofibres are possible.

During this project it was found that this set-up is suitable to measure the resistance of multiple clustered nanofibres. However, it was difficult to estimate the geometry and thereby determine the conductivity from an IV-measurement. Therefore, a new chip design was developed.

The new chip design is shown on figure 8.5. Chip design 2 can be fabricated by microfabrication as design 1. However, to make a quick test of the design a shadow mask was created and gold was sputtered directly onto a commercial 50 nm silicon nitride support on a 200 μm silicon frame for TEM. The silicon nitride support had a window size of 0.5x1.5 mm designed for high-tilt tomographic applications enabling imaging with up to 75° tilt.

The shadow mask was clamped onto the TEM silicon nitride chip and, using sputter coating, gold was deposited on the desired regions forming electrodes. The result is

shown on figure 8.5. With this method the fibres can be dropcasted evenly and separated as they are directly dropcasted onto the TEM silicon nitride chip. The final chip will be more robust if all steps are done by microfabrication. Then a thin titanium layer or other adhesion layer could be deposited between the gold and silicon substrate to avoid delamination of the gold electrodes.

Chip design 2 has a vertical spacing between the electrodes of $\sim 60 \mu\text{m}$ and a horizontal spacing of $\sim 40 \mu\text{m}$ (see figure 8.5 to the right). With this design the nanofibres can be connected with subsequent electrode deposition if the fibre is positioned between two electrodes leaving a larger area for the nanofibres than design 1. This also opens up for 4-point measurements as it is easier to connect the fibre to 4 electrodes. Furthermore, the design can be used for tomography with up to 75° tilt enabling 3D-OMiTEM acquisition before or after a conductivity measurement. This would make it possible to get conductivity measurement and orientation measurement in 3D of the same fiber which could contribute to the understanding of how orientation affects the conductivity.

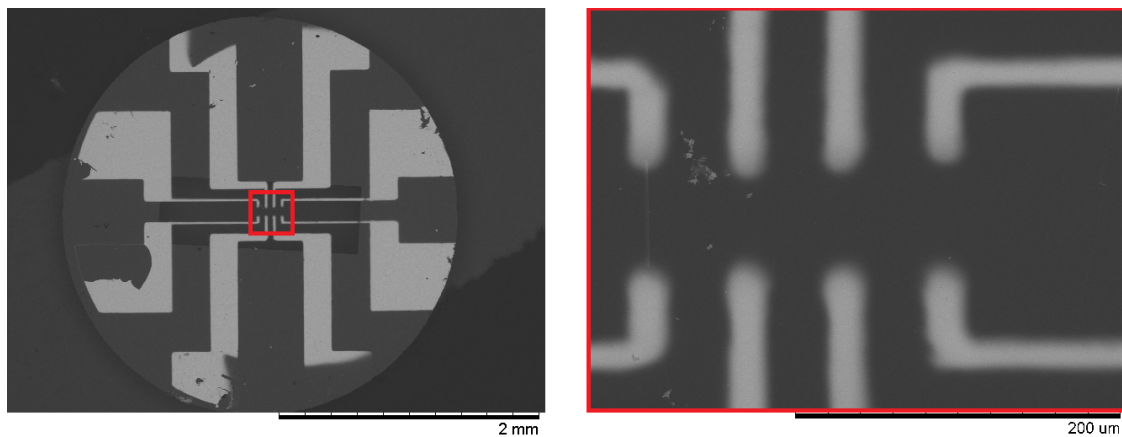


Figure 8.5: SEM images of Chip design 2. 50 nm silicon nitride window on a thick silicon frame fitting in a normal TEM holder. 8 gold electrodes are deposited on top. Left image shows an overview image of the whole chip. Right image shows a magnification of the area indicated by a red square in the left image.

To connect the fibres to the electrodes, Electron Beam Induced Deposition (EBID) was used to deposit thin platinum electrodes from the fibre to the larger electrodes. To test if it is possible to deposit such long electrodes using EBID, a platinum electrode was deposited between two larger electrodes in the longest distance e.i. in the vertical spacing. This can be seen on figure 8.5 in the image to the right. The platinum electrode is the thin electrode between the two electrodes to the left.

8.4 Electrode deposition

In most sample preparation techniques, metal contacts are deposited using Ion Beam Induced Deposition (IBID). However, IBID is known for creating a large contamination area⁸⁴. Fawey et. al showed an overspray leading to a contaminated area of 17 μm for contacts deposited using IBID. For comparison they reported an over spray of 1 μm for EBID. Since the contaminated area would be larger than the fibre dimensions only EBID is suitable for writing contacts and electrodes for this purpose. However, EBID is known for being a slower technique with higher contact resistance than contacts written with IBID. Protochips has made a measurement of contact resistance for both types of contact and their results showed that the contact resistance was $3.75 \cdot 10^3 \mu\Omega \cdot \text{cm}$ for EBID deposition and $25 \mu\Omega \cdot \text{cm}$ for IBID deposition⁸⁵. However, EBID deposition contact resistivity could be reduced to $90 \mu\Omega \cdot \text{cm}$ by annealing the sample at 300°C in an oxygen rich environment for 10 min⁸⁵. The resistivity of the CGO nanofibres, calculated by the path of least resistance in chapter 7, were approximately $3.5\text{-}6 \cdot 10^5 \Omega \cdot \text{cm}$ which is orders of magnitude larger than the contact resistivity and the EBID electrodes should be sufficient for the purpose of measuring CGO nanofibre conductivity. Even if no grain boundaries are present in the structure the resistivity should be $1000 \Omega \cdot \text{cm}$ still orders of magnitude larger than the contact resistivity.

To determine suitable parameters for the EBID, electrodes were deposited with different parameters. All electrodes were deposited using a working distance of 5 mm, acceleration voltage of 2 keV and using high current mode. The rest of the parameters were varied and are summarized in table 8.1. A corresponding overview image with the different electrodes is shown on figure 8.6.

Electrode	Exposure Time (s)	Scan Speed (step number)	Length (μm)	Width (μm)
1	120	14	5	0.6
2	120	9	25	0.3
3	120	14	25	0.3
4	60	14	25	0.3
5	30	14	5	0.3

Table 8.1: Parameters for EBID. All other parameters were constant.

The slowest scan speed of the microscope was 1 and the fastest was 14. The overview image shows that the fastest scan speed was the best as the electrode with the slowest

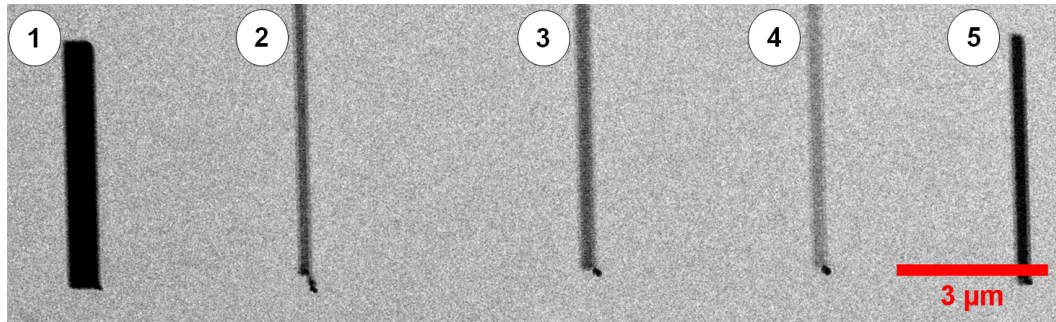


Figure 8.6: Overview of electrodes deposited with Electron Beam Induced Deposition (EBID). The corresponding parameters used for the EBID are summarized in table 8.1.

scan speed (electrode 2 on figure 8.6) showed evidence of drift at the starting point of the electrode deposition showing up as multiple spots on a line. The longest exposure time was 120 s as this was the longest time the pressure in the chamber, due to Pt gas, was constant before dropping. The test shows that 25 μm long electrodes can be deposited with high precision in a couple of minutes.

To further investigate the quality of the electrodes and the contamination area STEM-EDS was used to create a platinum map. The result is shown on figure 8.7 and 8.8 and shows the DF-STEM images and their corresponding EDS platinum maps. A lineprofile is of the HAADF STEM image is shown on figure 8.9.

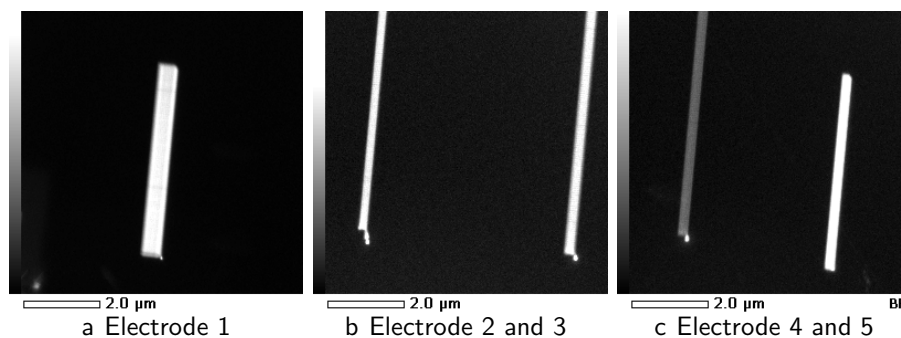


Figure 8.7: DF-STEM of EBID electrodes.

The line profile on figure 8.9 shows that the electrode is well defined. The EDS results on figure 8.8 show in general that there is no obvious contamination area and no platinum was deposited outside the electrodes. The contrast in the STEM images on figure 8.7 show the amount e.i. the thickness of the platinum. Thus, the STEM results, together with the EDS results, show that the fastest scan speed is the best for creating electrodes and that the short electrodes have the highest amount of platinum as expected since the same amount of platinum is deposited on a smaller area. Finally, the results show that

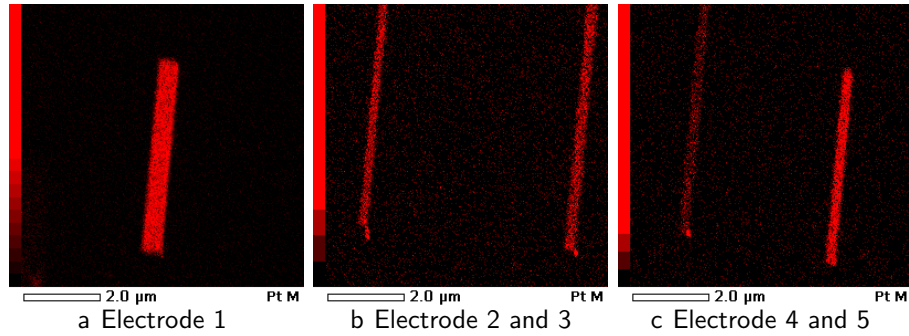


Figure 8.8: Corresponding EDS Pt M maps of EBID electrodes on figure 8.7.

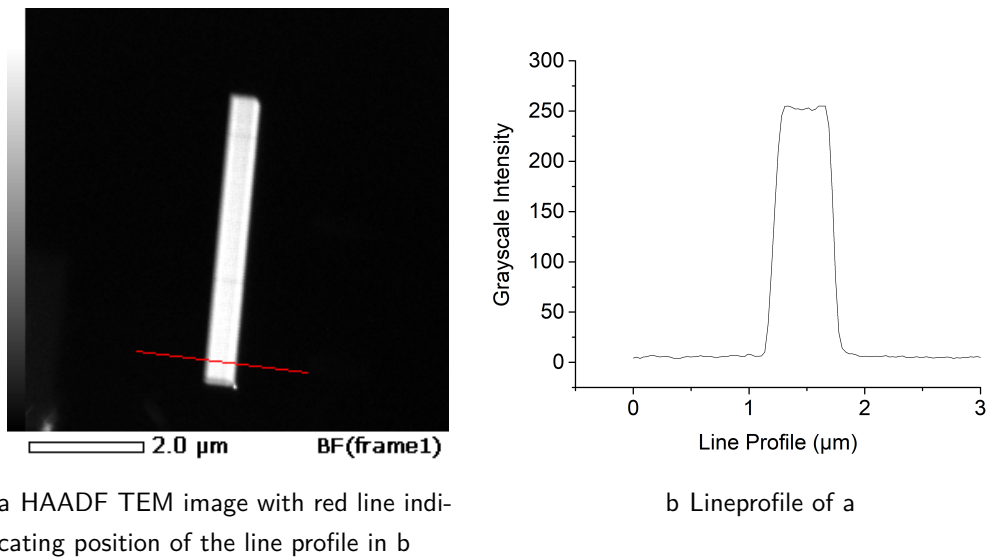


Figure 8.9: Grayscale profile over electrode

25 μm electrodes can be successfully created without a significant contamination area in a couple of minutes making it suitable for writing small electrodes for connecting the nanofibres to the larger electrodes.

8.5 Measuring IV curves

The set-up on figure 8.1 was tested by measuring an IV-curve of the cluster of fibres on figure 8.3b at room temperature. Platinum was deposited by EBID on top of the electrodes to create better contacts. Then the potential was ramped up while measuring the current. The result is shown on figure 8.10.

The result of the linear fit on figure 8.10 gave a slope of $4.61 \cdot 10^{-8} \pm 7 \cdot 10^{-10} \Omega^{-1}$. This shows that with this set-up it is possible to measure a currents down to $\sim 0.5 \text{ nA}$. The

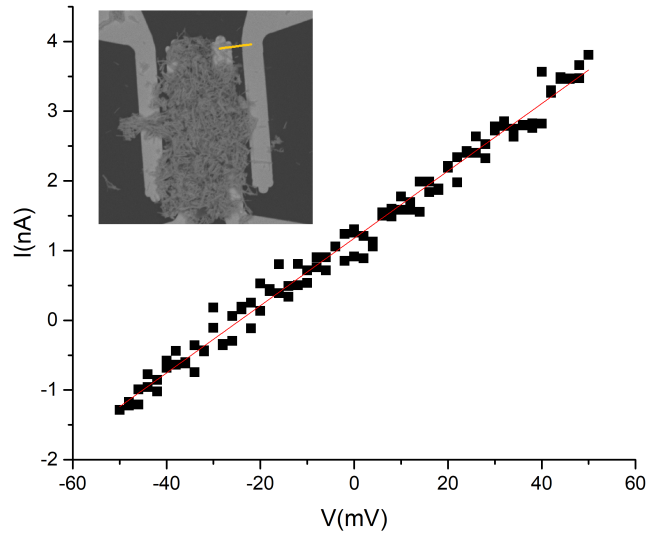


Figure 8.10: IV curve for determination of resistivity of multiple nanofibres. The measurement was done over the two electrodes to the right, shown by a yellow line in the inset image. The red line is a linear fit.

set-up should be able to measure down to pA. However, the quality of the electrical contacts in the set-up can reduce the sensitivity.

In chapter 7 the resistivity at 440°C of the CGO nanofibres were found to be $\sim 3 \cdot 10^5 \Omega \cdot \text{cm}$ e.i. the resistance of a single nanofibre with a radius of 100 nm and a length of 1 μm is:

$$R = \rho \frac{l}{A} = 3 \cdot 10^3 \Omega \cdot \text{m} \cdot \frac{1 \cdot 10^{-6} \text{m}}{(100 \cdot 10^{-9} \text{m})^2 \pi} = 1 \cdot 10^{11} \Omega \quad (8.1)$$

Thus in order to measure nA a potential of 100 V should be applied. Alternatively, the temperature of the nanowire could be increased since it follows equation 7.1 this will increase the conductivity and thereby decrease the resistivity.

8.6 Conclusion

In this chapter the preliminary results of the method development for measuring conductivity of a single electrospun nanofibre were presented. Two potential microchip designs were presented from which design 2 proved to be the most promising. With this design direct dropcasting can be used to place nanofibres on the chip without clustering as oppose to design 1. The design enables tomographic tilting and can therefore be used for 3D-OMiTEM subsequent or prior to the conductivity enabling both measurements of the same fibre. Furthermore, chip design 2 enables the possibility of measuring both

2-point measurements and 4-point measurements. Microfabrication should be used for creating both types of chips to ensure high quality contacts that do not de-laminate.

Small EBID contacts can be used to contact the fibres to the large electrodes on the chip. The contact resistivity is low enough for measuring conductivity of CGO. EBID is a promising technique as it proved to be able to write long electrodes (25 μm) in a couple of minutes without any significant overspray or contamination area.

The set-up can measure small currents down to 1 nA enabling conductivity measurements of single nanofibres. However, grounding bracelets is important for avoiding damaging the nanofibres. The applied voltage should be approximately 100 V for measurements at 440°C. Alternatively, for lower voltage, the temperature could be increased.

Chapter 9

Conclusion

This thesis has shown potentials and challenges of 3D-OMiTEM by applying the technique on three different materials namely a silver nanowire, maghemite nanoflowers and CGO nanofibres.

The results from the silver nanowire case showed that 3D-OMiTEM successfully measures the orientations predicted by theory. It showed no deviations in the crystal planes along the nanowire, as they were all $\{101\}$, and the twinning structures was clear in the GBCD analysis. However, the example also shows that great care must be taken to avoid beam damage by reducing the total exposure time. As a consequence this shows that 3D-OMiTEM is challenging to apply on beam sensitive samples and the acquisition parameters should be well thought off before acquisition.

The maghemite nanoflowers results first and foremost showed the potential for using 3D-OMiTEM for statistical analysis of crystallites in ensembles of nanoflowers. The results showed that it was possible to extract crystalline size and nanoflower size, e.i. agglomerate size simultaneously from one measurement. This has previously been done using different techniques and the analysis could not be made on single nanoflowers but only on the average of the whole ensemble. The results showed that as the agglomerate size increased so did the largest crystallite in the agglomerate while the average crystallite size practically did not change. XRD result would therefore have shown only the constant average crystallite size. This type of results with the whole 3D information with orientation and morphology can potentially be used in future work as input to simulations for determining the magnetization of the nanoflowers and on the ensemble of nanoflowers giving new insides to this type of material. The crystallites had an average diameter of 6 nm while the spatial resolution at the used magnification and sample tilt angles was ~ 3

nm. From the results we can conclude that the morphology and statistics of hundreds or even thousands of crystallites can be extracted, from a 3D-OMiTEM reconstruction, to find crystallite size distribution while at the same time getting information of the whole sample geometry.

To summarize the results showed that 3D-OMiTEM successfully determined the crystal orientation of the sample enabling analysis of grain boundaries. Furthermore, 3D-OMiTEM can be used to study the sample geometry as well as the morphology of hundreds or thousands of grains enabling morphology statistical analysis including particle size distribution. However, great care must be taken to avoid beam damage and the sample tilt range should be as high as possible to avoid elongations of the grains.

All of this combined was used together to reach the main aim of this work. Namely to study the effect of orientation on doping concentration in the grain boundaries to ultimately predict ion percolation paths to characterize the overall performance of the materials in SOCs. For the first time, 3D-OMiTEM was applied successfully on polycrystalline functional materials for energy conversion devices namely on electrospun CGO nanofibres. Prior to this, a small flat part of the sample was studied by EFTEM and 3D-OMiTEM to plot the doping concentration as a function of grain boundary misorientation. The result showed a linear relationship between the misorientation and the doping concentration. High grain boundary misorientations proved to have the highest doping concentration. This, for the first time, enables the prediction of the ion percolation path with the least resistance through the fibre. With this knowledge 3D-OMiTEM was applied successfully on a fibre and the resistivity could be calculated directly from the misorientation by converting this to a doping concentration. The result shows the great new potentials of 3D-OMiTEM. Since it is a TEM based technique it opens up for prior or subsequent analysis using other TEM based techniques e.g. compositional analysis all with a resolution down to 1 nm as shown by Liu et al. (2011)²⁰. This opens up for a variety of new analysis in the TEM.

It would be interesting to compare conductivity calculated from the 3D-OMiTEM/EFTEM results with a measured conductivity. Therefore, preliminary steps were taken, during this work, to find the optimal setup for this. Because of the small dimensions of the fibre, measuring the conductivity of a single fibre is challenging. Two chip designs were presented of which one of them proved to be the most promising. The chip is based on the design from a chip for TEM tomographic applications. It is a silicon based chip with a silicon nitride window enabling TEM characterization at high angles. To enable conductivity measurements the chip is fabricated with larger electrodes with connection

paths of 200 μm in width. This makes sure that the electrodes can be connected to a Linkam stage for controlling the measurement. Finally, small electrodes are connected by writing them with EBID. This technique proved to create electrodes with sufficiently low contact resistance and the technique proved to produce well defined electrodes with minimal contamination area. The design enables 3D-OMiTEM prior or subsequent to the conductivity measurement. However, the chips were prepared with a quick shadow mask and sputter coating to do a quick test and as a result the electrodes would easily peel off. Therefore, the hole chip should be fabricated in a clean room facility to produce high quality chips with an adhesion layer between the electrodes and the chip.

9.1 Future Work

A major outcome of this work was the prediction of ion percolation paths in CGO nanofibres. A direct comparison to a measured conductivity would be very beneficial. As previously described this is very challenging. However, in this work a chip design was proposed. To complete the task of measuring conductivity of a single nanofibre, the chip design should be fabricated in a clean room facility with an adhesion layer between the electrode and silicon substrate. The chip design should be straight forward in regards to clean room fabrication.

First of all it would be beneficial to measure the resistivity of the EBID electrodes to test if the resistance is low enough as predicted by the protochips results⁸⁵. This could be done by shorting two of the electrodes on the chip by writing the EBID electrode between them. Then the resistivity of the EBID electrode could be measured. Also a 4-point measurement could be of interest separating contact resistance from the measurement. This could be done by writing an EBID electrode between four electrodes.

After the electrode testing the actual measurement of the fibre, in the Linkam stage, could be done by direct dropcasting and writing EBID electrodes to contact the fibre to the electrodes with the parameters found in this work.

Measuring conductivities of fibres calcined at different temperatures would furthermore contribute to the knowledge of conductivity of nanofibres. As a starting point for the conductivity measurement it would be easier to measure a fibre calcined at higher temperatures. This would increase the grain size and thereby also the conductivity making it easier to measure.

In regards to the 3D-OMiTEM technique it would be highly beneficial to the results if the sample tilt range could be increased. There already exists TEM holders for 360°

rotations e.g. the Fischione On-Axis Rotation Tomography Holder model 2050. However, this holder requires a sample prepared by focussed ion beam. This is more time consuming than dropcasting but could give valuable information as the elongation of the morphology would disappear and the spatial resolution would increase. Furthermore, to increase resolution 3D-OMiTEM could be acquired at higher magnification after calibration. This would be highly beneficial especially for the sample of maghemite nanoflowers. The current resolution is close to the crystallite size and it would therefore be interesting to see a more detailed structure. This could also help at determining how good a resolution we can get with 3D-OMiTEM. One challenge when using a too high magnification could be that the sample would move out of the field of view when tilting the sample. This limit would be interesting to find. Furthermore, by calibrating more magnifications 3D-OMiTEM would be applicable to more problems as the magnification could be chosen for the specific sample.

Bibliography

- [1] European Commission; Energy Roadmap 2050, *Policy*,1–9, issn: 14710080. 2012.
- [2] Klima-, Energi- og Forsyningsministeriet; Klima-, energi-og forsyningsministerens redegørelse til Folketinget om klimapolitikken. 2019; <https://kefm.dk/media/7115/klimapolitisk-redegoerelse-2019.pdf>.
- [3] Eurostat; Energy statistics - an overview, ISSN 2443-8219. 2020; https://ec.europa.eu/eurostat/statistics-explained/index.php/Energy_statistics_-_an_overview.
- [4] Eurostat; Renewable energy statistics , ISSN 2443-8219. 2020; https://ec.europa.eu/eurostat/statistics-explained/index.php/Renewable_energy_statistics.
- [5] Energinet, Årsrapport 2019. 2020; <https://energinet.dk/Om-nyheder/Nyheder/2020/03/30/aarsrapport-2019>.
- [6] Minh, N. Q. Solid oxide fuel cell technology - Features and applications. *Solid State Ionics* **2004**, *174*, 271–277.
- [7] Shri Prakash, B.; Senthil Kumar, S.; Aruna, S. T. Properties and development of Ni/YSZ as an anode material in solid oxide fuel cell: A review. *Renewable and Sustainable Energy Reviews* **2014**, *36*, 149–179.
- [8] Kee, R. J.; Zhu, H.; Sukeshini, A. M.; Jackson, G. S. Solid oxide fuel cells: Operating principles, current challenges, and the role of syngas. *Combustion Science and Technology* **2008**, *180*, 1207–1244.
- [9] Bowman, W. J.; Darbal, A.; Crozier, P. A. Linking Macroscopic and Nanoscopic Ionic Conductivity: A Semiempirical Framework for Characterizing Grain Boundary Conductivity in Polycrystalline Ceramics. *Acs Applied Materials and Interfaces* **2020**, *12*, 507–517.

- [10] Bowman, W. J.; Kelly, M. N.; Rohrer, G. S.; Hernandez, C. A.; Crozier, P. A. Enhanced ionic conductivity in electroceramics by nanoscale enrichment of grain boundaries with high solute concentration. *Nanoscale* **2017**, *9*, 17293–17302.
- [11] Jo, S. H.; Muralidharan, P.; Kim, D. K. Electrical characterization of dense and porous nanocrystalline Gd-doped ceria electrolytes. *Solid State Ionics* **2008**, *178*, 1990–1997.
- [12] De Souza, R. A.; Fleig, J.; Maier, J.; Zhang, Z.; Sigle, W.; Rühle, M. Electrical resistance of low-angle tilt grain boundaries in acceptor-doped SrTiO₃ as a function of misorientation angle. *Journal of Applied Physics* **2005**, *97*.
- [13] Waser, R. Electronic properties of grain boundaries in SrTiO₃ and BaTiO₃ ceramics. *Solid State Ionics* **1995**, *75*, 89–99.
- [14] Wang, D. Y.; Nowick, A. S. The "grain-boundary effect" in doped ceria solid electrolytes. *Journal of Solid State Chemistry* **1980**, *35*, 325–333.
- [15] Tanaka, J.; Baumard, J.; Abelard, P. Nonlinear electrical-properties of grain-boundaries in an oxygen-ion conductor(CeO₂.Y₂O₃). *Journal of the American Ceramic Society* **1987**, *70*, 637–643.
- [16] Ye, F.; Yin, C. Y.; Ou, D. R.; Mori, T. Relationship between lattice mismatch and ionic conduction of grain boundary in YSZ. *Progress in Natural Science: Materials International* **2014**, *24*, 83–86.
- [17] Bowman, W. J.; Kelly, M. N.; Rohrer, G. S.; Hernandez, C. A.; Crozier, P. A. Enhanced ionic conductivity in electroceramics by nanoscale enrichment of grain boundaries with high solute concentration. *Nanoscale* **2017**, *9*, 17293–17302.
- [18] Rohrer, G. S.; Saylor, D. M.; El Dasher, B.; Adams, B. L.; Rollett, A. D.; Wynblatt, P. The distribution of internal interfaces in polycrystals. *Zeitschrift Fuer Metallkunde/materials Research and Advanced Techniques* **2004**, *95*, 197–214.
- [19] Rohrer, G. S. Measuring and interpreting the structure of grain-boundary networks. *Journal of the American Ceramic Society* **2011**, *94*, 633–646.
- [20] Liu, H. H.; Schmidt, S.; Poulsen, H. F.; Godfrey, A.; Liu, Z. Q.; Sharon, J. A.; Huang, X. Three-Dimensional Orientation Mapping in the Transmission Electron Microscope. *Science* **2011**, *332*, 833–834.

- [21] Wu, G.; Zhu, W.; He, Q.; Feng, Z.; Huang, T.; Zhang, L.; Schmidt, S.; Godfrey, A.; Huang, X. 2D and 3D orientation mapping in nanostructured metals: A review. *Nano Materials Science* **2020**, *2*, 50–57.
- [22] Larsen, P. M.; Schmidt, S. Improved orientation sampling for indexing diffraction patterns of polycrystalline materials. *Journal of Applied Crystallography* **2017**, *50*, 1571–1582.
- [23] Mason, J. K.; Schuh, C. A. In *Electron Backscatter Diffraction in Materials Science*; Schwartz, A. J., Kumar, M., Adams, B. L., Field, D. P., Eds.; Springer US, 2009; pp 35–51.
- [24] Glowinski, K. Methods for quantitative characterization of three-dimensional grain boundary networks in polycrystalline materials. *Doctoral dissertation* **2015**, Ch. 2.
- [25] Rohrer, G. S.; Randle, V. In *Electron Backscatter Diffraction in Materials Science*; Schwartz, A. J., Kumar, M., Adams, B. L., Field, D. P., Eds.; Springer US, 2009; pp 215–229.
- [26] Glowinski, K. GBtoolbox. http://imim.pl/personal/adam.morawiec/A_Morawiec_Web_Page/S/K_Glowinski/Downloads.html.
- [27] Weyland, M.; Midgley, P. In *Transmission Electron Microscopy: Diffraction, Imaging, and Spectrometry*; Carter, C. B., Williams, D. B., Eds.; Springer International Publishing: Cham, 2016; pp 343–376.
- [28] Carter, C. B.; Williams, D. B. *Transmission Electron Microscopy : A Textbook for Materials Science*; Springer US, 2009; pp 141–171.
- [29] Carter, C. B.; Williams, D. B. *Transmission Electron Microscopy : A Textbook for Materials Science*; Springer US, 2009; pp 257–269.
- [30] Carter, C. B.; Williams, D. B. *Transmission Electron Microscopy : A Textbook for Materials Science*; Springer US, 2009; pp 283–309.
- [31] Carter, C. B.; Williams, D. B. *Transmission Electron Microscopy : A Textbook for Materials Science*; Springer US, 2009; pp 197–209.
- [32] Thomas, P.; Midgley, P. EFTEM. *Transmission Electron Microscopy* **2016**, 377–404.
- [33] Mackenzie, J. K. Second Paper on Statistics Associated with the Random Disorientation of Cubes. *Biometrika* **1958**, *45*, 229.

- [34] Carter, C. B.; Williams, D. B. *Transmission Electron Microscopy : A Textbook for Materials Science*; Springer US, 2009; pp 679–698.
- [35] Hofer, F.; Grogger, W.; Kothleitner, G.; Warbichler, P. Quantitative analysis of EFTEM elemental distribution images. *Ultramicroscopy* **1997**, *67*, 83–103.
- [36] Crowther, R. A.; DeRosier, D. J.; Klug, A. The reconstruction of a three-dimensional structure from projections and its application to electron microscopy. *Proceedings of the Royal Society of London, Series a (mathematical and Physical Sciences)* **1970**, *317*, 319–40, 319–340.
- [37] Radermacher, M. Three-Dimensional reconstruction of single particles from random and nonrandom tilt series. *Journal of Electron Microscopy Technique* **1988**, *9*, 359–394.
- [38] Sun, Y.; Xia, Y. Mechanistic Study on the Replacement Reaction between Silver Nanostructures and Chloroauric Acid in Aqueous Medium. *Journal of the American Chemical Society* **2004**, *126*, 3892–3901.
- [39] Wang, X.; Feng, J.; Bai, Y.; Zhang, Q.; Yin, Y. Synthesis, Properties, and Applications of Hollow Micro-/Nanostructures. *Chemical Reviews* **2016**, *116*, 10983–11060.
- [40] Xia, X.; Wang, Y.; Ruditskiy, A.; Xia, Y. 25th anniversary article: Galvanic replacement: A simple and versatile route to hollow nanostructures with tunable and well-controlled properties. *Advanced Materials* **2013**, *25*, 6313–6333.
- [41] Carlo, M. directions. At low T , in the present classical theory without randomness, S. *Science* **2014**, *343*, 1339–1343.
- [42] Lai, X.; Halpert, J. E.; Wang, D. Recent advances in micro-/nano-structured hollow spheres for energy applications: From simple to complex systems. *Energy and Environmental Science* **2012**, *5*, 5604–5618.
- [43] Chee, S. W.; Tan, S. F.; Baraissov, Z.; Bosman, M.; Mirsaidov, U. Direct observation of the nanoscale Kirkendall effect during galvanic replacement reactions. *Nature Communications* **2017**, *8*, 1–8.
- [44] Skrabalak, S. E.; Au, L.; Li, X.; Xia, Y. Facile synthesis of Ag nanocubes and Au nanocages. *Nature Protocols* **2007**, *2*, 2182–2190.

- [45] Sun, Y.; Mayers, B. T.; Xia, Y. Template-Engaged Replacement Reaction: A One-Step Approach to the Large-Scale Synthesis of Metal Nanostructures with Hollow Interiors. *Nano Letters* **2002**, *2*, 481–485.
- [46] Skriver, H. L.; Rosengaard, N. M. Surface energy and work function of elemental metals. *Physical Review B* **1992**, *46*, 7157–7168.
- [47] Fu, X.; Yuan, J. Non-destructive detection of cross-sectional strain and defect structure in an individual Ag five-fold twinned nanowire by 3D electron diffraction mapping. *Scientific Reports* **2017**, *7*, 1–12.
- [48] Sun, Y.; Ren, Y.; Liu, Y.; Wen, J.; Okasinski, J. S.; Miller, D. J. Ambient-stable tetragonal phase in silver nanostructures. *Nature Communications* **2012**, *3*, 6–11.
- [49] Sun, Y.; Wang, Y. Monitoring of galvanic replacement reaction between silver nanowires and H₂AuCl₄ by in situ transmission x-ray microscopy. *Nano Letters* **2011**, *11*, 4386–4392.
- [50] Sun, H.; Yesibolati, M. N.; Canepa, S. A.; Mølhave, K. Anisotropic Nanoscale Galvanic Replacement Reactions Studied by Liquid Cell Scanning Transmission Electron Microscopy. *Microscopy and Microanalysis* **2018**, *24*, 244–245.
- [51] Canepa, S. Quantifying Chemical and Electrochemical Reactions in Liquids by in situ Electron Microscopy. *Doctoral dissertation* **2017**,
- [52] TVIPS, EM-DFOM. <https://www.tvips.com/imaging-software/em-tools/em-dfom/>.
- [53] DREAM3D, <http://dream3d.bluequartz.net/>.
- [54] Glowinski, K.; Morawiec, A. Analysis of experimental grain boundary distributions based on boundary-space metrics. *Metallurgical and Materials Transactions A: Physical Metallurgy and Materials Science* **2014**, *45*, 3189–3194.
- [55] Glowinski, K.; Morawiec, A. A Toolbox for Geometric Grain Boundary Characterization. *Proceedings of the 1st International Conference on 3d Materials Science* **2016**, 119–124.
- [56] Brandon, D. The structure of high-angle grain boundaries. *Acta Metallurgica* **1966**, *14*, 1479–1484.

- [57] Wetegrove, M.; Witte, K.; Bodnar, W.; Pfahl, D. E.; Springer, A.; Schell, N.; Westphal, F.; Burkel, E. Formation of maghemite nanostructures in polyol: tuning the particle size via the precursor stoichiometry. *CrystEngComm* **2019**, *21*, 1956–1966.
- [58] Hugounenq, P.; Alloyeau, D.; Clarke, S. P.; Le, M.; Bazzi, R.; Brougham, D. F.; Wilhelm, C.; Gazeau, F. Cooperative Organization in Iron Oxide Multi-Core Nanoparticles Potentiates Their Efficiency as Heating Mediators and MRI Contrast Agents. **2012**, 10935–10949.
- [59] Dutz, S. Candidates for Biomedical Applications? *IEEE Transactions on Magnetics* **2016**, *52*, 1–3.
- [60] Kallumadil, M.; Tada, M.; Nakagawa, T.; Abe, M.; Southern, P.; Pankhurst, Q. A. Journal of Magnetism and Magnetic Materials Suitability of commercial colloids for magnetic hyperthermia. **2009**, *321*, 1509–1513.
- [61] Jeong, B. U.; Teng, X.; Wang, Y.; Yang, H.; Xia, Y. Superparamagnetic Colloids : Controlled Synthesis and Niche Applications **. **2007**, 33–60.
- [62] Bender, P. et al. Relating Magnetic Properties and High Hyperthermia Performance of Iron Oxide Nanoflowers. *Journal of Physical Chemistry C* **2018**, *122*, 3068–3077.
- [63] Gavián, H.; Sánchez, E. H.; Brollo, M. E.; Asín, L.; Moerner, K. K.; Frandsen, C.; Lázaro, F. J.; Serna, C. J.; Veintemillas-Verdaguer, S.; Morales, M. P.; Gutiérrez, L. Formation Mechanism of Maghemite Nanoflowers Synthesized by a Polyol-Mediated Process. *ACS Omega* **2017**, *2*, 7172–7184.
- [64] Gavián, H. et al. Colloidal Flower-Shaped Iron Oxide Nanoparticles: Synthesis Strategies and Coatings. *Particle and Particle Systems Characterization* **2017**, *34*, 1–12.
- [65] Weissleder, R.; Stark, D. D.; Engelstad, B. L.; Bacon, B. A.; White, D. L.; Jacobs, P.; Lewis, J. Superparamagnetic Pharmacokinetics Iron Oxide : and Toxicity. **1989**,
- [66] Zhang, T.; Zeng, Z.; Huang, H.; Hing, P.; Kilner, J. Effect of alumina addition on the electrical and mechanical properties of Ce_{0.8}Gd_{0.2}O_{2-δ} ceramics. *Materials Letters* **2002**, *57*, 124–129.
- [67] Bowman, W. J.; Zhu, J.; Sharma, R.; Crozier, P. A. Electrical conductivity and grain boundary composition of Gd-doped and Gd/Pr co-doped ceria. *Solid State Ionics* **2015**, *272*, 9–17.

- [68] Avila-Paredes, H. J.; Choi, K.; Chen, C. T.; Kim, S. Dopant-concentration dependence of grain-boundary conductivity in ceria: A space-charge analysis. *Journal of Materials Chemistry* **2009**, *19*, 4837–4842.
- [69] Gerhardt, R.; Nowick, A. S. Grain-Boundary Effect in Ceria Doped with Trivalent Cations: I, Electrical Measurements. *Journal of the American Ceramic Society* **1986**, *69*, 641–646.
- [70] Jasper, A.; Kilner, J. A.; McComb, D. W. TEM and impedance spectroscopy of doped ceria electrolytes. *Solid State Ionics* **2008**, *179*, 904–908.
- [71] Zhang, T. S.; Ma, J.; Cheng, H.; Chan, S. H. Ionic conductivity of high-purity Gd-doped ceria solid solutions. *Materials Research Bulletin* **2006**, *41*, 563–568.
- [72] Avila-Paredes, H. J.; Kim, S. The effect of segregated transition metal ions on the grain boundary resistivity of gadolinium doped ceria: Alteration of the space charge potential. *Solid State Ionics* **2006**, *177*, 3075–3080.
- [73] Christie, G. M.; Van Berkel, F. P. Microstructure - Ionic conductivity relationships in ceria-gadolinia electrolytes. *Solid State Ionics* **1996**, *83*, 17–27.
- [74] De Angelis, S.; Jørgensen, P. S.; Esposito, V.; Hsiao Rho Tsai, E.; Holler, M.; Kreka, K.; Abdellahi, E.; Bowen, J. R. Ex-situ tracking solid oxide cell electrode microstructural evolution in a redox cycle by high resolution ptychographic nanotomography. *Journal of Power Sources* **2017**, *360*, 520–527.
- [75] Zhi, M.; Lee, S.; Miller, N.; Menzler, N. H.; Wu, N. An intermediate-temperature solid oxide fuel cell with electrospun nanofiber cathode. *Energy and Environmental Science* **2012**, *5*, 7066–7071.
- [76] Zhao, E.; Jia, Z.; Zhao, L.; Xiong, Y.; Sun, C.; Brito, M. E. One dimensional La_{0.8}Sr_{0.2}Co_{0.2}Fe_{0.8}O_{3-δ}/Ce_{0.8}Gd_{0.2}O_{1.9} nanocomposite cathodes for intermediate temperature solid oxide fuel cells. *Journal of Power Sources* **2012**, *219*, 133–139.
- [77] Chou, C. C.; Huang, C. F.; Yeh, T. H. Characterization and catalytic activity of La_{0.6}Sr_{0.4}Co_{0.2}Fe_{0.8}O_{3-δ}-yttria stabilized zirconia electrospun nano-fiber as a cathode catalyst. *Ceramics International* **2013**, *39*, S549–S553, S549–S553.
- [78] Li, L.; Zhang, P.; Liu, R.; Guo, S. M. Preparation of fibrous Ni-coated-YSZ anodes for solid oxide fuel cells. *Journal of Power Sources* **2011**, *196*, 1242–1247.

- [79] Fan, L.; Xiong, Y.; Liu, L.; Wang, Y.; Kishimoto, H.; Yamaji, K.; Horita, T. Performance of Gd_{0.2}Ce_{0.8}O_{1.9} infiltrated La_{0.2}Sr_{0.8}TiO₃ nanofiber scaffolds as anodes for solid oxide fuel cells. *Journal of Power Sources* **2014**, *265*, 125–131.
- [80] Zhang, W. Electrospinning for solid oxide fuel cells. *Electrospinning for Advanced Energy and Environmental Applications* **2015**, 61–76.
- [81] Glowinski, K.; Morawiec, A. Analysis of experimental grain boundary distributions based on boundary-space metrics. *Metallurgical and Materials Transactions A: Physical Metallurgy and Materials Science* **2014**, *45*, 3189–3194.
- [82] Thermo Fisher Scientific, Inspect3D. <https://www.thermofisher.com/dk/en/home/electron-microscopy/products/software-em-3d-vis/inspect-3d-software.html>.
- [83] Thomsen, J. D. Measuring and Tailoring the Structure of Two-Dimensional Materials by Transmission Electron Microscopy. *Doctoral dissertation* **2017**,
- [84] Hammad Fawey, M.; Chakravadhanula, V. S. K.; Reddy, M. A.; Rongeat, C.; Scherer, T.; Hahn, H.; Fichtner, M.; Kübel, C. In situ TEM studies of micron-sized all-solid-state fluoride ion batteries: Preparation, prospects, and challenges. *Microscopy Research and Technique* **2016**, *79*, 615–624.
- [85] Protochips, FIB Sample Preparation. <http://www.protochips.com/wp-content/uploads/2017/10/prep-fib-samples.pdf>.

Appendix A

OMiTEM Reconstruction Manual

CONTENTS

1	Introduction	2
2	BF Reconstruction and Preparation	3
2.1	Converting Tvips Format	3
2.2	Tomographic Reconstruction of BF Data in Inspect3D	3
2.2.1	File Preparation	3
2.2.2	Reduce Data	4
2.2.3	Stack Alignment (find ω shift)	4
2.2.4	Tilt Axis Adjustment (find rotation center)	5
2.2.5	Reconstruct Volume	5
2.2.6	Inspect Stack	5
2.3	Create Mask (Avizo)	6
2.4	Create ω -shift file	6
3	OMiTEM Reconstruction	7
3.1	Tvips_convert	7
3.2	Drift Correction	8
3.2.1	Check Drift Correction	8
3.3	Adjust	8
3.4	Reconstruct	8
3.5	Advanced Reconstruction	8
4	Visualization and Statistics	10
4.1	Dream3d Pipelines	10
4.1.1	Step 1 - Import Data	10
4.1.2	Step 2 - Masking, Statistics on Unfiltered Data and IPF Coloring	10
4.1.3	Step 3 - Thresholding, Statistics and Exporting Slices	11
4.1.4	Meshing	13
4.1.5	GBPD	13
4.1.6	Combining Two Reconstructions	13
4.2	Visualize in Paraview	13
4.2.1	2D Visualization - Ortho slices	13
4.2.2	3D Visualization	14
4.3	Visualization in Avizo	14

4.4	Visualize GBPD with Mathematica	14
4.5	Create Mackenzie Plot	15
A	DREAM3d Pipeline Description	16
A.1	Step 1 - Import Data	16
A.2	Step 2 - Masking, Statistics on Unfiltered Data and IPF Coloring	16
A.3	Step 3 - Thresholding, Statistics and Exporting Slices	22
A.4	Meshing	25
A.5	GBPD	27
B	Programs, Scripts and Files	29
B.1	Software	29
B.2	Files	29
B.2.1	Example .txt files	29
B.2.2	Matlab scripts	29
B.2.3	Mathematica	30
B.2.4	Dream3D pipelines	30

Chapter 1

Introduction

This manual describes how to reconstruct Orientation Mapping in the TEM (OMiTEM) data.

The first chapter describes how to use bright field (BF) images to create a 3D BF tomographic reconstruction. The BF images show the morphology and is used to create a mask for the dark field (DF) images in the OMiTEM data.

The second chapter describes additional and supplementary parts to the original OMiTEM reconstruction manual (not developed in this project). This includes masking orientation maps with the BF data.

The third chapter describes how to use Dream3D pipelines to segment, smooth the data, create grain boundary plane distributions (GBPD) and data formats for visualization in Avizo or Paraview. Furthermore, it describes how to visualize 3D-OMiTEM data in Paraview, how to visualize GBPDs in Mathematica and how to create Mackenzie plots.

The appendix is divided into two parts. Part A is a description of the Dream3D pipelines and B shows a list of the used software and files for this manual.

Chapter 2

BF Reconstruction and Preparation

BF images are used to make a 3D tomographic reconstruction in order to create a mask for the outer shape of the OMiTEM data. Furthermore, the reconstruction process is used to find the ω -shift and rotation center necessary for the OMiTEM reconstruction. The reconstruction is done with Inspect3D and the binary mask is created with Avizo

2.1 Converting Tvips Format

To get the files for Inspect3D run the matlab script described in 3.1.

Then run the script GetAllBF. This creates one folder with the first BF image per omega tilt for the BF reconstruction. It also creates one folder per omega containing all BF images. This is later used to check the drift correction in step 3.2

2.2 Tomographic Reconstruction of BF Data in Inspect3D

2.2.1 File Preparation

- Open Inspect3D
- Click "Load" and choose all images. Make sure they are in the correct order.
- In "convert to bit depth" choose 16 bit
- In "convert to file type" choose MRC file
- Unfold "edit slice information". Click alpha tilt to mark column. In the slice information editor window insert base value (lowest tilt angle) and increment (tilt step). Then click "fill values". This will fill values in the alpha column with the correct tilt angles.

- Click "generate" in the file information window. This creates an .mrc file with the *omega*-tilt info.

2.2.2 Reduce Data

- Click "load" and choose the .mrc file created previously. Unfold "image manipulation" and click "invert image intensities".
- Go through images with the slider. If a bad image shows up (very dark or sample out of image), double right click and click "delete". This will "skip" the image. If you use this option you manually have to find the ω -shift manually and insert it in the ω -shift file.
- When satisfied with the stack of images, click "generate". This creates a new .mrc file with only the good images with inverted intensities.

2.2.3 Stack Alignment (find ω shift)

- Load the .mrc file from the reduce data step.
- Click "set up filter". Some good starting values are:
 - High pass radius 0.12 A High pass sigma 0
 - Low pass radius 0.4
 - Low pass sigma 0
 - Enable hanning window, tapering 0 (this reduces edge effects)
 - Optionally: 3x3 median filter. Sometimes it is better without
- Click "stack alignment"
 - Mark "use filter". This will use the filter you chose in the previous step.
 - Set max iterations to 3
 - set "Update tilt axis orientation period" to 1
- GPU alignment
 - Mark "use GPU for alignment shift calculation"
 - Mark "update tilt axis orientation manually"
- Click "generate". The program align slices and after 1 iteration it suggests a rotation axis angle.
- Rotation axis angle: For JEOL 2100 at Risø the rotation axis angle is 23°. Delete whatever the program suggests, write 23 and click "confirm".
- After 1 more iterations it asks about axis angle. Fill 0 and click confirm. Repeat this for 3rd iteration.
- When it is done click "save" under stack alignment. Save both .stf file and .txt file. This is used later.
- On the alignment data tab in the big window you can see shifts. Make sure the rotation axis is 23.

2.2.4 Tilt Axis Adjustment (find rotation center)

- Unfold "tilt axis adjustments"
- Load the aligned data set (if not already loaded).
- Mark "manual". (W)BP is optional. Do what gives the best image.
- To begin with set shift pixels to 5.
- On lower image hold CTRL and click on the image. This enables you to choose the projection plane visible at the top images. Do this for the upper and lower image. A good idea is to choose the highest plane where you still have sample or somewhere where you can see particles.
- Make the "banana" shapes disappear by clicking tilt axis shift or ω until the shapes disappear. When satisfied click "generate" and note the tilt axis. Do not change the tilt axis rotation or z-shift. write down the rotation shift in rotation center for later use.

2.2.5 Reconstruct Volume

- Click on the "reconstruct volume" tab.
- Load aligned images
- Mark "live view"
- In "reconstruction techniques"
 - mark "SIRT"
 - set iterations to 40
 - set detector settings: TEM CCD.
- In "reconstruct volumes setup" you can choose to crop the volume. Cropping the volume of interest can help reducing the computation time. However, if cropping is used remember to crop symmetrically. This is necessary since the OMiTEM reconstruction procedure crops from the center. Write down the xdim (width), ydim (thickness) and zdim (height) for use in the OMiTEM reconstruction to make the mask fit the reconstructed OMiTEM volume. After inserting the value, click on the small pencil to fill the value. Tip: remember to check that you have a big enough thickness to not crop part of your sample away.
- Click "generate"

2.2.6 Inspect Stack

Inspect stack (or go directly to Avizo)

- Load data and see if the data is satisfying.

2.3 Create Mask (Avizo)

- Open the .rec file created by inspect3D.
- Change axis: When you click on the green data module containing the data, a property window pops up. Click on the "Image crop editor" . click swap yz, click swap xy and then click "ok". This will change the axis to match the axis of the OMiTEM reconstruction. Optionally you can crop the volume symmetrically here. It needs to be symmetrically to fit with the OMiTEM output. Column 1 (x-axis) corresponds to the thickness in step 2.2.5.
- Shift to match rotation axis: In the "image crop editor" change the middle column (y-axis). Change the min index to the "rotation shift" you obtained in 2.2.4. Change the max index to max + rotation shift.
- right click on the green data module and type "interactive threshold" in the search field. Double click on the module and use it to set the threshold and get the binary mask.
- right click on the new label image and type "convert image type". Use the module and convert to 8 bit. Set "scale" to 255.
- Export the newly created binary data to 2D tiff. Click "file", "export data as" and choose 2D tiffs.

2.4 Create ω -shift file

Create an omega-shift file with the shifts found in step 2.2.3. An example of the omegashift file can be found in the folder with examples. The format should be:

```
# comment line
omega_1      alpha_1  beta_1  xshift_1  yshift_1
omega_2      alpha_2  beta_2  xshift_2  yshift_2
.            .        .        .        .
.            .        .        .        .
.            .        .        .        .
omega_n      alpha_n  beta_n  xshift_n  yshift_n
```

The xshift yshift are the last two columns in the .txt file created in inspect3d. Alpha and beta should be 0 since this is the omega shift file.

Chapter 3

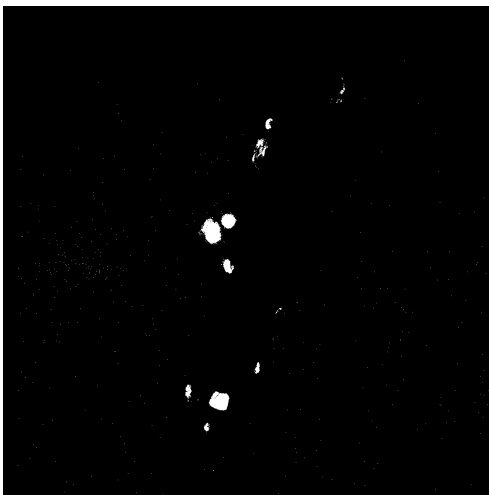
OMiTEM Reconstruction

This section will describe additional and supplementary steps not covered in the OMiTEM reconstruction manual (A).

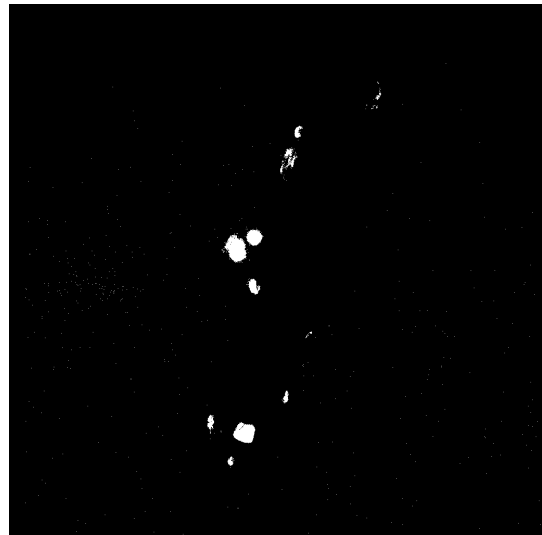
3.1 Tvips_convert

If the `tvips_convert` step fails or if you need to filter the data in the import process, conversion can be done using the Matlab script "`tvips_convert.m`".

Currently it is set up to use non-local means filtering. This helps reducing noise, making the binarization step easier. If you wish to change this, change line 366 and 367 in the `Tvips_convert_CQU_2.m`. The effect of the non-local means filtering is shown on figure 3.1.



(a) Binarized image without filtering.



(b) Binarized image after non-local means filtering.

Figure 3.1: Effect of non-local means filtering

3.2 Drift Correction

To use the shift files created in step 2.4, the drift correction step needs to be run differently than described in the manual (A).

Currently the `df_lattice.py` cannot start at any other value than zero. `Inspect3D` on the other hand often has a shift different than 0 to begin with. Therefore, run the `drift_measurement_beta.py` normally. Then run the `df_lattice.py` with an empty omega shift file. An example can be found in the folder with "examples" called `empty_omega_shift.txt`. Correct it to make the angles fit your measurement.

Now it is possible to combine the shift file created in 2.4 with the `df_shift.txt` using the matlab script "writeshift.m". The generated file should be the one used in the adjust step.

3.2.1 Check Drift Correction

To check the drift correction run the matlab script `drift_check.m`. This creates one folder per omega containing all the drift corrected BF images. Inspect the image stack in `imagej`.

3.3 Adjust

Use the `df_shift.txt` generated in step 3.2 for the alignment step.

Furthermore, to use the mask created in 2.3 make sure to have the correct values of `xdim` and `ydim` in the adjust step. `xdim` is the width in step 2.2.5 and `ydim` is the height in step 2.2.5.

3.4 Reconstruct

In the reconstruct step, the rotation center found in step 2.2.4 needs to be inserted in the config file. This is done by setting `x_c=(xdim/2)-rotationshift`. Where `rotationshift` is the shift found in step 2.2.4.

Furthermore, in this step `xdim` and `ydim` are not the same as in the adjust step. Ensure to set the following:

```
x_sample_dimension = width
y_sample_dimension = thickness
z_sample_dimension = height
```

3.5 Advanced Reconstruction

If it is difficult to binarize the images in the OMiTEM reconstruction, it can be an advantage to use two binarization levels. One very low (1 for all rings) for the inner part which is difficult to get the information from, and one which nicely shows the edges of the

object. If two reconstructions are made with two different binarization levels, they can later be combined using Dream3d as described in section (see section 4.1.6).

Chapter 4

Visualization and Statistics

To analyse and color the OMiTEM data Dream3D is used. Then, Avizo is used for visualization and to create animations. To use Dream3d, the data needs to be converted to .ANG data format. This is done with the matlab scrip OMiTEM2ANG.m. The converted data can be used directly in Dream3d.

4.1 Dream3d Pipelines

Use the pipelines in the Dream3d pipeline folder. These should be used in the correct order to work. Step 1, Step 2, Step 3 is used to segment, color, get statistics and create tifs for visualization. Meshing and GBPD are used to created a mesh and find the grain boundary plane distribution.

For information about what to input in the Dream3d modules refer to "Dream3d pipeline description" (Appendix A). A set of test files can be found in the folder OMiTEM Reconstruction -> testfiles. It also contains a result folder containing FeatureData csv files, GBPD files for mathematica and tiff files for visualization in Avizo.

The Dream3D pipeline folder consists of 3 pipeline for creating files for visualization and statistics and 2 pipelines for creating grain boundary plane distributions.

The purpose of each pipeline is described in the following.

4.1.1 Step 1 - Import Data

The first pipeline imports the data to h5ebsd format.

4.1.2 Step 2 - Masking, Statistics on Unfiltered Data and IPF Coloring

The second step pipeline masks the data with the mask created in step 2.3. Secondly it segments the data. Here you can type in the segmentation tolerance. This is currently set to 5. Finally it colors the grains in inverse pole figure colors (ipf) for cubic crystal structures. You can set the reference direction. Currently it is set to [100]. The pipeline

also creates a feature data csv file containing labeled grains and their individual feature properties. Currently the pipeline exports the following:

- Aspect ratio: Ratio of semi-axis lengths (b/a and c/a) for best-fit ellipsoid to Feature
- Axis euler angles: Euler angles (in radians) necessary to rotate the sample reference frame to the reference frame of the Feature, where the principal axes of the best-fit ellipsoid are (X, Y, Z)
- Axis lengths: Semi-axis lengths (a, b, c) for best-fit ellipsoid to Feature
- Centroids
- Equivalent diameters (in voxels)
- Number of voxels
- Number of neighbors
- Sphericity
- Surface area to volume ratio (voxels)
- Average euler angles per feature
- Average quats per feature

These parameters can be used for statistical information for e.g. size distribution. The data is not scaled. To get the correct volume or equivalent diameter you need to use the voxel or pixel size from the microscope image files.

4.1.3 Step 3 - Thresholding, Statistics and Exporting Slices

This pipeline filters out small grains segmented due to noise. This is done by thresholding by the axis lengths obtained in step 2. The effect of this is shown on figure 4.2.

The threshold can be set for each axis length. Currently they are all set to 5. This means that grains having a smaller axis length than 5 will be eroded. Finally the pipeline creates tiff files colored in ipf colors that can be visualized in Avizo. The pipeline also creates a feature data .csv file as in Step 2 but now for the filtered grains.

Tip: The axis length threshold can be found from a quick visualization in paraview (or other 3d visualization software) or by analysing the FeatureData exported in step 2.

Inspection in Paraview:

By opening the .xdmf file from step 2 in paraview it is possible to view the volume colored by the the axis lengths of the grain. This nicely visualizes what size the noise is (see figure 4.2). For visualisation in Paraview see section 4.2.

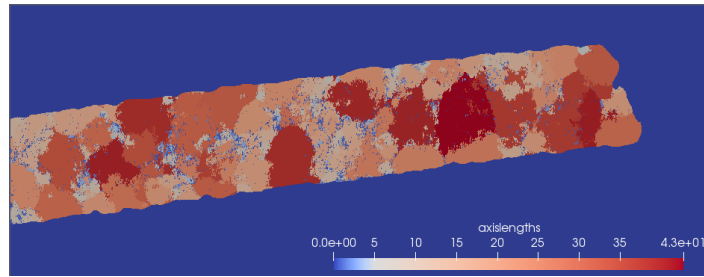
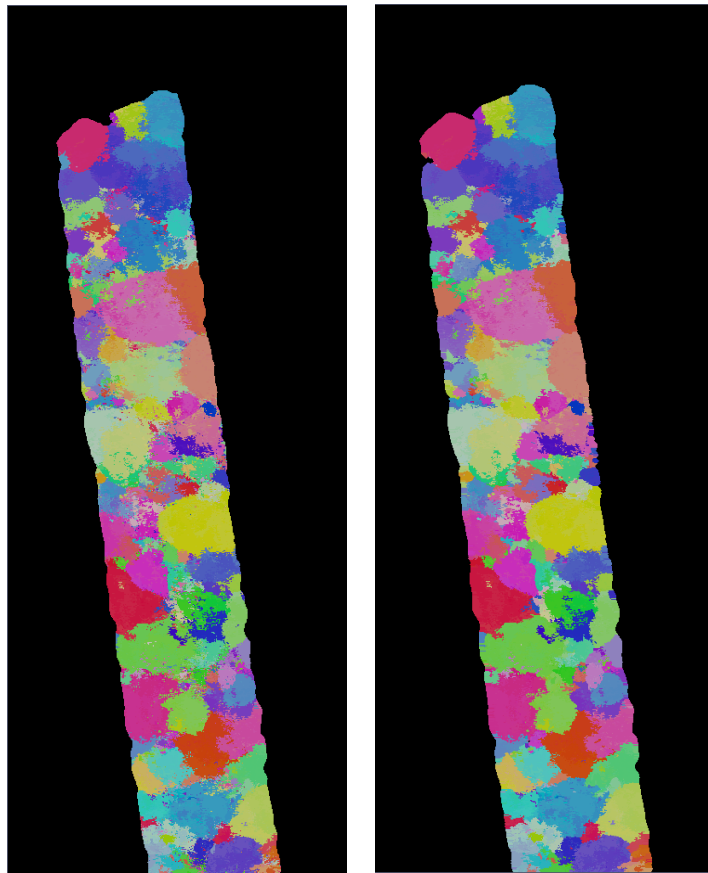


Figure 4.1: CGO fiber colored by axis length to estimate threshold.



(a) ipf color before thresholding (b) ipf color after thresholding
with axislengths=5

Figure 4.2: Reconstruction of CGO fiber.

Analysis of FeatureData:

In Step 2 the Feature data is exported. This includes a column containing the individual feature's axislengths. By creating a histogram the threshold can be determined from the big noise peak.

4.1.4 Meshing

The data is now ready for visualization in Avizo. This pipeline is for extra statistics or grain boundary plane distributions. This pipeline creates a mesh used for GBPD and GBCD.

4.1.5 GBPD

This pipeline creates GBPD and writes a .dat file. This file can be viewed with the Mathematica code "gbpd" described in section 4.4.

4.1.6 Combining Two Reconstructions

If you have made two reconstructions as described in section 3.5 you can combine them using DREAM3D.

Import the .ANG files using step1. Then use the Dream3d pipelines -> combined. After this you can use this file in step 2, 3 etc.

4.2 Visualize in Paraview

After Step2 and Step 3, Dream3d produces an xdmf file that can be used in paraview to inspect the result.

Open the .xdmf file in paraview. Choose Xdmf3 viewer. In "properties" (bottom left window) choose the Cell Arrays you want to see. Then click apply.

4.2.1 2D Visualization - Ortho slices

In the dropdown menu "coloring" where it says "solid color" choose the array you want to see (see figure 4.3). In the dropdown menu "representation" where it says "Outline" change to "slice". This will show you an ortho slice.



Figure 4.3: Icons in paraview

In "display" (lower left window) -> slicing choose the "slice direction" and use the slider "slice" to go through the slices (see figure 4.4).

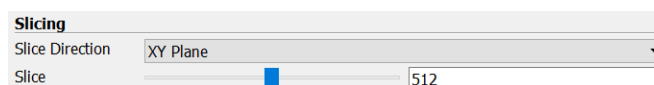


Figure 4.4

To match the view with the "slice direction" you can choose the view direction "set view direction to" +X,-X, +Y, -Y, +Z, -Z by clicking on one of the icons: 

4.2.2 3D Visualization

To view the result in 3D, in "properties" mark the cell array you want to see and the mask. Then click apply. To view the 3D volume click on the threshold icon . In scalars choose mask and set minimum to 1 and maximum to 1 (see figure 4.5). Click apply.

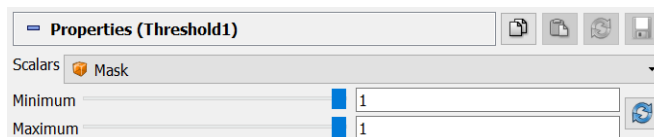


Figure 4.5

Then in "coloring" choose the Cell array you want to color by and change the representation to "surface".

A nice way to visualize is to use the IPF coloring. If you want to see the true IPF colors uncheck "Map scalars".

Now you can drag the object to see it in the direction you want to.

4.3 Visualization in Avizo

The IPF tif files created in step 3 (section 4.1.3) can be visualized in Avizo or other 3D visualization software. If Avizo is used, the data needs to be converted to .png files with transparent background. This can be done with the matlab scrip "transparent_ background.m".

In Avizo use "volren" to visualize the data not "volume rendering".

If not familiar with Avizo refer to the Avizo manual "Avizo how to_06092018.docx" created by Sina Baier located in the same folder as this manual.

4.4 Visualize GBPD with Mathematica

The mathematica script created by Krzysztof Glowinski (2015) can be used to visualize gbpd's written by Dream3D.

- Open mathematica script "plotGBPD.nd".
- Insert the path of the plotGBPD.nd in "path"
- Insert the data path in "datapath"
- Run cells. This should create the GBPD

4.5 Create Mackenzie Plot

A Mackenzie plot can be created with the matlab script mackenzie.m (package).

Appendix A

DREAM3d Pipeline Description

A.1 Step 1 - Import Data

This pipeline imports the data to h5ebbsd format.

Required objects to input:

Input directory

Output directory

Conversion parameters should be:

Z Spacing: 1

Stacking Order: low to high

Set Reference Frame: Default

In the Advanced File Name Options make the parameters fit to the input file name.

A.2 Step 2 - Masking, Statistics on Unfiltered Data and IPF Coloring

01 Import H5EBSD

This module is used to import the data. By reading only the necessary arrays memory problems are avoided.

Required objects to input:

EBSD HDF5 File: Choose the file created with step 1.

Euler representation: Degrees

In "Data arrays to read" mark:

- Confidence Index

- Phases

- Euler Angles

Name the Created objects as:

Data Container: ImageDataContainer1

Cell Data -> Cell Attribute matrix: CellData1

Cell Ensemble Data -> Cell Ensemble Attribute Matrix: CellEnsembleData1

In this manual the "Name the created objects" can be filled out as you want. However, to follow the manual use the suggested naming.

02 Create Ensemble Info

This module is used to create the information about the crystal structure. Required objects should be:

Crystal Structure: Choose crystal structure of sample (should normally be Cubic-High m-3m)

Phase type: Primary

Name: Write name of sample

03 ITK:: Import Images (3D Stack)

This module is used to import the mask.

Required objects should be:

Input Directory: Input the directory of the mask images created in 2.3.

File ordering: Ascending

Advanced File Name Options: make the parameters fit to the input mask image file names.

Origin: 000

resolution: 111

Name the created objects (example to follow manual):

Data Container: ImageDataContainer

Cell Attribute Matrix: Cell data

Image Data: ImageData

04 Convert Orientation Representation

Most Dream3D modules use quaternion representation. This module is used to generate an array with orientations in quaternion representation.

Inputs should be:

Input Orientation Type: Euler

Output Orientation Type: Quaternions

Input Orientations: Choose "EulerAngles" in the CellData1 container imported in 01.

Output Orientations: Quats

05 Threshold Objects

This module is used to create the binary mask from the mask images. Input:

Select Attribute Matrix: Choose the mask. (If the attributes are named as in this manual it should be: ImageDataContainer/CellData.)

Attribute arrays to threshold: ImageData > 0

Name the created objects:

Output Attribute array: Mask

06 Move Data

This module is used to move the mask to the Data Container with the OMiTEM data. It is necessary that they are in the same data container.

Input:

Object to move: Attribute array

Attribute array Source: ImageDataContainer/Celldata/Mask

Attribute matrix destination: ImageDataContainer1/Celldata1

07 Delete Data

To use as little memory as possible this module is used to remove the Data Container that contained the original mask data no longer needed.

Input:

Mark: ImageDataContainer

08 Isolate Largest Feature

This module selects the largest connected components as mask. The mask data can have edge effects from the reconstruction. If you have more than one object delete or suppress this module.

Input:

Cell data: Choose the mask. ImageDataContainer1/Celldata1/Mask

09 Segment Features (Misorientation)

This module is used to segment the data into features. This is necessary to get information about the individual grains.

Input:

Misorientation tolerance: Good starting value is 5.

Mark "use mask array".

Input the required arrays: Quats, Phases, Mask and Crystal structure

Name the created objects as:

Cell Feature id: FeatureIds

Cell Feature Attribute Matrix: CellFeatureData

Active: Active

10 Find Feature Phases

This module is used to create a feature phase array. Normally in OMiTEM there is only one phase. However, some modules require a feature phase array in some modules.

Input Phases and featureids.

Name the created object as:

Phases: ImageDataContainer1/CellFeatureData: phase

11 Find Feature Average Orientations

This module is used to find the average orientation of individual grains segmented in module 09.

Input required objects:

Element data in CellDataContainer1: FeatureIds, Phases, Quats

Ensemble data in ImageDataContainer/EnsembleAttributeMatrix: CrystalStructures

Name the created objects:

Average quaternions: ImageDataContainer1/CellFeatureData: avgquats

Average euler angles: ImageDataContainer1/CellFeatureData: avgeul

12 Find Feature Neighbors

This module produces information about neighbouring grains. This can be used for statistics or for other modules.

Parameters "Store Boundary Cells Array" and "Store Surface Feature Array" should be unchecked.

Input required objects:

FeatureIds: ImageDataContainer1/Celldata1/FeatureIds

Cell Feature Attribute Matrix: ImageDataContainer1/CellFeatureData

Created objects:

Number of neighbors: NumNeighbors

Neighbor list: NeighborList

Shared surface area list: SharedSurfaceAreaList

13 Find Feature Sizes

This module is used to generate geometric information about each grain.

"Save element size" should be unchecked

Input required objects:

FeatureIds: ImageDataContainer1Celldata1/FeatureIds

Cell Feature Attribute Matrix: ImageDataContainer1/CellFeatureData

Created objects:

Equivalent diameters: EquivalentDiameters

Number of Elements: NumElements

Volumes: Volumes

14 Find Feature Centroids

This module is used to generate geometric information about each grain. Input required objects: FeatureIds: ImageDataContainer1Celldata1/FeatureIds Created objects: Centroids: ImagedataContainer1/Celldata1/Centroids

15 Find Feature Shapes

This module is used to generate geometric information about each grain.

Input required objects:

FeatureIds: ImageDataContainer1Celldata1/FeatureIds

Cell Feature Attribute Matrix: ImageDataContainer1/CellFeatureData

Centroids: ImagedataContainer1/Celldata1/Centroids

Created objects:

Omega3s: Omega3s

Axis Lengths: AxisLengths

Axis Euler Angles: AxisEulerAngles

Aspect Ratios: AspectRatios

Volumes: Volumesshape

16 Find Surface Area to Volume Ratio & Sphericity

This module is used to generate geometric information about each grain.

Mark calculate sphericity.

Input required objects:

FeatureIds: ImageDataContainer1Celldata1/FeatureIds

Number of Elements: NumElements

Created objects:

Surface Area to Volume Ratio: SurfaceAreaVolumeRatio Sphericity: Sphericity

17 Export Feature Data as CSV file

This module exports the geometrical information of each grain.

Output File: Choose the output Directory and name

Uncheck Write Neighbor Data, mark Write Number of features line

Choose delimiter

Input required objects:

Feature Attribute Matrix: ImageDataContainer1/CellFeatureData

18 Generate IPF Colors

This module generate IPF colors for later visualization in Paraview. Reference direction 100

mark: "apply to good elements only"

Input required objects:

In ImageDataContainer1/CellData1 input: EulerAngles, Phases and Mask ImageDataContainer1/EnsembleAttributeMatrix/CrystalStructures

Created Objects:

IPF colors: IPF

19 Create Element Array from Feature Array

Feature array cannot be used for visualization in Paraview. Therefore this module creates an element array from a feature array. This enables visualization of number of elements in Paraview.

Input Required Objects: NumElements and FeatureIds

Copied attribute array: numelements

20 Create Element Array from Feature Array

Feature array cannot be used for visualization in Paraview. Therefore this module creates an element array from a feature array. This enables visualization of equivalent diameter in Paraview.

Input Required Objects: EquivalentDiameters and FeatureIds

Copied attribute array: EquivalentDiameters

21 Write Dream.3D Data file

This module is used to write a Dream3D file which can be used for the next pipeline. Furthermore, it creates an xdmf file which can be used with Paraview.

Choose output file name and directory
Mark "Write xdmf File"
Uncheck "Include Xdmf Time Markers"

A.3 Step 3 - Thresholding, Statistics and Exporting Slices

01 Read DREAM.3D Data File

Input the file and direction of the Dream3d file created by pipeline Step 2.

To avoid memory issues only import the following:

- CellData1
 - Confidence index
 - EulerAngles
 - FeatureIds
 - IPF
 - Mask
 - Quats
- CellFeatureData
 - Axislengths
 - NumNeighbors
 - avgeul
 - phase
- EnsembleAttributeMatrix
 - CrystalStructures

02 Create Element Array from Feature Array

This module is used to create an element array containing axislength. This is later used to filter small elements away.

Feature data to copy to element data: ImageDataContainer1/Celldata1/Axislength
Feature Ids: ImageDataContainer1/Celldata1/FeatureIds

Created Attribute Array: axislength

03 Split Multicomponent Attribute Array

This module is used to split the axis length into 3 components.

postfix: Component

Multicomponent Attribute Array: ImageDataContainer1/CellData1/axislength

04 Threshold Objects

This module is used to create a mask excluding small elements with an axislength smaller than the threshold. Currently it is set to 5.

Mask=1 axislengthComponent0>5

axislengthComponent1>5

axislengthComponent2>5

Output Attribute Array: Maskaxis.

05 Clear Data (Mask)

This module clears all voxels outside the mask. This can help with computation time. Furthermore, it defines the features with small axislength as being bad data.

Input the mask

Mask: ImageDataContainer1/CellData1/Maskaxis

06 Erode/Dilate Bad Data

This module erodes the bad data.

Operation: Erode

Number of iterations: 5

mark x direction, y direction and z direction.

Required objects.

Feature Ids: ImageDataContainer1/CellData1/FeatureIds

07 Clear Data (mask)

To retain the border everything outside the original mask is cleared.

Input the mask

Mask: ImageDataContainer1/CellData1/Mask

08 Find Feature Sizes

This module is used to find the sizes of each feature. This can later be exported to get statistics on the grains.

Save element sized should be unchecked

Input required objects:

FeatureIds: ImageDataContainer1Celldata1/FeatureIds

Cell Feature Attribute Matrix: ImageDataContainer1/CellFeatureData

Created objects:

Equivalent diameters: EquivalentDiameters1

Number of Elements: NumElements1

Volumes: Volumes1

09 Minimum Size

This module removes all features below 1 (since some were removed in the previous modules). The module can also be used to filter small elements away by inserting the minimum size.

Minimum allowed feature size: 1

Feature Ids: ImageDataContainer1Celldata1/FeatureIds

ImageDataContainer1Celldata1/NumElements

10 Minimum Number of Neighbors

This module removes all features that have less neighbors than the set threshold. It is currently set to 2.

Minimum allowed feature size: 2

Feature Ids: ImageDataContainer1Celldata1/FeatureIds

ImageDataContainer1Celldata1/NumElements

11 Export Feature Data as CSV

This module exports the geometrical information of each grain.

Output File: Choose the output Directory and name.

Uncheck Write Neighbor Data, mark Write Number of features line.

choose delimiter.

Input required objects:

Feature Attribute Matrix: ImageDataContainer1/CellFeatureData

12 Find Feature Neighbors

This module creates a NeighborList used to create a Mackenzie plot.

Input required objects:

FeatureIds: ImageDataContainer1Celldata1/FeatureIds

Cell Feature Attribute Matrix: ImageDataContainer1/CellFeatureData

Created objects:

Number of Neighbors: NumNeighbors1

Neighbor List: NeighborList

Shared Surface Area List: SharedSurfaceAreaList

13 Export Feature Data as CSV

This module exports NeighborList for creating Mackenzie plots.

Output File: Choose the output Directory and name.

Mark Write Neighbor Data, mark Write Number of features line.

Delimiter: Tab.

Input required objects:

Feature Attribute Matrix: ImageDataContainer1/CellFeatureData

14 Delete Data

This deletes unnecessary arrays to save memory.

Mark: Maskaxis, NumElements1, Volumes1

15 Write Dream3d Data File

This module is used to write a Dream3D file which can be used for the next pipeline. Furthermore, it creates an xdmf file which can be used with Paraview.

Choose output file name and directory

Check Write xdmf File

uncheck Include Xdmf Time Markers

16 Export Tiff Image Stack (ImageProcessing)

This module writes tif image slices with ipf coloring for visualization in Avizo.

plane: XY

Output file and direction: File name and directory of created tiffs.

Input Required objects:

ImageDataContainer1/CellData1/IPF

A.4 Meshing

The data is now ready for visualization in Avizo. This pipeline is for extra statistics or grain boundary plane distributions. This pipeline creates a mesh used for GBPD and

GBCD.

01 Read DREAM3D Data File

To avoid memory issues only the following needs to be imported:

CellData1:

EulerAngles

FeatureIds

CellFeatureData:

EquivalentDiameters1

NumElements1

phase

EnsembleAttributeMatrix:

CrystalStructures

02 Quick Surface Mesh

This module creates a mesh.

Input required objects:

feature ids

Created objects:

TriangleDataContainer

VertexData

NodeType

FaceData

FaceLabels

FaceFeatureData

03 Laplacian Smoothing

This module smooths the mesh.

Iteration steps: 100

Default lambda: 0,25

Triple line lambda: 0,2

Quadruple Points lambda: 0,15

Outer points lambda: 0

Outer triple line lambda: 0

outer Quadruple Points lambda: 0

Required objects: Node Type and Face Labels

04 Generate Triangle Areas

This module generates triangle areas which is used in the gbpd calculations.

Created objects:

TriangleDataContainer/FaceData/FacAreas

05 Generate Triangle Normals

This module generates triangle normals used in the gbpd calculations. Created objects:

TriangleDataContainer/FaceData/FaceNormals

06 Write Dream3D Data File

This module is used to write a Dream3D file which can be used for the next pipeline. Furthermore, it creates an xdmf file which can be used with Paraview.

Choose output file name and directory

Check Write xdmf File

uncheck Include Xdmf Time Markers

A.5 GBPD

This pipeline creates GBPD and writes a .dat file. This file can be view with the Mathematica code "gbpd".

01 Read DREAM.3D Data File

Input the file and direction of the Dream3d file created by pipeline Meshing.

02 Generate Triangle Face Ids

This module creates traingle face ids which is used in the gbpd calculation.

Input required objects:

TriangleDataContainer/FaceData/FaceLabels

Created Objects:

FaceLabels

FeatureFaceId1

FaceFeatureData1

FaceLabels1

NumTriangles1

03 Find GBPD (Metric-Based Approach)

This module calculates and exports the grain boundary plane distribution.

phase of interest: 1

Limiting distance: 5

Number of sampling points: 3000

Output directory and file names for gbpd files

Output directory and file names for error files

Appendix B

Programs, Scripts and Files

B.1 Software

- Inspect3D
- Avizo
- OMiTEM reconstruction software
- Dream3D
- (Mathematica)

B.2 Files

B.2.1 Example .txt files

- omega_shift_file.txt
- omega_shift_empty.txt
- Config.xml

B.2.2 Matlab scripts

- tvips_convert.m (package)
- writeshift.m
- OMiTEM2ANG.m
- transparent_background.m
- GetAllBF.m
- drift_check.m
- mackenzie.m (package)

B.2.3 Mathematica

- gbpd (package)

B.2.4 Dream3D pipelines

- step1.json
- step2.json
- step3.json
- meshing.json
- GBPD.json
- combined.json

Appendix B

OMiTEM Acquisition Manual

3D-OMiTEM Manual

Make sure you have a 400GB free on a hard-drive

Microscope settings:

- 1) Choose alpha 2 [L1: alpha selector] and spot 1-2 [L1: spotsize] (preferably 1 but use 2 if brightness is too high).
- 2) Find the sample.
- 3) Choose 25kx magnification.
- 4) Adjust eucentric height while tilting.
 - a) Set the current of the objective lens to the reference value by pressing [R1:STD FOCUS].
 - b) In the drop down menu click: Dialogue > operation > click on the stage tab. To tilt click +- X
 - c) Center the object of interest with the track ball. Tilt with 5 degree step in the desired tilt range. When tilting the object of interest moves. Adjust z with [R1:Z] to get object back in center for each step. For a desired scan from [-A:+A] Start at tilt 0 and go to -A (minimum), then to 0 and then to +A (max tilt).
- 5) Align beam at 0 tilt without adjusting eucentric height (Go through step 4)-11) in normal alignment manual)
- 6) Set up diffraction mode.
 - a) Insert SAD aperture
 - b) Press [R1: SA Diff] and adjust with [R1: Diff focus] to get the smallest spots.
 - c) Press [L1:PLA] and use [L1,R1:def] to center the diffraction pattern.
 - d) Insert objective aperture [L1:OB] and choose the smallest aperture [L1: disk buttons] or the manual objective aperture NO 3. Center the aperture using [L1:arrows].
- 7) Go to image mode by pressing [R1: Mag1], take the SAD out and center the objective aperture with [L1: arrows]. (tip: spread and then focus the beam to see if it is centered)
- 8) Go to normal software (EM-Menu) for image acquisition and adjust brightness to fit with acquisition with 1k Camera (remember to insert the 1k camera). This is very sensitive. Start with a very spread beam.
- 9) In EM-Menu In the toolbar choose "recorder options" (next to the red dot). If it is not there find it in view>toolbar>video recorder. Choose record>Unscaled images (16 bit)

Set up conical scanning.

- 10) Open software for conical scanning using the drop down menu: Applications > start EM tools (Use unscaled 16 bit) and create a new folder.

Check setup and calibrations

- 11) Before going any further it is necessary to check a couple of thing. Sometimes EM tools blanks some functions and it is necessary to restart the program
 - a) Go to Tomography -> Preferences. Click the Options tab. Check that the "correct stage when image shift exceeds limit of (%)" is not blank (see figure 1). It should be marked and the value should be set to 0.2-0.3 (depending on your TEM setup). This makes sure that if the image shift

becomes too high it will shift with the stage. This prevents shadowing from the objective aperture when the image shift is too high.

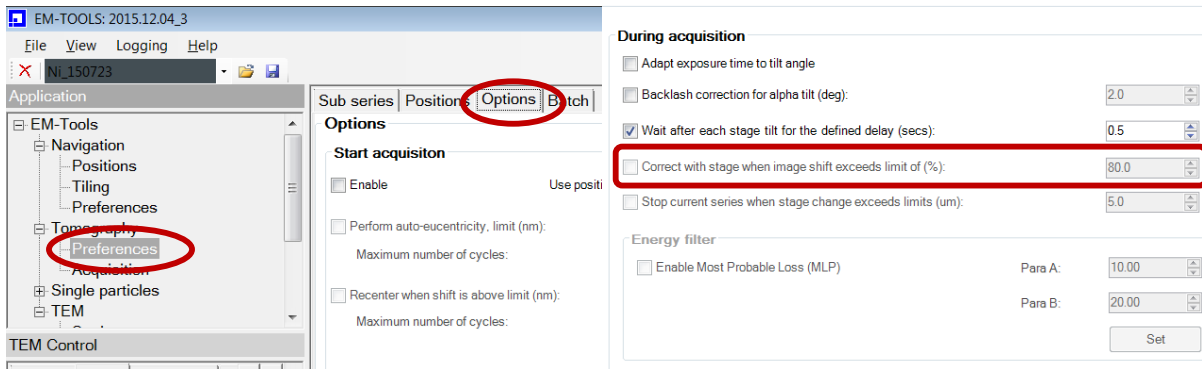


Fig 1: Blank "Correct with stage when image shift exceeds limit of (%)" restart EM-tools.

b) Check calibrations.

Go to TEM->Settings. This shows an overview of defined parameters and calibrations. It should contain a line at 25000x with green values.



This means that the system is calibrated at this magnification. If you need other magnifications it needs to be calibrated before. Ask the one in charge of the TEM.

c) If in a) the "correct with stage.." is blank or if there is no calibration restart EM-Menu and EM-Tools and create a new folder.

12) Set beam tilt angles.

- a) In the application window (to the left) click TEM-> scan generator and click on "DFOM acquisition" tab.
- b) Insert number of rings (6-10).
- c) Insert theta angles (mrad) in beam tilt angle for every ring (To convert from d-spacing to theta use $t(\text{mrad})=1000*2*\text{Arcsin}(\lambda/2d)$). Click in the table to change settings for each ring.
- d) Set positions to 180 and exposure time to 150.

13) Check DFOM calibration

a) Click on the DFOM calibration tab. Fill in all the values as in the figure 2.

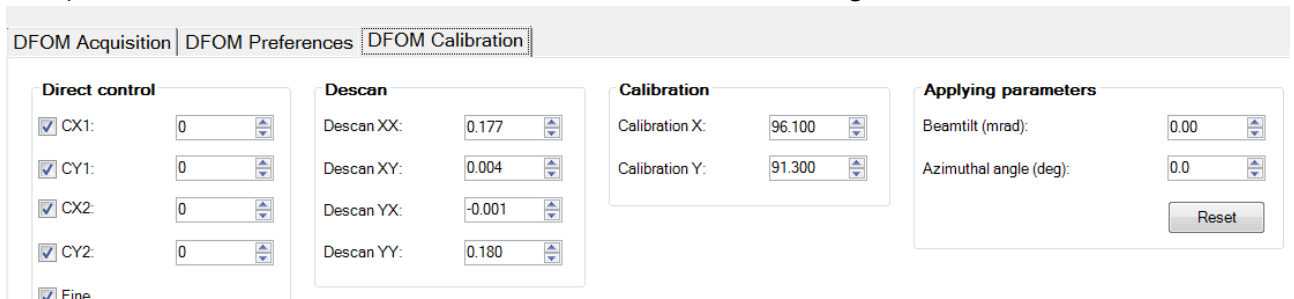


Fig 2: DFOM calibrations

14) **Test that all theta angles are correct.**

- a) Go to diffraction mode and insert the SAD.
- b) Click on the "DFOM calibration" tab.
- c) Insert the first beam tilt angle and press "Enter". The diffraction pattern should shift. Check that a new ring is at the center.
- d) Increase azimuthal angle. The diffraction pattern should rotate in a circle not in an ellipse. If this is not the case, contact the TEM responsible to correct the calibration.
- e) Repeat this for all beam tilt angles to check the beam tilt calibration.
- f) Take SAD out and go to image mode.

15) **Adjustments (center aperture and set autofocus).**

- a) Go to navigation > positions > and click on the focus tab. Click get TEM > PC. In the camera control menu click expose > choose 1k Camera and an exposure of 150-200ms (repeat for tracking and exposure).
- b) In TEM > scan generator > DFOM preferences insert the values as shown on figure 3. After inserting the numbers, click "Center" in "centering objective aperture with offset beamtilt" to center the beam. Do this 3 times (or until the "last change" is small and the aperture looks centered). The mean value at the camera control window would not change much.

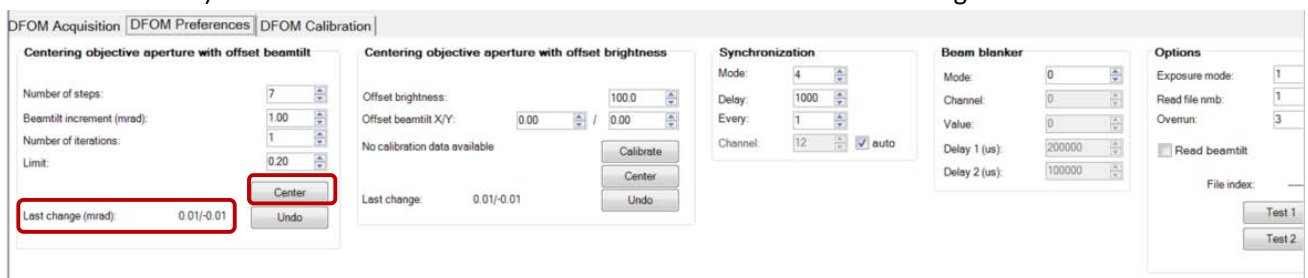


Fig 3: DFOM preferences and centering of objective aperture.

- c) Go to navigation > positions > and click on the focus tab. Click autofocus > correct Repeat 3 times or until last change is under 200.

16) **Start acquisition.**

- a) Set the tilt angles. Go to Tomography > preference > sub series. In number of sub series start at 1. To change settings for second and third subseries click on + or -. The setting for scan from [-A:+A] are described in the following:
 - Subseries 1 makes sure that we go to -A. In this step no images are recorded. Choose linear mode and insert omega angles as:
 - o start: 0
 - o end: -A
 - o incr: 2
 - o select "skip multiple focusing and drift check" and "skip exposure position."
 - Subseries 2 is where BF and DF images are recorded. Choose linear mode and set omega angles as:
 - o start: -A

- end: +A
 - incr: step size
 - unselect all options and choose Tiff as file format.
 - Subseries 3 makes sure the goniometer return to 0. No images are recorded. You can also manually stop this step. Choose linear mode and set:
 - Start: +A
 - End: 0
 - Incr: 2
 - Select all options.
- b) Go to Positions > focus 1. Check the options. They should be as in figure 4. Click on the + or - button to enable editing of tracking or exposure. Check the options. They should be as in figure 4.

Preferences Tracking

Options

Apply on first position only

Take new image after tracking

Additional focus and drift check

Enable and repeat focussing until:

Focus change below (nm): 500

Enable drift check

Drift rate below (nm/min): 20.0

Delay (s): 0.0

Maximal time (s): 30

Break condition

Enable Limit (%): 20.0

Focus change (nm): 30000

Beam centering

Enable Delay (min): 10.0

Max. tilt angle (deg): 45.0

Shift beam

Use TEM Beam Centering

Camera format: F114TR 1k

Exp time (ms): 500.0

Obj-Aperture centering

Enable Delay (min): 0.0

Dynamic focussing in STEM

Enable

Preferences Focus

Focus mode

Repeat focussing until:

Focus change below (nm): 400

Maximum iterations: 4

Break condition

Focus change (nm): 30000

Enable Limit (%): 20.0

Beam centering

Enable Delay (min): 10.0

Max. tilt angle (deg): 45.0

Shift beam

Use TEM Beam Centering

Camera format: F114TR 1k

Exp time (ms): 500.0

Preferences Exposure

Options

Tracking after exposure

Store addition small format (256 x 256)

Beam centering

Enable Delay (min): 10.0

Max. tilt angle (deg): 45.0

Shift beam

Use TEM Beam Centering

Camera format: F114TR 1k

Exp time (ms): 500.0

Special series

None Focus/dose

Tiling Beamtilt

Beamtilt series

Mode: Recorder

Number of radi: 8

#	BT	Nmb	Time	Central
1	12.34	180	150	no
2	14.25	180	150	no
3	20.15	180	150	no

Beam tilt angle (mrad): 12.3

Number of positions per angle: 180

Exposure time (ms): 150

Skip central position: no

Center objective aperture

Fig 4: preferences for focus, tracking and exposure.

- c) Go to Preferences > Batch (mark the box). Make sure exposure is 150-200 ms. And defocus=0
- d) To start the test go to Tomography > acquisition > start. See that grains light up and that sample tilts in normal acquisition software.

Appendix C

Manuscript 1

3D Ion Percolation Path in Gadolinium Doped Ceria Nanofibres for Solid Oxide Electrochemical Cells

Sofie Colding-Jørgensen^{1*}, Søren B. Simonsen¹, Peter S. Jørgensen¹,
Wenjing Zhang^{1,†}, Xiaoxu Huang², Søren Schmidt³, Luise Theil Kuhn^{1*}

¹DTU Energy , Technical University of Denmark
Fysikvej building 310, 2800 Kgs. Lyngby, Denmark

²DTU Mechanical Engineering, Technical University of Denmark
Nils Koppels Allé building 404, 2800 Kgs. Lyngby, Denmark

³DTU Physics, Technical University of Denmark
Fysikvej building 307, 2800 Kgs. Lyngby, Denmark

*To whom correspondence should be addressed; sofcol@dtu.dk, luku@dtu.dk.

†Present address: DTU Environment, Technical University of Denmark,
Bygningstorvet bygning 115, 2800 Kgs. Lyngby, Denmark

Understanding transport properties in ion conductive solids is key to supporting the development of devices for energy conversion, e.g., solid oxide electrochemical cells. Because of the complex nanostructured nature of such materials they have numerous types of grain boundaries and the prediction of the percolation path becomes challenging. We employ, for the first time, a combination of 3D-Orientation Mapping in the Transmission Electron Microscope and Energy Filtered Transmission Electron Microscopy to map crystal orientation and doping concentration with nm-precision to predict 3D-ion percolation paths in state-of-the-art electrospun ($\text{Ce}_{0.9}\text{Gd}_{0.1}\text{O}_{1.95}$) nanofibres. The re-

sults show that the conductivity of CGO nanofibres are affected by grain- and diameter size. Furthermore, we show that 3D-OMiTEM is a powerful non-destructive tool for determining 3D-ion percolation paths with nm-precision of complex nanostructures.

An increasing interest in the use of renewable energy sources emphasizes the need for high performance energy conversion devices. Examples of such devices include, but are not restricted to, Solid Oxide Electrolysis Cells (SOECs) and Fuel Cells (SOFCs). These give an opportunity to exploit fluctuating energy sources. Electrical energy can be harvested by using SOECs during overproduction periods from solar- or wind energy, and utilized in underproduction periods by SOFCs (1).

Solid Oxide Cells (SOC) are composed of electronic-, ionic- and mixed conductors and high conductivity is an important property for optimal performance. To develop and optimize such devices it is critical to understand the charge transport properties in ion conductive solids (2, 3).

The ionic and electronic conductivity of functional materials, used in SOCs, are closely related to the nano- and micro-granular structure since they contain a large fraction of grain boundaries (GB) (2–9). It is widely accepted that the conductivity in the interior of the grains are orders of magnitude larger than at the GB and as a result, the GBs often become the limiting factor for obtaining a higher conductivity (4–9). The conductivity in the GB is determined by equation 1 (3, 4).

$$\sigma_{GB} = \beta_{GB} \frac{n_v^{GB}}{T} \exp\left(\frac{-E^{GB}}{kT}\right), \quad (1)$$

where σ_{GB} is the grain boundary conductivity, β_{GB} is the pre-exponential conductivity, which is independent of the doping-concentration, n_v^{GB} is the effective GB carrier concentration i.e. the average concentration of oxygen vacancies in a GB, k is the Boltzmann factor, T is the temperature and E^{GB} is the GB activation energy.

The pre-exponential factor has been widely studied (10–17). However, the activation energy is difficult to determine as it depends on the composition of the individual grain boundary. The complex nano-structured nature of the materials generate a variety of possible GB-types with different atomic structure and composition. This makes it challenging to fully understand the fundamentals and parameters affecting the overall performance.

A recent study by Bowman et al. (2020) has gathered literature (11–17) on the field to determine the activation energy as a function of grain boundary doping concentration for gadolinium doped ceria (CGO). By fitting the data empirically they determined the relationship in equation 2 (3),

$$E^{GB} = 2 \cdot 10^{-4} \left([A^{3+}]_{GB} \right)^{-5} + 0.91 \quad (2)$$

where $[A^{3+}]_{GB}$ is the trivalent doping concentration.

The study by Bowman et al. (2020) furthermore suggests a linear relationship between the crystalline misorientation angle of two neighbouring grains and the GB doping concentration (3). This gives the opportunity to determine the local GB doping concentration, and thereby the GB- activation energy and conductivity, directly from a crystal orientation map. Hence, a crystal orientation map will be able to predict possible ion percolation paths, which could help determine the overall conductivity of the sample.

The overall conductivity can be affected by cracks or other structural changes (18). Therefore, the 3D-ion percolation path would be a valuable contribution to understanding the fundamentals of ion conductive solids. Hence, in order to better understand the conductivity of materials for SOCs, it is essential to study their nanoscale crystal orientation on grain level in 3D.

We propose 3D-Orientation Mapping in the Transmission Electron Microscope (3D-OMiTEM) as a promising technique for non-destructive visualization of crystal orientation in 3D. Liu et al. first described the method applied on a simulated data set and on an aluminium thin foil

in 2011 (19). More recently Wu et al. (2020) has described the method applied on a gold nano-island film (20).

We demonstrate that with this technique it is possible to obtain 3D orientation information of arbitrarily oriented crystals with complex structure and composition using TEM. Although it is still a challenge we show that maps can be obtained and reconstructed in a few days making this a feasible tool for electron microscopists.

We employ a combination of Energy Filtered Transmission Electron Microscopy (EFTEM) and OMiTEM to find the linear relationship between the doping concentration and the crystal orientation. We present the first demonstration of how a 3D-Orientation map, generated by 3D-OMiTEM, in combination with the linear relationship can be used to calculate 3D ion percolation paths with lowest resistivity. This work will contribute to the understanding of how the numerous possible GB-types, with different atomic structure and composition, affect the overall conductivity in the material.

We employ 3D-OMiTEM on a functional material, namely the state of the art SOC material electro-spun Gadolinium doped Cerium Oxide (CGO) nano fibres. These electrospun nanofibres have recently shown potential to be an efficient and cost effective alternative for materials for SOCs. The fibres can form electrodes with high porosity, high pore connectivity and form continuous electron- and ion conducting paths (21–26).

We show the first demonstration of the possibilities of 3D-OMiTEM on complex nano structured oxide electrospun fibres. This includes the first 3D-orientation map on nm-scale of an electrospun nano fibre, as well as the analysis of this map, in order to predict and visualize the first ion percolation path in 3D on nm scale. With this powerful tool we thereby come a step closer to understanding and describing the fundamentals of grain boundaries and grain boundary planes in state-of-the-art electrode materials for SOCs.

3D-OMiTEM During the 3D-OMiTEM acquisition we choose a specific Bragg reflection and form a dark field (DF) image where the contrast in the projection only comes from the part of the sample that obey the specific diffraction condition (see figure 1b). The DF image is recorded by inserting an objective aperture in the diffraction plane. Depending on what diffraction spot is chosen only grains with this specific orientation will contribute to the contrast in the image. Each image thus constitutes a 2D-projection of the 3D grain shapes observed for a point in the reciprocal space. This is done for beam tilts along the selected ring, 360° with a 2° step. Each of the 5 inner rings in the diffraction pattern was used for every sample rotation angle. For aligning the direct space information bright field (BF) images are recorded by setting the beam tilt to 0 (direct beam) as shown on figure 1a. The result is ~ 70.000 images that are reconstructed into a 3D grain orientation map.

3D-OMiTEM was applied on CGO electrospun nano fibres calcined at 800°C for 1 hour and for 10 hours, respectively, in atmospheric air.

Figure 1a shows a BF image of an electrospun CGO nano fibre with a diameter of approximately 200 nm. The BF image shows that the fibre morphology is dense and consists of multiple grains. However, the individual grains are difficult to distinguish which makes it hard to estimate a grain size distribution.

Individual grains can be identified on the corresponding DF image in figure 1b. By browsing through the DF images, recorded by choosing different diffraction spots, different grains light up. This reveals that the fibre is a polycrystalline sample with multiple grains with different crystal orientations.

The DF images are used to determine the crystal orientations as their acquisition parameters carry the corresponding reciprocal space information. The orientation reconstruction is done on threshold aligned DF images. An example is shown on figure 1c.

Using in-house developed software, grains are reconstructed resulting in a multi-dimensional data set with x,y,z coordinates, each with a confidence index and crystal orientation. The results are shown on figure 1d and 1e.

Since BF images contain more accurate information about the overall morphology of the fibres, BF tomograms were reconstructed in Inspect3D (27) and used to mask the outer boundary of the fibres in the final orientation map.



Figure 1: a and b are TEM images of CGO fibre calcined at 800°C for 1 hour. a BF image, b one of hundreds of thousands of DF images used for reconstruction. c binarized image of b used for reconstruction. a,b and c images are scaled to have the same size with scale bar as shown in a. d and e are orientation maps of an electrospun CGO fibre calcined at 800°C: d calcined for 1 hour, e calcined for 10 hours. The colors are inverse pole figure (IPF) coloring showing crystal directions.

The orientation maps produced by 3D-OMiTEM are presented in figure 1d,1e and show the electrospun fibres in 3D with grains coloured by their crystal orientation in inverse pole figure (IPF) color. The individual grains are defined as well as the overall morphological structure of the fibre. This enables extraction of geometric and orientation parameters of all individual grains for statistical analysis as well as for orientation analysis. To our knowledge this is the first time this type of 3D analysis has been conducted on electrospun nano fibres.

The 3D orientation map enables analysis and characterization of both the grains and grain

boundaries. To characterize the grains, the 3D structure is segmented by grouping voxels with a misorientation smaller than a set tolerance and defining them as one grain.

Each grain is compared to its neighbour and a histogram of the misorientation between neighbouring grains is plotted. The misorientation distribution on figure 2b and 2f showed no texture in the two fibres since it follows the Mackenzie distribution for randomly oriented cubic crystals (solid line in figure 2b and 2f).

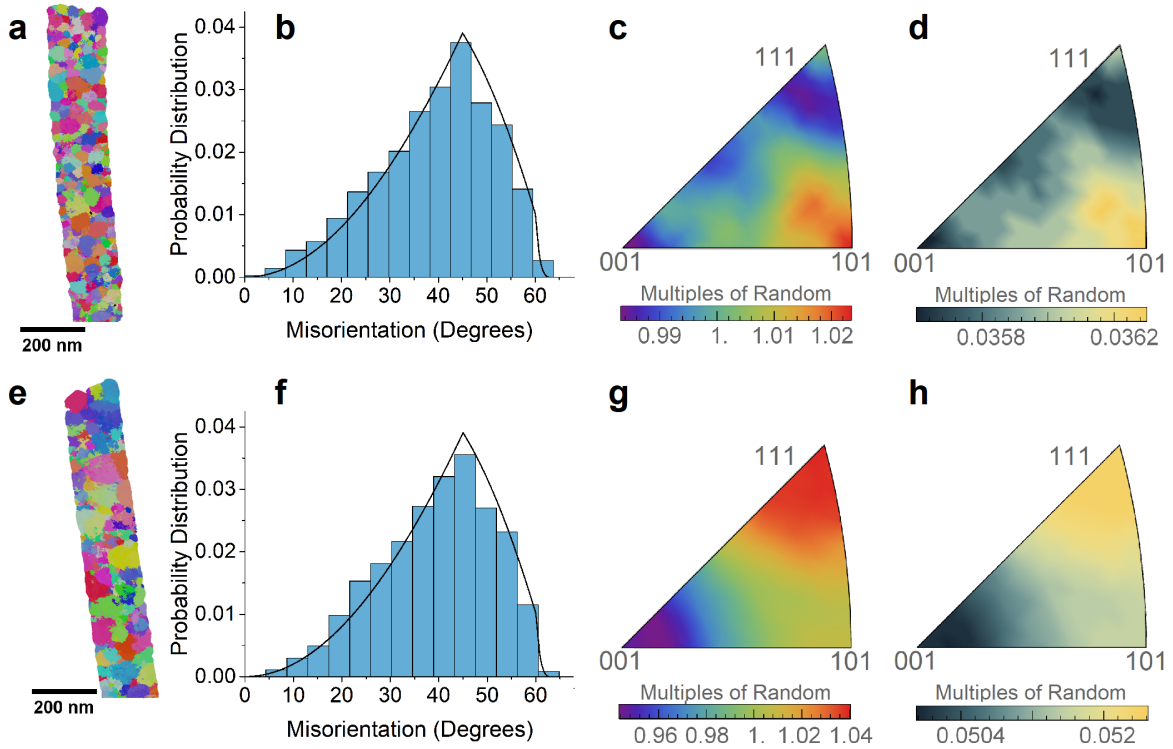


Figure 2: Orientation analysis: a, b, c and d are the results from a CGO nanofibre calcined at 800°C for 1 hour, e, f, g and h for a CGO nanofibre calcined at 800°C for 10 hours. a, e shows an ortho slice through the middle of the sample in IPF colors as figure 1. b and f show the misorientation probability distribution. The solid line is the theoretical mackenzie distribution for randomly oriented crystals. c, g show the grain boundary plane distribution (GBPD) with multiples of random scale. d, h is the error distribution of the GBPD in a and c, respectively, in absolute values. GBPDs are plotted using a mathematica script described in (28).

This finding is supported by the analysis of the grain boundary plane distribution (GBPD).

The GBPD in figure 2c and 2g is mapped using a metric based approach explained in (29), plotted using a mathematica script described in (28) and calculated using Dream3D (30). The GBPD of the two electro-spun fibres shown on figure 2 describes the measured area of grain boundary planes normalized with respect to a random isotropic distribution (28). The unit is thus multiples of random distribution. The maxima in the GBPD is 1.03 for the CGO nanofibre calcined for 1 hour (figure 2c) and 1.04 (figure 2g) for a CGO nanofibre calcined for 10 hours and lies within the statistical error of uncertainty (figure 2d, 2h). Therefore, the grain boundary plane distribution shows a random isotropic distribution for both samples and the two samples are indistinguishable with regards to the crystal orientation.

Both orientation analyses thereby show that grains in both fibres have a random isotropic distribution.

The grain size distribution was calculated from the 3D orientation map. From the number of voxels in a grain, a corresponding sphere was computed and the equivalent diameter was calculated for each grain.

The grain size distributions on figure 3 follow a log normal distribution with no significant noise peaks and reveal, as oppose to the orientation analysis, a clear difference for the two fibres. From the fits, the equivalent mean diameters can be calculated. The sample calcined for 1 hour has a mean diameter of 29.9 ± 0.9 nm and after 10 hours it increased to 35.3 ± 1.6 nm i.e. a 18% increase.

From the orientation- and structural analysis it is obvious that we can extract overall information from the sample not only on one slice of material but the whole sample in one measurement. This gives us good statistics as well as local information of the entire sample providing new possibilities of extracting information and understanding fundamentals of nano-structured materials. In the following we demonstrate, for the first time, some of the possibilities of 3D orientation map generated by 3D-OMiTEM.

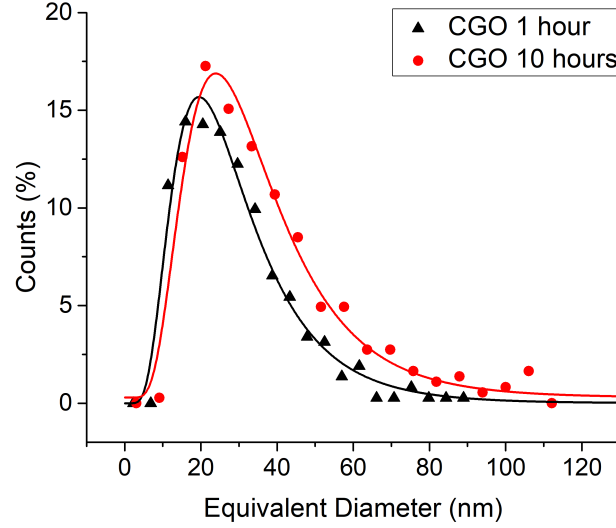


Figure 3: The grain size distribution found using OMiTEM. Black is the size distribution of CGO calcined at 800°C for 1 hour in atmospheric air. Red is the result for the sample calcined for 10 hour in atmospheric air. The solid lines show lognormal distribution fits.

The misorientation of grains can be used to find the local GB doping concentration, as in (3). To find the relationship between the misorientation and the doping concentration, EFTEM atomic ratio mapping as described in (31, 32) was acquired (figure 4a) followed by OMiTEM (figure 4b) of the same flat area (for further information see supporting info section S5 and Fig S3 and Fig S4).

The result is shown of figure 4c and the linear relationship, in equation 3, was determined from the fit in well agreement with Bowman et al. (2020) (3).

$$[A^{+3}] = 8 \cdot 10^{-2} + 4 \cdot 10^{-3} \cdot m \quad (3)$$

In equation 3, m denotes the crystallographic misorientation angle of neighbouring grains. The EFTEM result furthermore revealed that at the surface the gadolinium content was the same as that of a grain boundary with approximately 62° misorientation, which is the highest for a cubic structure.

From the local doping concentration, the activation energy and thereby the resistivity can

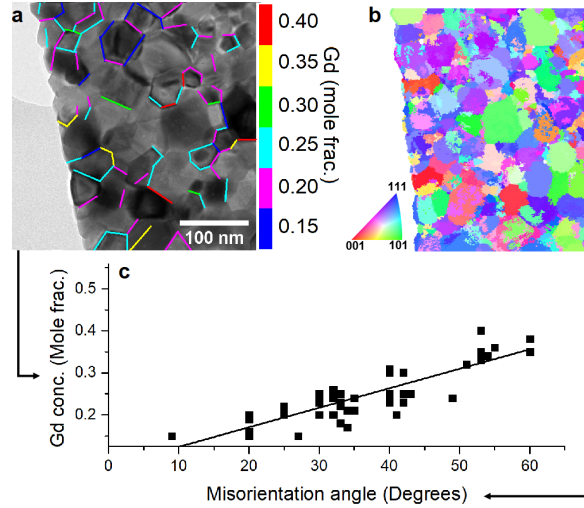


Figure 4: Relationship between grain boundary doping concentration and misorientation angle of neighbouring grains. a shows the result of the EFTEM atomic ratio mapping where the results of the gadolinium ratio are overlaid a BF image. b is the corresponding orientation map and c is the graph correlating the grain boundary doping concentration with the misorientation angle of neighbouring grains

be mapped using equation 1, 2 and 3. A slice through the middle of the calculated resistivity map, is shown on figure 5c and 5d. Here the grain interior has been assigned with the value of $\rho = 1 \cdot 10^3 \Omega \text{ cm}$ as in (4) at 440°C .

A possible ion percolation path is obtained by locating the path with the lowest resistivity in the fibre. This is done by distributing starting points evenly at the end of the fibre. Furthermore, the surface resistivity was set to have the value as at a grain boundary with 62° misorientation. The obtained percolation path is presented in figure 5a and 5b.

Figure 5a and 5b, to our knowledge, demonstrates for the first time the percolation path at such high resolution in 3D. With the 3D information it is possible to determine the percolation path with minimum resistance. This is done for the entire 3D structure and not just for a 2D slice.

To predict the relation between conductivity and fibre diameter, we virtually shrink the

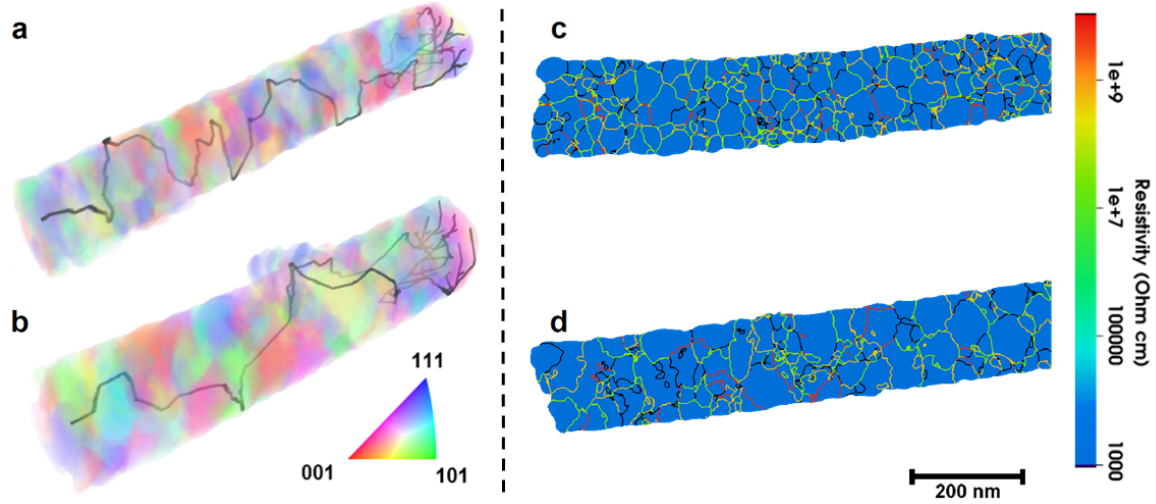


Figure 5: Visualization of percolation path and resistivity. a and c show the structure of a CGO nanofibre calcined at 800°C for 1 hour, b and d is the structure of a CGO nanofibre calcined at 800°C for 10 hour. a and b is the 3D visualization including the percolation path. The black path represents the ion percolation path with the smallest resistance. The colors are IPF colors visualizing different orientations. c and d shows a slice through the middle of the sample revealing the calculated resistivity at 440°C . The grain interior has been assign with the value of $\rho=1\text{E}3 \Omega \text{ cm}$. The colors represent the resistivity in the structure.

nanofibre diameters. The results on figure 6 show how the effective resistivity of the percolation path increases as the fibre becomes smaller, with a more rapid increase as the fibre diameter approaches zero. This is a consequence of the fibre containing fewer grains and grain boundaries as its diameter diminishes, leading to an increased probability of the percolation path having to cross a grain boundary with high resistance or having to travel on the surface. The onset of the more rapid increase in resistivity can be seen to occur at small fibre diameters ($< 20 \text{ nm}$). This corresponds roughly to when we would expect the fibre cross section to only contain a single grain. With no alternatives for less resistive grain boundaries the percolation path must pass the present grain boundary even at a high resistance i.e. the rapid increase corresponds to a change from few alternative grain boundaries to no alternative grain boundaries.

The percolation path in the CGO fibre calcined for 10 hours is seen to have a significantly

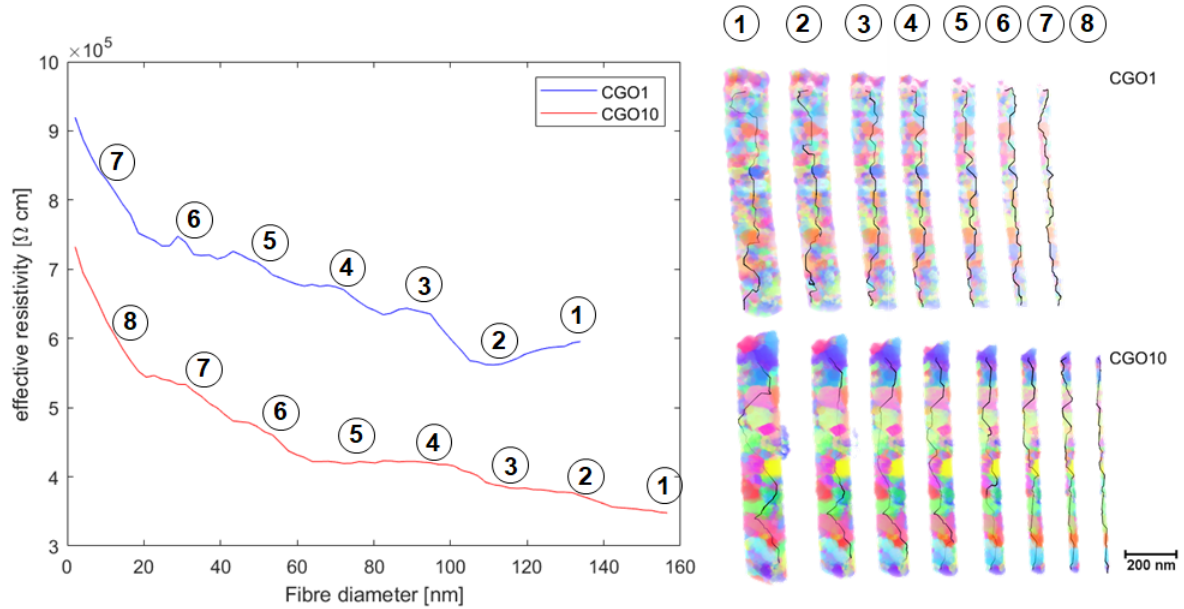


Figure 6: Left: Percolation path resistivity as a function of fibre diameter at the narrowest point on the fibre for the CGO calcined for 1 hour and CGO calcined for 10 hours. The largest plotted fibre diameter corresponds to the unaltered fibre before erosion. Right: 3D reconstruction of eroded CGO fibre calcined for 1 hour and 10 hours. Numbers indicate the position on the graph.

lower effective resistivity than the CGO fibre calcined for 1 hour ($3.49 \cdot 10^5 \Omega \cdot \text{cm}$ vs. $6.06 \cdot 10^5 \Omega \cdot \text{cm}$). The main contribution to the resistance in the percolation path comes from crossing grain boundaries rather than the bulk CGO resistivity. The increased effective resistivity in the CGO fibre calcined for 1 hour can thus be explained by the smaller grain size, leading to an additional number of grain boundaries to be crossed in the percolation path.

Our study reveals that 3D-OMiTEM is a feasible tool to visualize crystal orientation in polycrystalline nanofibres in 3D non-destructively. The results showed that CGO1 and CGO10 are indistinguishable with regards to the global crystal orientation distribution and only the grain size separates them. From this, and the calculations of the resistivity we conclude that the conductivity of the nanofibres are both affected by the grain size and the fibre diameter.

The work offers an insight into the possibilities of 3D-OMiTEM. 3D-OMiTEM can be used

to gain 3D orientation information locally on the entire sample enabling orientation- and structural analysis which ultimately can predict possible ion percolation paths. This can prove to be a strong tool to understand the fundamentals of grain boundaries in solid oxide cells and a step closer to understanding pathways in polycrystalline solids to support the development and optimization of devices for energy conversion.

Acknowledgments

The authors thank Peter A. Crozier for the fruitful discussions and Rune E. Johnsen for assisting with X-Ray Diffraction measurements.

Supplementary materials

Experimental methods

Evaluation of 3D-OMiTEM

Beam damage assessment

Missing wedge effects

EFTEM analysis

Determination of Percolation Path with Least Resistivity

Figs. S1 to S4

References

1. N. Q. Minh, "Solid oxide fuel cell technology - features and applications," *Solid State Ionics*, vol. 174, no. 1-4, pp. 271–277, 2004.

2. S. H. Jo, P. Muralidharan, and D. K. Kim, "Electrical characterization of dense and porous nanocrystalline Gd-doped ceria electrolytes," *Solid State Ionics*, vol. 178, no. 39-40, pp. 1990–1997, 2008.
3. W. J. Bowman, A. Darbal, and P. A. Crozier, "Linking macroscopic and nanoscopic ionic conductivity: A semiempirical framework for characterizing grain boundary conductivity in polycrystalline ceramics," *Acs Applied Materials and Interfaces*, vol. 12, no. 1, pp. 507–517, 2020.
4. W. J. Bowman, M. N. Kelly, G. S. Rohrer, C. A. Hernandez, and P. A. Crozier, "Enhanced ionic conductivity in electroceramics by nanoscale enrichment of grain boundaries with high solute concentration," *Nanoscale*, vol. 9, no. 44, pp. 17293–17302, 2017.
5. R. A. De Souza, J. Fleig, J. Maier, Z. Zhang, W. Sigle, and M. Rühle, "Electrical resistance of low-angle tilt grain boundaries in acceptor-doped SrTiO₃ as a function of misorientation angle," *Journal of Applied Physics*, vol. 97, no. 5, 2005.
6. R. Waser, "Electronic properties of grain boundaries in SrTiO₃ and BaTiO₃ ceramics," *Solid State Ionics*, vol. 75, no. C, pp. 89–99, 1995.
7. D. Y. Wang and A. S. Nowick, "The "grain-boundary effect" in doped ceria solid electrolytes," *Journal of Solid State Chemistry*, vol. 35, no. 3, pp. 325–333, 1980.
8. J. Tanaka, J. Baumard, and P. Abelard, "Nonlinear electrical-properties of grain-boundaries in an oxygen-ion conductor(CeO₂.Y₂O₃)," *Journal of the American Ceramic Society*, vol. 70, no. 9, pp. 637–643, 1987.
9. F. Ye, C. Y. Yin, D. R. Ou, and T. Mori, "Relationship between lattice mismatch and ionic conduction of grain boundary in ysz," *Progress in Natural Science: Materials International*, vol. 24, no. 1, pp. 83–86, 2014.

10. T. Zhang, Z. Zeng, H. Huang, P. Hing, and J. Kilner, "Effect of alumina addition on the electrical and mechanical properties of Ce_{0.8}Gd_{0.2}O_{2-δ} ceramics," *Materials Letters*, vol. 57, no. 1, pp. 124–129, 2002.
11. W. J. Bowman, J. Zhu, R. Sharma, and P. A. Crozier, "Electrical conductivity and grain boundary composition of Gd-doped and Gd/Pr co-doped ceria," *Solid State Ionics*, vol. 272, pp. 9–17, 2015.
12. H. J. Avila-Paredes, K. Choi, C. T. Chen, and S. Kim, "Dopant-concentration dependence of grain-boundary conductivity in ceria: A space-charge analysis," *Journal of Materials Chemistry*, vol. 19, no. 27, pp. 4837–4842, 2009.
13. R. Gerhardt and A. S. Nowick, "GrainBoundary Effect in Ceria Doped with Trivalent Cations: I, Electrical Measurements," *Journal of the American Ceramic Society*, vol. 69, no. 9, pp. 641–646, 1986.
14. A. Jasper, J. A. Kilner, and D. W. McComb, "TEM and impedance spectroscopy of doped ceria electrolytes," *Solid State Ionics*, vol. 179, no. 21-26, pp. 904–908, 2008.
15. T. S. Zhang, J. Ma, H. Cheng, and S. H. Chan, "Ionic conductivity of high-purity Gd-doped ceria solid solutions," *Materials Research Bulletin*, vol. 41, no. 3, pp. 563–568, 2006.
16. H. J. Avila-Paredes and S. Kim, "The effect of segregated transition metal ions on the grain boundary resistivity of gadolinium doped ceria: Alteration of the space charge potential," *Solid State Ionics*, vol. 177, no. 35-36, pp. 3075–3080, 2006.
17. G. M. Christie and F. P. Van Berkel, "Microstructure - Ionic conductivity relationships in ceria-gadolinia electrolytes," *Solid State Ionics*, vol. 83, no. 1-2, pp. 17–27, 1996.

18. S. De Angelis, P. S. Jørgensen, V. Esposito, E. Hsiao Rho Tsai, M. Holler, K. Kreka, E. Abdellahi, and J. R. Bowen, "Ex-situ tracking solid oxide cell electrode microstructural evolution in a redox cycle by high resolution ptychographic nanotomography," *Journal of Power Sources*, vol. 360, pp. 520–527, 2017.
19. H. H. Liu, S. Schmidt, H. F. Poulsen, A. Godfrey, Z. Q. Liu, J. A. Sharon, and X. Huang, "Three-dimensional orientation mapping in the transmission electron microscope," *Science*, vol. 332, no. 6031, pp. 833–834, 2011.
20. G. Wu, W. Zhu, Q. He, Z. Feng, T. Huang, L. Zhang, S. Schmidt, A. Godfrey, and X. Huang, "2d and 3d orientation mapping in nanostructured metals: A review," *Nano Materials Science*, vol. 2, no. 1, pp. 50–57, 2020.
21. M. Zhi, S. Lee, N. Miller, N. H. Menzler, and N. Wu, "An intermediate-temperature solid oxide fuel cell with electrospun nanofiber cathode," *Energy and Environmental Science*, vol. 5, no. 5, pp. 7066–7071, 2012.
22. E. Zhao, Z. Jia, L. Zhao, Y. Xiong, C. Sun, and M. E. Brito, "One dimensional $\text{La}_{0.8}\text{Sr}_{0.2}\text{Co}_{0.2}\text{Fe}_{0.8}\text{O}_{3-\delta}$ nanocomposite cathodes for intermediate temperature solid oxide fuel cells," *Journal of Power Sources*, vol. 219, pp. 133–139, 2012.
23. C. C. Chou, C. F. Huang, and T. H. Yeh, "Characterization and catalytic activity of $\text{La}_{0.6}\text{Sr}_{0.4}\text{Co}_{0.2}\text{Fe}_{0.8}\text{O}_{3-\delta}$ -yttria stabilized zirconia electrospun nano-fiber as a cathode catalyst," *Ceramics International*, vol. 39, no. 1, pp. S549–S553, S549–S553, 2013.
24. L. Li, P. Zhang, R. Liu, and S. M. Guo, "Preparation of fibrous ni-coated-ysz anodes for solid oxide fuel cells," *Journal of Power Sources*, vol. 196, no. 3, pp. 1242–1247, 2011.

25. L. Fan, Y. Xiong, L. Liu, Y. Wang, H. Kishimoto, K. Yamaji, and T. Horita, "Performance of $\text{gd}_{0.2}\text{ce}_{0.8}\text{o}_{1.9}$ infiltrated $\text{la}_{0.2}\text{sr}_{0.8}\text{tio}_3$ nanofiber scaffolds as anodes for solid oxide fuel cells," *Journal of Power Sources*, vol. 265, pp. 125–131, 2014.
26. W. Zhang, "Electrospinning for solid oxide fuel cells," *Electrospinning for Advanced Energy and Environmental Applications*, pp. 61–76, 2015.
27. Thermo Fisher Scientific, Inspect3D, <https://www.thermofisher.com/dk/en/home/electron-microscopy/products/software-em-3d-vis/inspect-3d-software.html>
28. K. Glowinski and A. Morawiec, "A toolbox for geometric grain boundary characterization," *Proceedings of the 1st International Conference on 3d Materials Science*, pp. 119–124, 2016.
29. K. Glowinski and A. Morawiec, "Analysis of experimental grain boundary distributions based on boundary-space metrics," *Metallurgical and Materials Transactions A: Physical Metallurgy and Materials Science*, vol. 45, no. 8, pp. 3189–3194, 2014.
30. DREAM3D, <http://dream3d.bluequartz.net/>.
31. F. Hofer, W. Grogger, G. Kothleitner, and P. Warbichler, "Quantitative analysis of EFTEM elemental distribution images," *Ultramicroscopy*, vol. 67, no. 1-4, pp. 83–103, 1997.
32. P. Thomas and P. Midgley, "Eftem," *Transmission Electron Microscopy*, pp. 377–404, 2016.
33. TVIPS, "Em-dfom, <https://www.tvips.com/imaging-software/em-tools/em-dfom/>."
34. J. A. Sethian and A. M. Popovici, "3-d travelttime computation using the fast marching method," *Geophysics*, vol. 64, no. 2, pp. 516–523, 1999.

Technical
University of
Denmark

Fysikvej, Building 310
2800 Kgs. Lyngby
Tlf. 4525 1700

www.energy.dtu.dk